THE UNIVERSITY OF CHICAGO

ANALYZING EXTRATERRESTRIAL MATERIALS AT THE NANOSCALE: RESOLVING THE ANCESTRY OF PRIMITIVE AMORPHOUS SILICATES

A DISSERTATION SUBMITTED TO

THE FACULTY OF THE DIVISION OF THE PHYSICAL SCIENCES

IN CANDIDACY FOR THE DEGREE OF

DOCTOR OF PHILOSOPHY

DEPARTMENT OF THE GEOPHYSICAL SCIENCES

BY

KRYSTEN LAUREN VILLALON

CHICAGO, ILLINOIS

JUNE 2021

This dissertation is dedicated to my parents, for providing “their little space cadette” with unconditional love and support so that she could live a happy and fulfilled life.

Fry: "Wait, I'm having one of those things...a headache, with pictures!"

Leela: "An idea?"

—Futurama

TABLE OF CONTENTS

LIST OF FIGURES

LIST OF TABLES

LIST OF COMMON ABBREVIATIONS

AGB	Asymptotic Giant Branch
AMM	Antarctic Micrometeorite
BF	Bright Field
CP-IDP	Chondritic Porous Interplanetary Dust Particle
DF	Dark Field
EDS	Energy-dispersive X-ray spectroscopy
FIB	Focused Ion Beam
GIS	Gas Injection System
GEMS	Glass with Embedded Metals and Sulfides
HAADF	High-Angle Angular Dark Field
IDP	Interplanetary Dust Particle
ISM	Interstellar Medium
LIC	Local Interstellar Cloud
LISM	Local Interstellar Medium
LIME	Low-Iron, Manganese-Enriched
RIMS	Resonance Ionization Mass Spectrometry
SAED	Selected Area Electron Diffraction
SEM	Scanning Electron Microscopy
SIMS	Secondary Ion Mass Spectrometry
STEM	Scanning Transmission Electron Microscopy
SLR	Short-Lived Radionuclide
TEM	Transmission Electron Microscopy
UCAMM	Ultracarbonaceous Antarctic Micrometeorite

ACKNOWLEDGEMENTS

This dissertation could not have been possible without the support of many advisors, colleagues, friends, and family, without whom I would have likely instead become a dog walker who likes to talk about space. First and foremost, I would like to thank my thesis advisor, Andrew Davis, for taking a chance on an Art History major. I also thank Andy for allowing me to develop my own research plans and pursue my own goals, supporting my research needs in order to gain expertise and to produce the highest quality data, and for always being available for help and advice. I would also like to thank the rest of my committee members, Thomas Stephan, Philipp Heck, Fred Ciesla, and Andrew Campbell, for providing their time, expertise, and kindness so that I could become the best scientist I can be and for believing that I could be successful in this field.

I would like to thank John Bradley, Hope Ishii, and Kenta Ohtaki for collaborating with me on the TEM work and for sharing their wealth of knowledge with me. I would also like to thank Nicole Nie and Nigel Brauser for their collaboration on some of the FIB related work, and Reto Trappitsch and Patrick Boehnke for their help with CHILI.

I would like to thank my current and former graduate and post graduate DOGS buddies Levke Kööp, Jennika Greer, Nicole Nie, Manavi Jadhav, and Nan Liu. Thank you for your friendship throughout the years, and for the much-needed coffee breaks, walks to the pond, turtle counting, duck watching, minecrafting, or wine/whine nights. I'd also like to thank Gerry Olack for his friendship, for maintaining the SEM lab, and for being a delightful and silly goose.

I would like to thank my parents, George and Vivian Villalon, my brother Steven Villalon, and my Aunt Beatriz Perez for their unconditional love throughout my entire life. I love you all so much.

I would like to thank Ryan Cross, my most special and sneaky kiwi, my favorite person in the whole world. You are the best thing that has ever happened to me and I'm so thankful to have had you by my side during grad school.

I would like to thank NASA Headquarters for supporting this work under the NASA Earth and Space Science Fellowship Program–Grant 80NSSC17K0494. I also thank Matthieu Gounelle and the Muséum National d'Histoire Naturelle for providing the Paris meteorite sample. I thank Terry Boudreaux for donating Aguas Zarcas to the Field Museum, and Jennika Greer and Drew Carhart for mounting and polishing the sample. This work made use of the instruments in the Electron Microscopy Core of UIC's Research Resources Center. I thank the TAWANI Foundation for funding the Robert A. Pritzker Center for Meteoritics and Polar Studies. I also thank Karen Bustillo at the Molecular Foundry at Lawrence Berkeley National Laboratory where portions of this work were performed. I would also like to thank Surya Rout and Sheryl Singerling for their helpful discussions related to TEM and diffraction analyses.

ABSTRACT

Presolar, circumstellar silicates have been positively identified by their highly anomalous oxygen isotopic compositions using secondary ion mass spectrometry (SIMS), yet presolar, interstellar silicates have eluded unambiguous discovery. Glass with embedded metal and sulfides (GEMS)—amorphous silicates that are an abundant constituent of primitive interplanetary dust particles (IDPs)—have been proposed to be these interstellar grains. Circumstellar silicates and GEMS may therefore represent related and consecutive stages in the lifetime of cosmic silicates. A competing hypothesis is that GEMS are vapor-phase, nonequilibrium condensates from the early solar nebula. In either case, GEMS may also be precursors to the amorphous silicates in primitive meteorites prior to parent body processing. The various silicate components of different primitive samples may represent various related stages in silicate dust evolution—from condensation around stars, interstellar medium processing, incorporation into growing planetesimals in protoplanetary disks, to subsequent parent body processing.

Analytical challenges have impeded the nanometer-scale components of fine-grained, extraterrestrial materials from being fully characterized. This dissertation explores techniques in sample preparation and quantitative microanalysis to allow for detailed characterizations of these components at an unprecedented level of accuracy and precision. Applying new methods of sample preparation using focused ion beam (FIB) milling in combination with scanning transmission electron microscopy (STEM) nanodiffraction and resonance ionization mass spectrometry (RIMS), we demonstrate how seemingly morphologically and chemically similar materials at the micrometer scale can show significant differences at the nanometer scale and sheds light on the ancestral connections, or lack thereof, between these enigmatic types of grains.

Chapter 1

Introduction

The word "dust" brings to mind that of the boring and mundane—the stuff that covers a neglected mantle above a fireplace or permeates the air in an old attic. But dust can also refer to quite extraordinary materials, such as the ashes of dying stars or the pulverized remains of planetary impacts. Dust pervades the universe as the byproduct of a myriad of astronomical phenomena; and dust plays a highly influential role in the evolution of galaxies and planetary systems. Extraterrestrial dust[1] (also referred to as cosmic dust or space dust) can therefore help us understand the processes that contribute to dust formation as well as the processes affected by the presence of dust. This dissertation explores the nanometer-scale chemistry and mineralogy of cosmic dust, specifically silicate dust trapped inside primitive meteorites that have experienced minimal secondary alteration, in order to better understand our early Solar System's history and the galactic lifecycle of matter. In this introductory chapter, I begin with an overview of cosmic dust in order to provide context as to the motivation behind this work.

A common misconception is that the space between planets, stars, and galaxies is a perfect vacuum. While certainly a far better vacuum than anything created on Earth, outer space is nonetheless lightly littered by gas and dust.[2] The presence of even small quantities of dust can have a number of significant consequences: 1) dust transforms the thermal structure of its galactic

[1] Dust is an imprecise term that loosely refers to any solid particulate matter roughly <1 mm. For the purpose of this dissertation, no distinction is made between small dust grains and large molecules.

[2] The lowest pressure regime currently achievable in a lab, called Extreme High Vacuum, is $<1\times10^{-12}$ Torr, corresponds to a density of $\sim1\times10^{6}$ particles/cm^3. The lowest pressure reportedly attained in a lab was $<5\times10^{-17}$ Torr (Gabrielse et al., 1990) and corresponds to a density of ~100 particles/cm^3. Compare these to densities found in the interstellar medium (ISM), which can range from as high as $\sim10^{6}$ particles/cm^3 in molecular clouds to as low as ~0.0065 particles/cm^3 in coronal gas (Ferrière, 2001).

environment by efficiently absorbing, scattering, and emitting radiation; 2) grain surfaces act as catalysts for chemical reactions, such as the formation of molecular hydrogen, water, and organic molecules essential for the creation of life; 3) dust grains sequester metals and act as condensation nuclei to seed nebulae, star, and planet formation; and 4) dust obscures or eclipses background objects, impeding the study of these objects. Cosmic dust is therefore a highly influential constituent of any astrophysical environment and determining the chemical and physical properties of this dust is the crux of many cosmological inquiries.

Silicate dust in particular is observed to be pervasive in most astrophysical environments, such as the winds of asymptotic giant branch (AGB) stars and Type II supernovae, the diffuse interstellar medium (ISM), molecular clouds, protoplanetary disks, as well as our own Solar System. Cosmic silicates are therefore extremely important for understanding the life cycle of matter, from nucleosynthesis in stars, interstellar processing, and Solar System formation to parent body alteration. Silicates are also among the most abundant component of meteorites, micrometeorites (MMs), and interplanetary dust particles (IDPs), yet many questions regarding the origins of and relationships between these different objects and their components remain.

Observational astronomers use telescopes to study cosmic dust by its interaction with electromagnetic radiation, through the interpretation of spectral features arising from optical phenomena such as extinction (absorption and scattering), polarization, and emission. Unfortunately, the amount of information that can be gathered from telescopic observations is limited as they are conducted at, quite literally, astronomical distances. Astronomical observations provide important constraints on the average properties of cosmic dust populations in different environments, but only *in situ* studies can provide highly detailed characterizations of individual grains, potentially down to the atomic scale, and are therefore necessary for understanding the chemical complexity and diversity of grains within cosmic dust populations. While the fine-grained

nature of cosmic dust, particularly cosmic silicates, makes laboratory studies analytically challenging, advances in sample-preparation and instrumentation now allow for detailed characterizations of cosmic dust at an unprecedented level of accuracy and precision.

This first chapter introduces the different types of cosmic dust, their importance in the context of understanding galactic chemical evolution and the open questions that still remain regarding their histories and interrelationships. The second chapter gives an overview of the samples studied, as well as sample preparation methods and analytical techniques for submicron analysis.

1.1 The Lifecycle of Matter: A Primer on Cosmic Dust Nomenclature

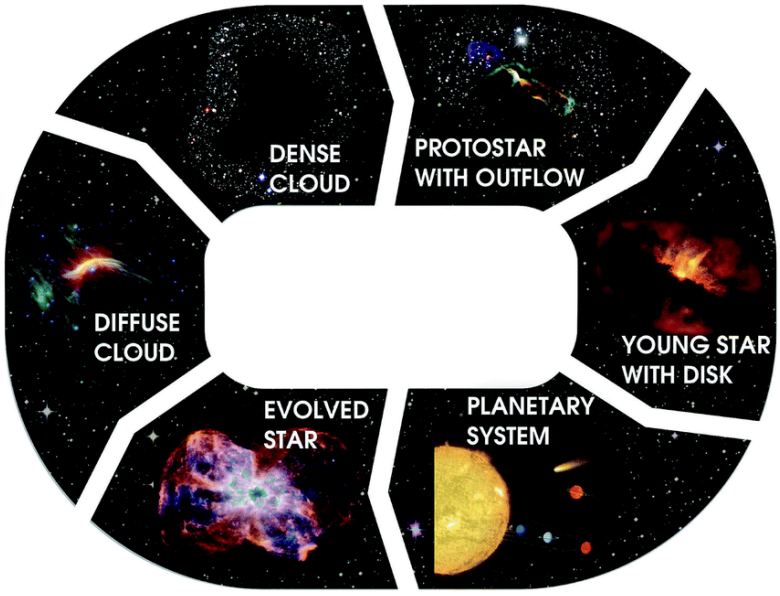

Figure 1.1: The lifecycle of gas, dust and ice in interstellar and circumstellar clouds. Credit: M. Persson, NASA/ESA/ESO/ALMA

The galaxy is not static—material is continually modified, cycled, and recycled through different environments (Figure 1.1). After the Big Bang, the hot early universe contained only the light nuclides ^{1}H, ^{2}D, ^{3}He, ^{4}He, and ^{7}Li. Most of the heavier elements were synthesized in stars via nucleosynthesis and released back into their surroundings in stellar winds or explosions, where these heavy elements could then condense into dust grains to be later incorporated into future

generations of stars or planetary systems. These grains that condense around evolving or dying stars are called *circumstellar* grains (and are also referred to as stardust). Circumstellar grains are released into the surrounding ISM where they are "subject to a variety of indignities, lumped under the general term of grain processing."[3] The ISM is a destructive environment, where grains are continually modified and isotopically homogenized by irradiation, supernova shocks, and grain-grain collisions. There is no clear point at which a circumstellar grain becomes interstellar, but, for the purposes of this review, circumstellar grains are those that retain their exotic isotopic signatures inherited by their parent stars, while interstellar grains are those that have lost such isotopic signatures due to extensive processing in the ISM. Solid dust particles account for only ~1% of the mass in the ISM (Draine et al., 2007), and models estimate that only a few percent of these solid grains can be circumstellar in origin (Zhukovska et al., 2008; Draine, 2009; Hoppe et al., 2017). Circumstellar grains are therefore not representative of *interstellar* grains, or the grains that compose the ISM. *In situ* dust formation is required to account for the currently observed mass of ISM dust and gas-phase elemental depletions, but it is still unconstrained whether sufficient quantities of silicate and carbonaceous grains can form under the temperature and density regimes typical of the diffuse ISM, although recent experimental studies have demonstrated that silicates may be able to condense in cold (<20 K) and dense regions of the ISM called molecular clouds (Krasnokutski et al., 2014; Rouillé et al., 2014).

Planetary systems themselves also form in molecular clouds. While much of the interstellar/molecular cloud material is ultimately destroyed during and after star formation, the discovery of *presolar grains* in meteorites and IDPs confirmed that some of this material that was available prior to Solar System formation indeed survived. Presolar grains are grains that formed

[3] Seab, C. G. (1998) Grain Destruction and Growth in *Dust in the Universe* (M. E. Bailey, D. A. Williams, Eds.) p. 304.

prior to the formation of the Solar System. They have been positively identified in meteorites, MMs, IDPs, and samples from comet Wild 2 returned by the Stardust mission (Zinner, 2014). Unless otherwise specified, presolar grains usually refer specifically to circumstellar grains as they are identified by their anomalous isotopic signatures inherited from their parent star. Presolar interstellar grains have yet to be conclusively identified in extraterrestrial samples, but the elemental compositions of contemporary interstellar grains have been studied *in situ* aboard the Cassini spacecraft (Altobelli et al., 2016) and from samples returned from the Stardust mission (Westphal et al., 2014), as well as observationally using spectroscopy.

Meteorites are rock fragments originating from collisions in the asteroid belt. MMs and IDPs emanate from either asteroid collisions or the disintegration of comets as they approach the Sun. IDPs and MMs differ by their collection method—IDPs are dust samples collected in the stratosphere by high altitude aircraft, while MMs are generally larger dust samples recovered on Earth's surface.

Silicates are pervasive in most astrophysical environments, such as the winds of asymptotic giant branch stars and Type II supernovae, the diffuse ISM, molecular clouds, protoplanetary disks, as well as our own Solar System. Cosmic silicates are therefore extremely important for understanding the life cycle of matter, from nucleosynthesis in stars, interstellar processing, and Solar System formation to parent body alteration. The fundamental questions of this thesis are as follows: 1) How do the properties of silicate grains vary depending on their formation environment? 2) How do silicate grains change throughout their lifetimes after they have travelled through one or many different environments? 3) What is already known about the different environments that form or host silicate grains or the silicate components in various cosmic samples?

A major component of primitive carbonaceous chondrite (CC) matrices is amorphous silicate. Amorphous silicate is highly susceptible to alteration, and its presence is therefore assumed

to be indicative of minimal secondary processing. Amorphous silicate is also a dominant component of the ISM (Kemper et al., 2004) as well as chondritic porous interplanetary dust particles (CP-IDPs), a subset of highly porous IDPs that are believed to originate in comets and are considered to be the most pristine extraterrestrial samples to date (Bradley, 2014). The amorphous silicate in CP-IDPs is referred to as GEMS (glass with embedded metal and sulfides) as the amorphous silicate contains inclusions of kamacite (α-Fe,Ni) and pyrrhotite ($Fe_{(1-x)}S$). The origins of GEMS remain contentiously debated: they have been argued to be surviving presolar, interstellar silicates (Bradley, 1994); condensates from the early solar nebula (Keller and Messenger, 2011); or a combination, whereby cyclical processing in the ISM culminates with processing in our own presolar nebula and protoplanetary disk (Ishii et al., 2018).

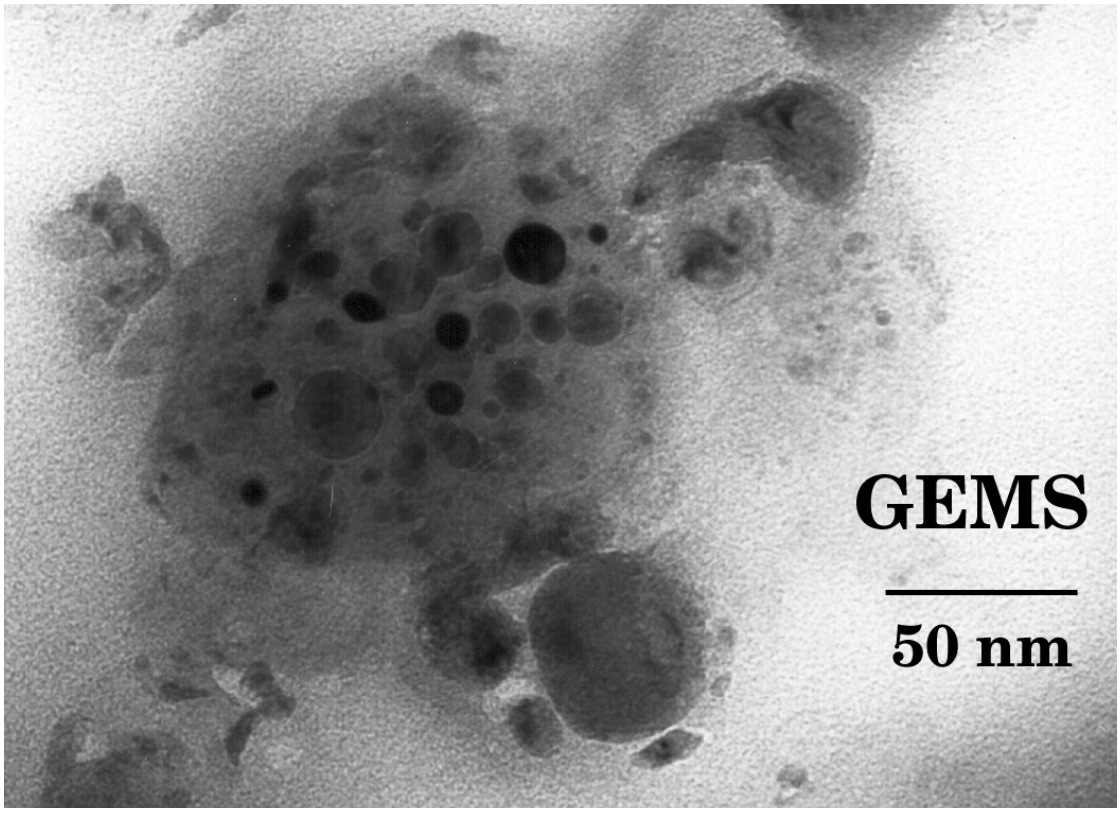

Figure 1.2: GEMS grain from an IDP. Image courtesy of NASA JPL.

Presolar, *circumstellar* silicates are among the most abundant presolar phases found in extraterrestrial samples, second only to nanodiamonds, and are found at abundances as high as ~250 ppm in meteorites and >400 ppm in anhydrous IDPs (Floss and Haenecour, 2016; Nittler et al., 2018). In contrast, presolar, *interstellar* silicates have eluded unambiguous discovery in primitive materials despite interstellar silicates being the predominant solid component of the ISM. GEMS grains have been proposed to be these missing presolar, interstellar grains (Bradley, 1994). Presolar (circumstellar) silicates and GEMS may therefore represent related and consecutive stages in the lifetime of cosmic silicates. Keller and Messenger (2011) argue that the majority of GEMS grains are instead vapor-phase, nonequilibrium condensates that formed at temperatures >1000 K in the inner Solar System, while a small minority of isotopically anomalous GEMS are circumstellar silicates. In either case, GEMS may be a primary building block of the Solar System. Thus, the various silicate components of different primitive samples may represent related stages in silicate dust evolution—from condensation around stars, ISM processing, incorporation into growing planetesimals in protoplanetary disks, to subsequent parent body processing.

1.2 Overview and Motivation

Despite their abundance in anhydrous IDPs, GEMS has yet to be unambiguously identified in meteorites. A central question to this dissertation is: if GEMS is a primary component of primitive IDPs and was a primary building block of early SS materials, is it found in primitive carbonaceous chondrites? GEMS-like material with textural similarities to GEMS as well as comparable average chemical compositions as measured by energy-dispersive X-ray spectroscopy (EDS) have been reported in the CM2 chondrites Paris and Y-791198, Acfer 094 (C2-ungrouped), and a carbon-rich clast from the CR2 chondrite LaPaz Icefield 02342 (Chizmadia and Brearley, 2008; Leroux et al., 2015; Nittler et al., 2019; Matsumoto et al., 2019). Similar objects also appear

to be abundant in UCAMMs (Dobrică et al., 2012; Noguchi et al., 2015). Unfortunately, the ubiquity of nanophase components throughout GEMS and GEMS-like material makes comparisons between them analytically challenging and necessitates more detailed scrutiny before drawing conclusions. Nanoparticles embedded within or surrounding GEMS and GEMS-like objects are ~1–30 nm in size, smaller than the thinnest TEM sections. Therefore, even with sufficiently high spatial resolution, EDS of the embedded nanoparticles is limited by interactions of the electron beam with the surrounding material. Also, EDS does not provide any structural information, which is crucial for a proper identification of GEMS. Electron diffraction provides crystallographic information and is therefore a complementary technique that can provide robust sample characterization when used in combination with EDS. While the mineralogy of the nanoparticles in IDP GEMS has been previously explored (e.g., Dai and Bradley, 2001), the mineralogy of those in meteoritic GEMS-like objects has yet to be determined.

Using nanodiffraction in a scanning transmission electron microscope (STEM) in combination with TEM and STEM EDS, we have determined the mineralogy and elemental compositions of the nanoparticles in the GEMS-like objects of the Paris meteorite for comparison with those from *bona fide* GEMS. Paris is a breccia considered to be one of the least altered CM chondrites (Hewins et al., 2014) but has evidence of heterogeneous aqueous alteration, containing both metal-rich lithologies (CM2.9) with abundant amorphous silicates as well as metal-poor lithologies (CM2.7) with abundant phyllosilicates. GEMS-like material is abundant throughout Paris, particularly in the interchondrule matrix (ICM) of the least altered lithologies and fine-grained rims (FGRs) around chondrules (Leroux et al., 2015). If the GEMS-like material in primitive meteorites can be confirmed to be related to IDP GEMS, it may uniquely demonstrate the progression of silicates from the ISM and/or early solar nebula to incorporation into a growing

planetesimal and subsequent alteration. If the GEMS-like material in primitive meteorites is unrelated to IDP GEMS, it may represent a significant, yet largely unexplored, class of objects.

We have also explored the differences between the fine-grained material from different regions of Paris: we sampled ICM material from both the more altered (~CM2.7), metal-poor lithologies as well as the less altered (~CM2.9), metal-rich lithologies; and we also sampled the FGRs surrounding metal-rich chondrules. ICM refers to the fine-grained (≤1 μm) material that fills the space between coarse-grained objects. FGRs are a texturally distinct fine-grained component of similar materials that commonly encloses chondrules and other coarse-grained objects in carbonaceous chondrites, particularly in CMs such as Paris. FGR thickness roughly correlates to the size of the enclosed object (Zanetta et al., 2021). The proportions of their components, such as amorphous silicate, alteration phases, and presolar silicates, differ between FGRs and ICMs within the same meteorite and between different meteorites (Leitner et al., 2016; Haenecour et al., 2018; Vollmer et al., 2020; Zanetta et al., 2021). The origin of FGRs remains unclear. Both nebular (Metzler et al., 1992; Metzler, 2004; Zanetta et al., 2021) and parent-body (Sears et al., 1993; Tomeoka and Tanimura, 2000; Trigo-Rodriguez et al., 2006; Takayama and Tomeoka, 2012) origins have been proposed for FGRs. Some FGRs show distinct layers in backscattered electron (BSE) imaging, usually an outer layer of dark (lower mean atomic number), higher-porosity material and an inner layer of lighter (higher mean atomic number), seemingly more compacted material (Trigo-Rodriguez et al., 2006; Zanetta et al., 2021). Single-layered FGRs appear texturally and compositionally indistinguishable from the outer layer material of layered FGRs and are therefore not distinguished below. Both the inner and outer layers of FGRs were sampled in this study.

For this dissertation, I am studying fine-grained silicates with a focus on understanding the origin and relationship between presolar silicates, interstellar silicates, GEMS, and primitive matrix

silicates. Due to their small sizes, analytical challenges have impeded the nanoscale components of fine-grained, extraterrestrial materials from being fully characterized. This dissertation explores techniques in sample preparation and quantitative microanalysis to allow for detailed characterizations of these components at an unprecedented level of accuracy and precision. Applying new methods of sample preparation using focused ion beam (FIB) milling in combination with scanning transmission electron microscopy (STEM) nanodiffraction and resonant ionization mass spectrometry (RIMS), we demonstrate how seemingly morphologically and chemically similar materials at the microscale can show significant differences at the nanoscale and sheds light on the ancestral connections, or lack thereof, between these enigmatic types of grains.

Chapter 2

Techniques and Samples

2.1 Techniques

2.1.1 FIB preparation

2.1.1.1 Conventional FIB liftout for (S)TEM analysis

As the name suggests, a FIB instrument uses a focused beam of ions (usually Ga^+ ions) to image samples as well as remove material via sputtering. In combination with a gas injection system (GIS), a FIB can also be used to deposit material via ion-beam-induced deposition (similarly, the electron beam in a SEM can be used to deposit material via electron-beam-induced deposition). Electron-transparent lamellae for characterization of samples in a TEM or STEM instrument are conventionally prepared using a FIB. In this process, an ~0.5–2.0 µm thick C or Pt coating is first deposited using the electron beam over the area of interest to protect the sample from subsequent Ga ion-beam damage. A thick C or Pt coating is then ion-beam-deposited over the previous coating, resulting in an ~5 µm thick protective strap. Carbon deposition can minimize: (1) curtaining effects; (2) contrast issues during high-angle annular dark-field (HAADF) imaging; and (3) interference between S and Pt X-ray lines during EDS analysis, while Pt deposition is often used because of its faster deposition rate, allowing for a much thicker protective coating prior to final thinning. Trenches (~15 µm long × ~10 µm wide × > 5 µm deep) are milled on each side of the lamella until 1–1.5 µm thickness of the lamella is achieved. The lamellae can be further thinned at this step, although this may lead to significant redeposition of surrounding material. The lamella is lifted out *in situ* with a micromanipulator and attached to a Cu TEM half-grid using electron or ion-beam assisted deposition. To reduce FIB-induced damage, the ion-beam energy is reduced from 30 keV

to 5 keV to 2 keV during final thinning and polishing steps until electron transparency is achieved. For this study, all FIB liftouts were performed using the TESCAN LYRA3 FIB-SEM equipped with an Oxford Instruments OmniGIS II gas injector at the University of Chicago, while final thinning to electron transparency was carried out using the FEI Helios NanoLab 660 FIB instrument at the University of Hawai'i at Mānoa just before TEM analyses.

2.1.1.2 FIB grain isolation for mass spectrometry analysis

Mass spectrometry techniques can provide valuable information on the isotopic composition of samples, but unfortunately the spatial resolution is insufficient to resolve most of the dust components discussed in this dissertation. This means that the beam samples material not only from the grain of interest, but from surrounding material as well, leading to isotopic compositions that are more isotopically normal than those of the grain of interest (Figure 2.1). While advances in mass spectrometry are continually improving the spatial resolution available on many instruments, mitigation strategies are often still necessary to study cosmic dust.

One mitigation strategy is to use a FIB to mill an annulus around the grain of interest so that much of the surrounding material is ~~removed~~ and unable to significantly contribute to the signal. FIB milling has been used previously to isolate presolar silicates for NanoSIMS analysis

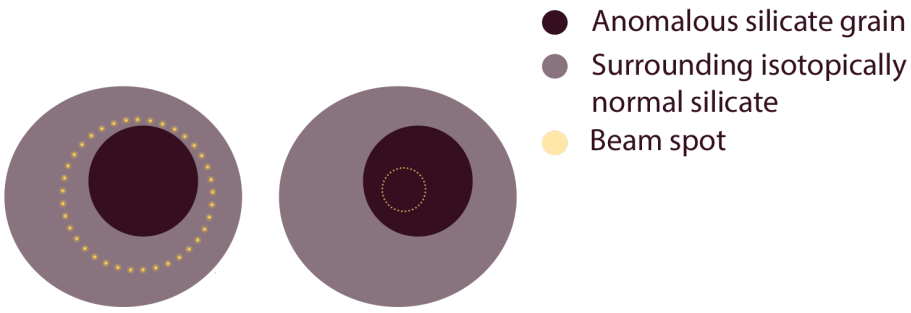

Figure 2.1: Cartoon depicting how insufficient spatial resolution leads isotopic compositions that are more isotopically normal due to overlap of surrounding material. Left: Configuration where the beam spot is larger than the grain of interest, leading to an isotopically dilute measurement as the surrounding isotopically normal material is also sampled. Right: Configuration where the spatial resolution is smaller than the grain of interest so that the isotopic composition only reflects that of the grain of interest.

(Nguyen and Messenger, 2014; Kodolányi et al., 2014). First, a cap of Pt is electron deposited over the grain to protect it from further milling and redeposition. Care must be taken to ensure the deposit is centered on the grain of interest. Second, an annulus with an outer diameter of >4 μm around the grain is milled away.

We further developed a method for fully lifting out and sequestering the grains from the surrounding material to prevent any contamination. After FIB milling around the grains, a W needle is attached to the Pt cap with another layer of Pt via ion deposition using an Oxford OmniProbe 400 micromanipulator. An area of the Au foil is "cleaned" by ion milling. The needle with exposed grain is then affixed to the surface with another Pt deposit to avoid loss of the sample. See Section 4.2 for reference images.

2.1.2 STEM nanodiffraction

In electron microscopy, a beam of electrons is directed toward a sample in order to provide images and characteristic information. The primary electron beam interacts with atoms within the sample to produce a variety of secondary signals, which are indicative of the sample's composition and mineralogy (Figure 2.2). In thick SEM specimens, many of these secondary signals often used for sample characterization, in particular backscattered electrons (BSE) or characteristic X-rays as used in EDS, originate from relatively large sample regions (on the order of a μm in diameter and depth dependent) and therefore limit the spatial resolution of the analyses. As shown in Figure 2.2, the spatial resolution is greatly improved when using electron-transparent samples for TEM analyses and can potentially provide information at the atomic level. The magnification of a TEM is 25–50× that of an SEM. As with SEM, characteristic X-rays used for EDS analyses can provide qualitative to quantitative elemental compositions of samples, although at a much improved spatial resolution in TEM compared to SEM. Elastically scattered electrons from TEM sections also

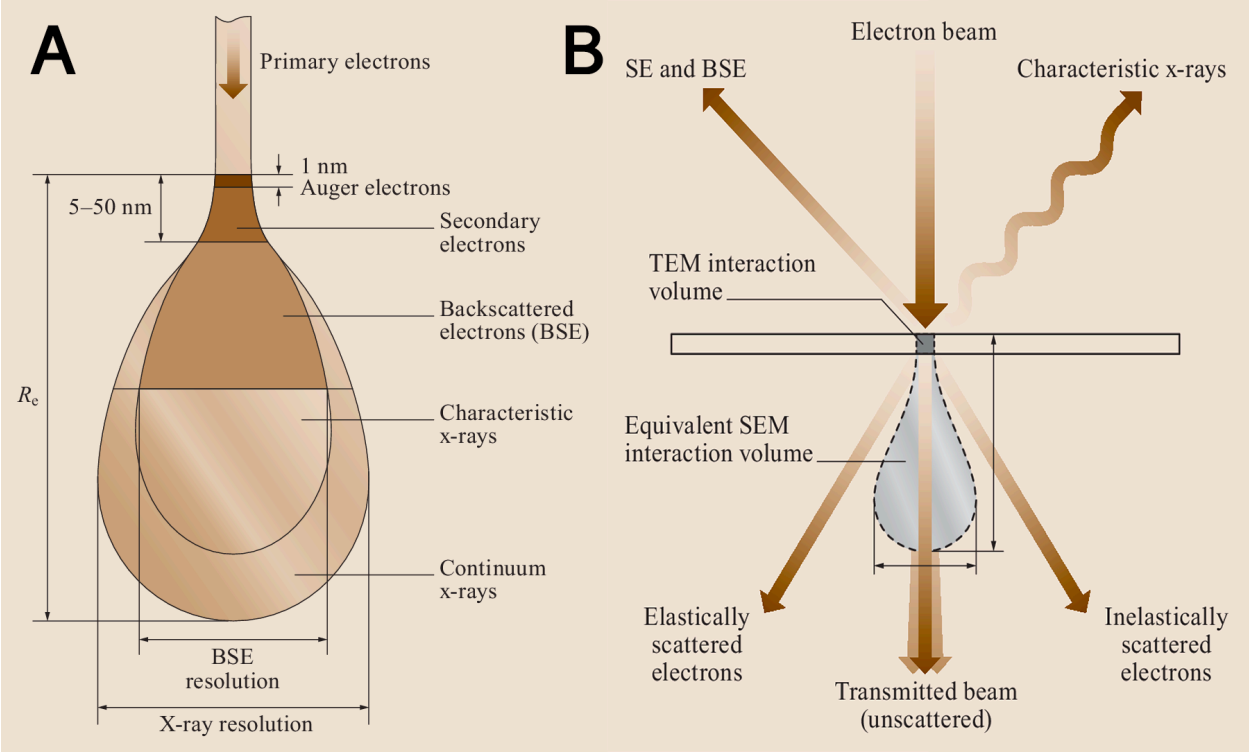

Figure 2.2: Electron beam sample interaction in an A) SEM with thick sample and a B) TEM with an electron-transparent sample. From McKinley (2019).

contribute to diffraction pattern formation and diffraction contrast images, while the energy lost by inelastically scattered electrons, used in techniques such as EELS, can provide further chemical and structural information, including oxidation states.

For all of these reasons, (S)TEM is a highly valuable technique for studying extraterrestrial samples such as presolar silicates, GEMS, and meteorite matrices with grains typically <1 μm in size; however, nanoparticles that are thinner than the TEM sections will still lead to beam overlap with surrounding material. Therefore, even with sufficiently high spatial resolution, EDS and conventional diffraction techniques of the embedded nanoparticles is limited by interactions of the electron beam with the surrounding material. Also, unlike with diffraction, EDS does not provide any structural information, which is crucial for a proper identification of GEMS.

Selected-area electron diffraction (SAED) is a widely utilized electron diffraction technique in geoscience but is unfortunately ill-suited to determining the crystal structures of components

<100 nm in size. Convergent-beam electron diffraction (CBED) is another conventional electron diffraction technique. CBED can sample regions a few nm in diameter and can be a powerful technique for determining crystallographic information; however, the convergent beam imparts high current densities, which can heat and damage the sample. A CBED pattern potentially provides a greater wealth of crystallographic information than an SAED pattern, but this also makes indexing of CBED patterns much more complicated. Nanodiffraction (Cowley, 1999) can be achieved using a small spot size, a small condenser aperture (<30 μm), and an extra condenser lens, available on modern TEMs. In STEM mode, images and diffraction patterns can be obtained simultaneously. Nanodiffraction has only seen limited use in meteoritics but is able to produce diffraction patterns from regions as small as ~1 nm without the sample damage imposed by CBED. Patterns are also easily indexable, as with SAED. Unlike with EDS, it is more easily discernible if multiple phases are contributing to an electron diffraction pattern, and it is possible to remove the contribution from unwanted phases. Nanodiffraction can therefore provide essential mineralogical information on the often-neglected smallest class of objects in meteorites.

2.1.3 CHILI

Mass spectrometry is an analytical technique that measures the mass-to-charge ratio (m/z) of atoms or molecules present in a sample, which can then be used to determine the isotopic compositions in a sample *in situ*. Secondary Ion Mass Spectrometry (SIMS) is a conventional technique used in cosmochemistry to study extraterrestrial samples. A SIMS instrument (also called an ion microprobe) uses positive (e.g., Cs^+) or negative (e.g., O^-) ions to remove sample material, which generates secondary ions that are sent through a mass spectrometer for analysis. The Cameca NanoSIMS is capable of acquiring SIMS data at especially high spatial resolutions down to 50 nm. Unfortunately, even with the resolution afforded by the NanoSIMS, presolar silicates,

and likewise similar materials in scale like IDPs and meteorite matrices, suffer from significant dilution effects due to their small sizes coupled with the high abundance of Solar System silicates (Figure 2.1). Another significant issue is that SIMS techniques are not able to resolve isobaric interferences, that is, they cannot differentiate isotopes of different elements at the same mass. Lastly, SIMS techniques have a quite low useful yield[4], which for small particles with fewer atoms than larger grains leads to large uncertainties from counting statistics.

The Chicago Instrument for Laser Ionization (CHILI, Figure 2.3) is a resonance ionization mass spectrometry (RIMS) instrument and is able to not only separate isobaric interferences but can also measure 2–3 elements simultaneously (potentially from the elements shown in Figure 2.4) for multi-element isotopic studies (Stephan et al., 2016). An illustration of the general operating principles for SIMS and RIMS instruments is shown in Figure 2.5 and a comparison showing the advantages of CHILI over SIMS is shown in Table 2.1. In SIMS, first a primary ion beam (usually Cs^+ or O^-) removes sample material, leading to a cloud of primarily neutral atoms and ~1% ionized atoms[5]. The ionized atoms are sent through a mass analyzer where they are separated by their mass-to-charge ratio. In RIMS, either a desorption laser or primary ion beam (Ga^+) removes sample material, but unlike in SIMS, the ~1% ionized atoms are first removed. Tunable lasers are then used to selectively ionize the remaining cloud of neutrals, ionizing a large fraction of the remaining atoms for the elements chosen, which are then sent through a time-of-flight mass analyzer.

CHILI is in the process of being optimized to one day reach an unprecedented lateral resolution of <50 nm and a useful yield of ~30–40%; While CHILI's current spatial resolution is

[4] The useful yield is the number of atoms detected divided by the number of atoms removed from the grain of interest.
[5] The ionization efficiency of SIMS is usually <1% for most elements, although higher efficiencies of <3% can be achieved under ideal conditions and up to 20% for alkalis (Stephan et al., 2016).

still in the range of a few hundred nm, it has a much higher sensitivity than NanoSIMS, which is particularly useful for measuring the isotopic compositions of the heavy trace elements such as strontium, molybdenum, barium, and zirconium.

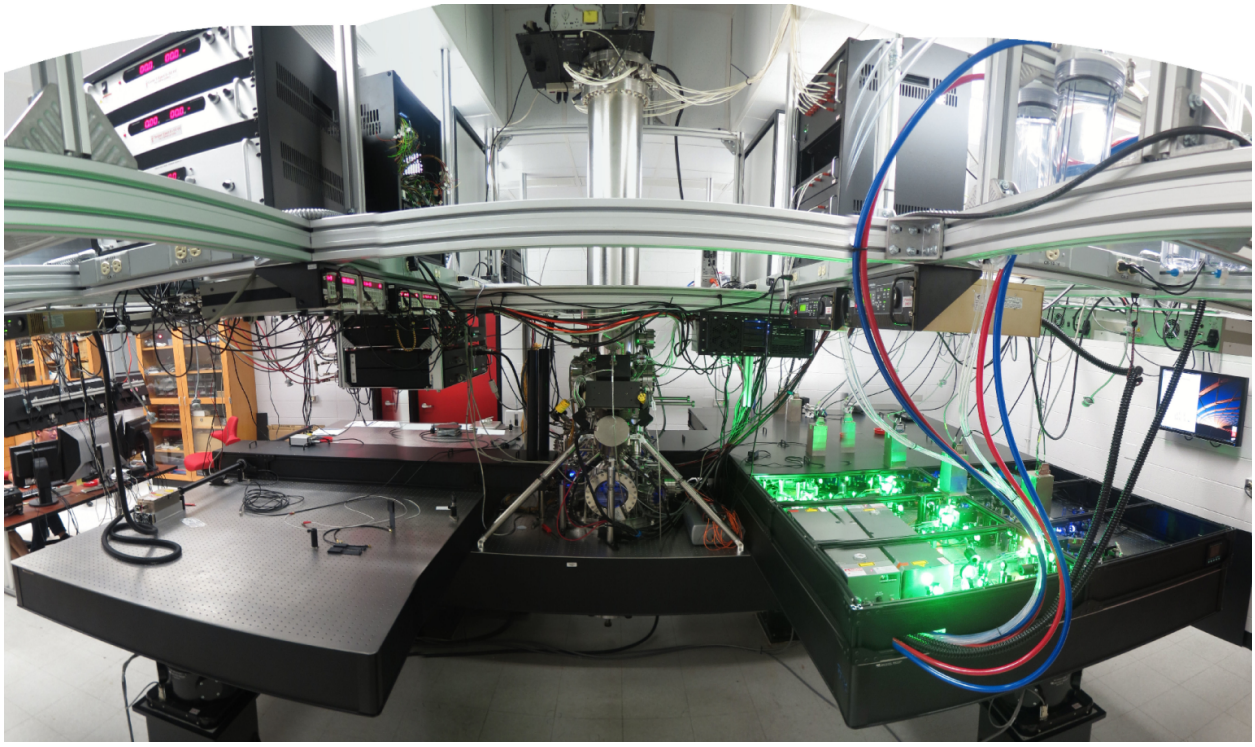

Figure 2.3: The Chicago Instrument for Laser Ionization. Image courtesy of Thomas Stephan.

H																	He
Li	Be											B	C	N	O	F	Ne
Na	Mg											Al	Si	P	S	Cl	Ar
K	Ca	Sc	Ti	V	Cr	Mn	Fe	Co	Ni	Cu	Zn	Ga	Ge	As	Se	Br	Kr
Rb	Sr	Y	Zr	Nb	Mo	Tc	Ru	Rh	Pd	Ag	Cd	In	Sn	Sb	Te	I	Xe
Cs	Ba	La	Hf	Ta	W	Re	Os	Ir	Pt	Au	Hg	Tl	Pb	Bi	Po	At	Rn
Fr	Ra	Ac															

Ce	Pr	Nd	Pm	Sm	Eu	Gd	Tb	Dy	Ho	Er	Tm	Yb	Lu
Th	Pa	U	Np	Pu	Am								

Figure 2.4: Periodic table of elements that can be analyzed by CHILI's current ionization lasers (unshaded). From Stephan et al. (2016)

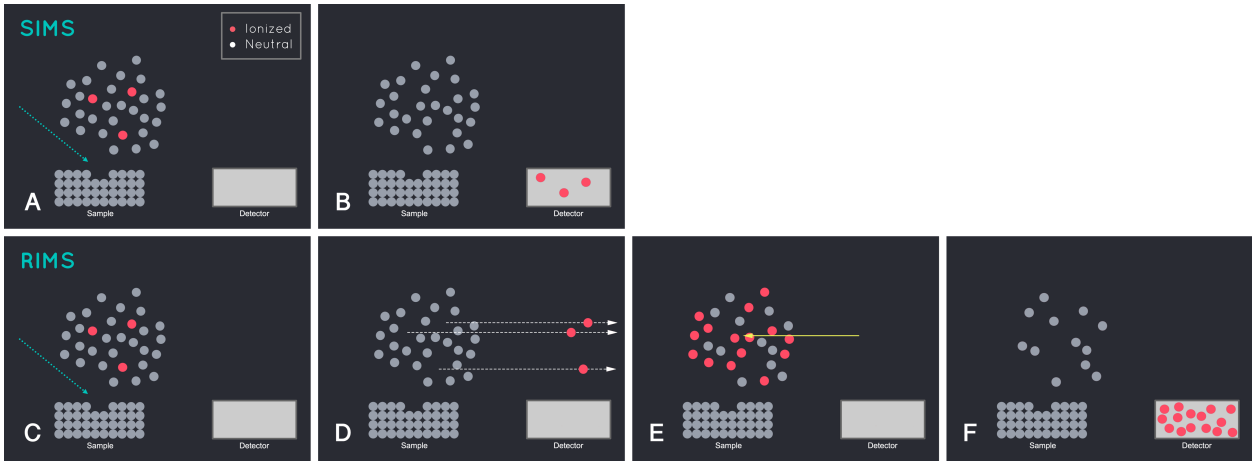

Figure 2.5: Illustration of the general principles behind SIMS and RIMS in a hypothetical single-element sample. SIMS: A) sample removal and subsequent ionization. B) Ionized atoms sent into a mass analyzer. RIMS: C) sample removal and subsequent ionization. D) removal of initial ionized atoms. E) selective ionization of remaining cloud of neutrals, F) ionized atoms sent through a time-of-flight mass analyzer and detected.

Table 2.1: Summary comparison between NanoSIMS and CHILI.

	NanoSIMS	**CHILI**
Lateral resolution	• Cs^+ primary beam (~50–100 nm) • O^- primary beam (~100–200 nm)	• Ga^+ primary beam (potentially: ~10–50 nm) • Desorption laser (~1 μm)
Isobaric interferences	Yes	Highly Suppressed
Useful yield	Typically <1%	Up to 30%–40%

2.2 Samples

2.2.1 The Paris meteorite

Purchased at an auction in the Hôtel Drouot in Paris and hidden amongst the personal effects of Jean Colonna-Cimera, a senior mining engineer in Africa and Southeast Asia and a collector of artifacts, the Paris meteorite is considered to be one of the least altered CM chondrites (Bourot-Denise et al., 2010; Hewins et al., 2014). It is a breccia with evidence of heterogeneous aqueous alteration, containing both metal-rich lithologies with abundant amorphous silicates as well as metal-poor lithologies with abundant phyllosilicates. Leroux et al. (2015) reported that

GEMS-like material is abundant throughout Paris, particularly in the interchondrule matrix (ICM) of the least altered lithologies and fine-grained rims (FGRs) around chondrules. If the GEMS-like material in primitive meteorites can be confirmed to be related to IDP GEMS, it may uniquely demonstrate the progression of silicates from the ISM and/or early solar nebula to incorporation into a growing planetesimal and subsequent alteration. If the GEMS-like material in primitive meteorites is unrelated to IDP GEMS, it may represent a significant, yet largely unexplored, class of objects.

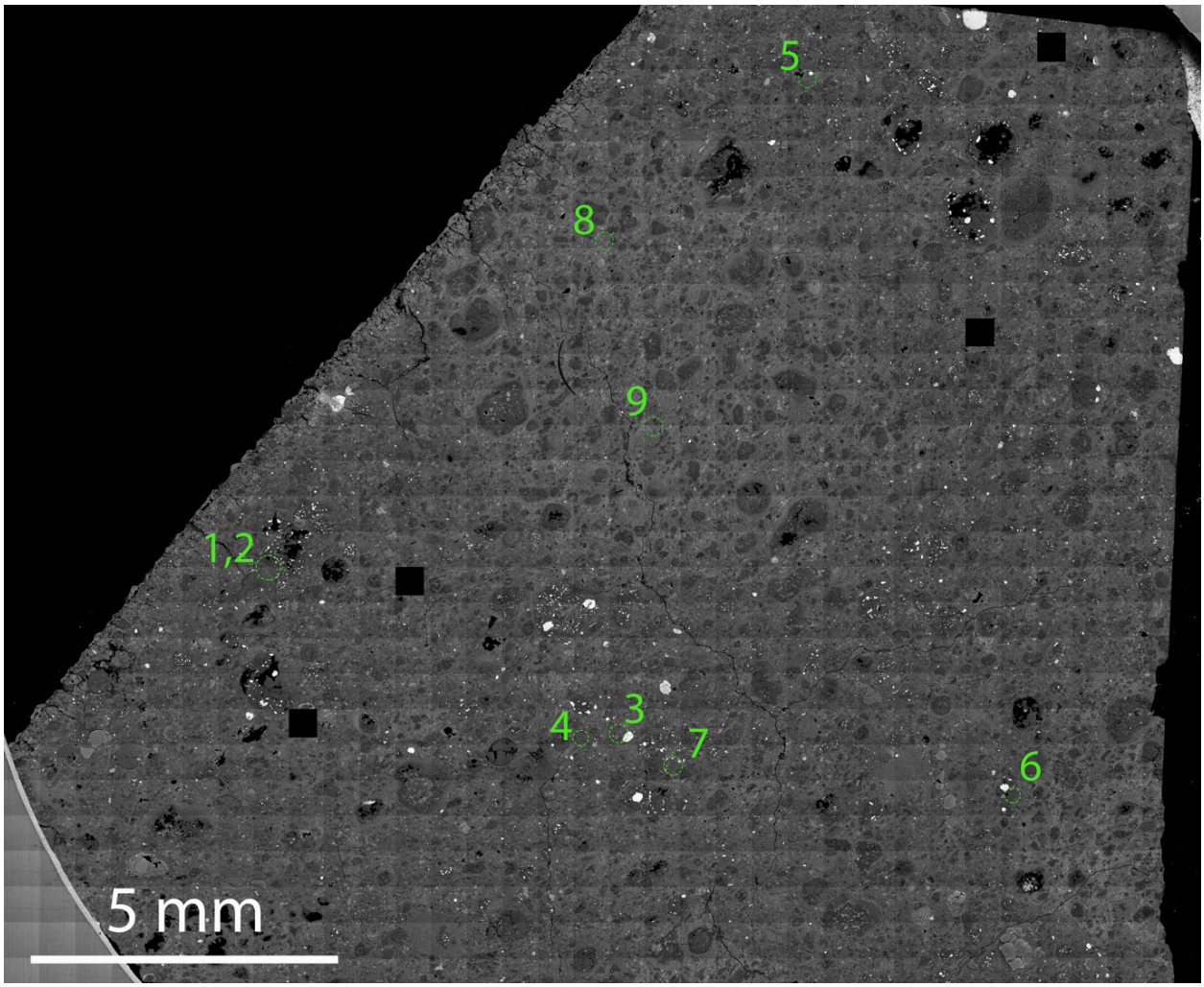

Figure 2.6: Backscattered electron (BSE) image of Paris section 2010-01. Regions sampled for TEM analysis are circled and numbered. Corresponding SE/BSE and STEM images from these regions are shown in Figs. 2.2–2.9.

Section 2010-1 of the Paris meteorite was provided by the Muséum National d'Histoire Naturelle in Paris. Nine lamellae (Figures 2.6–2.14) were lifted out and thinned using the TESCAN LYRA3 focused ion beam scanning electron microscope at the University of Chicago; final thinning to electron transparency was carried out using the FEI Helios NanoLab 660 FIB instrument at the University of Hawai'i at Mānoa just before TEM analyses.

2.2.2 Aguas Zarcas

Aguas Zarcas fell on April 23, 2019 in Costa Rica and is geochemically and isotopically consistent with a CM2 classification (Meteoritical Bulletin Database; Kerraouch et al., 2021). A large fraction of meteorite fragments from this fall was collected before rain and has not been exposed to liquid water on Earth. As such, Aguas Zarcas provides a unique opportunity to study components easily susceptible to contamination and terrestrial alteration, such as organic matter. Like many other CM meteorites, notably Paris, Aguas Zarcas is a breccia with different lithologies that have experienced widely varying levels of parent body aqueous alteration, with as many as five unique lithologies consistent with petrologic subtypes ranging from 2.2–2.8. A section of Aguas Zarcas, FMNH ME 6111.20, from a prerain specimen was provided for this study (Figure 2.15). This section was polished with water-free isopropanol and diamond lapping film at the Field Museum of Natural History (FMNH) and stored in dry conditions in low vacuum. Two lamellae from a metal-rich region of the section were lifted out and thinned using the TESCAN LYRA3 focused ion beam scanning electron microscope at the University of Chicago (Figures 2.16 and 2.17).

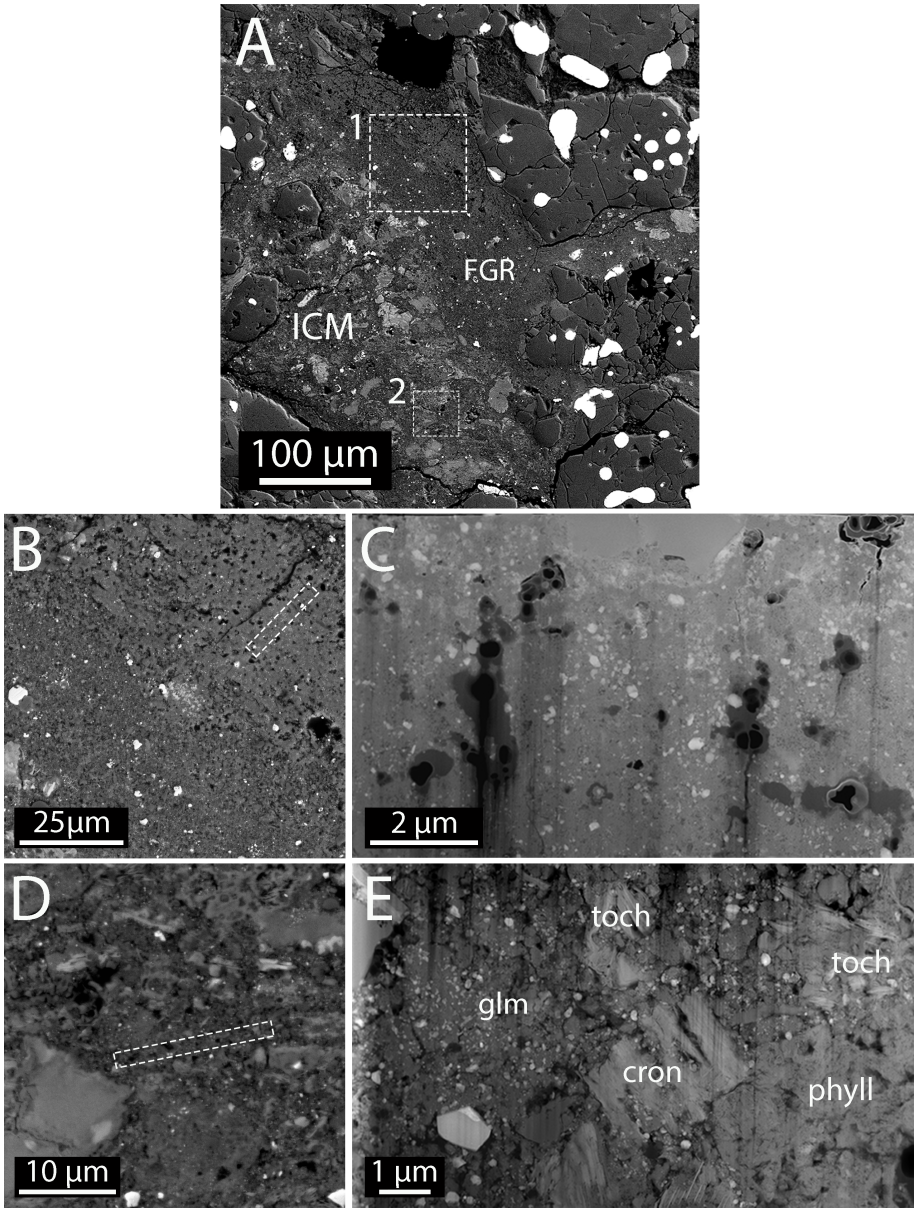

Figure 2.7: Corresponding BSE and dark-field (DF) scanning transmission electron microscopy (STEM) images showing the contextual overview of areas 1 and 2 as labelled in Figure 2.6. (A) BSE image of metal-rich chondrules with evident fine-grained rims (FGRs) adjacent to surrounding interchondrule matrix (ICM). (B) BSE image showing two distinct layers from an FGR and the lift-out location from area 1. (C) DF-STEM image of the lift-out from the interior layer of the FGR. Material is more compacted than material in other sections and has abundant organic nanoglobules. (D) BSE image of the lift-out location from area 2. (E) DF-STEM image of the lift-out from metal-rich ICM region. GEMS-like material (glm) is directly adjacent to hydrated phases, such as tochilinite (toch), cronstedite (cron), and phyllosilicates (phyll).

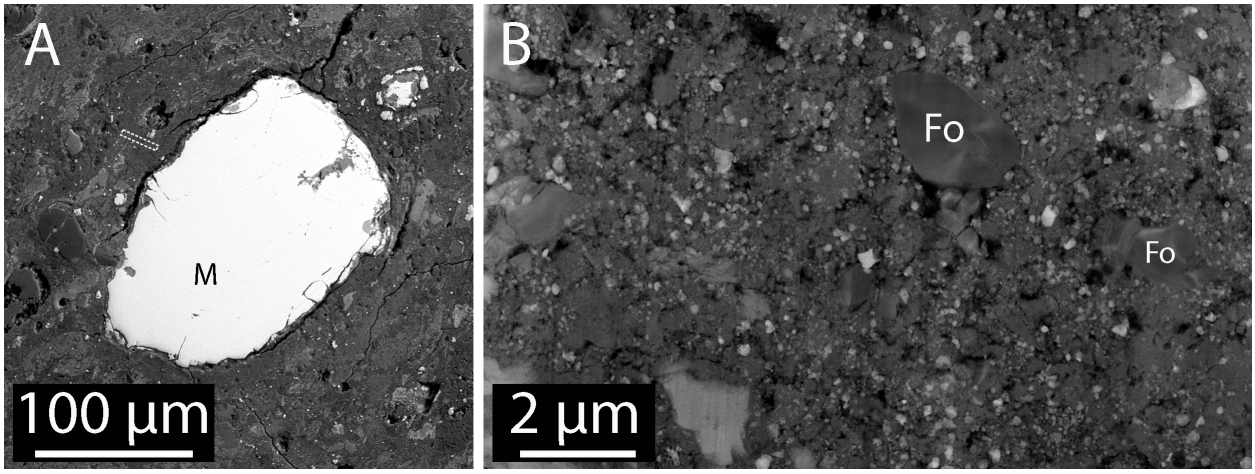

Figure 2.8: Corresponding BSE (A) and DF-STEM (B) images showing the contextual overview of area 3 as labelled in Figure 2.6. (A) BSE image of a large metal grain and surrounding ICM material. The lift-out location from area 3 is shown. Lighter gray ICM material corresponds to alteration phases (e.g., tochilinite). (B) DF-STEM image of the lift-out from ICM showing abundant GEMS-like material and few alteration phases. M = metal; Fo = forsterite.

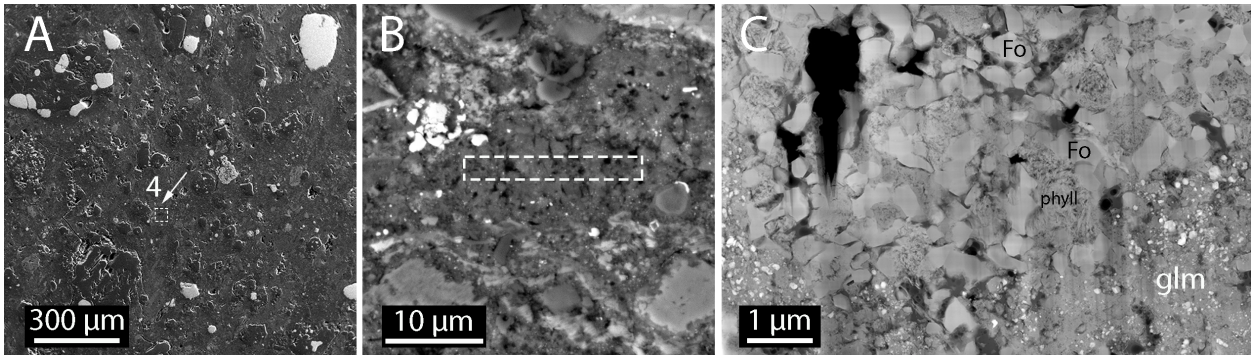

Figure 2.9: Corresponding SE (A), BSE (B), and DF-STEM (C) images showing the contextual overview of area 4 as labelled in Figure 2.6. (A) SE image of metal-rich zone of Paris. (B) BSE image of lift-out location from area 4. (C) DF-STEM image of the lift-out of ICM material. The top portion of the sample contains abundant crystalline olivine and pyroxene grains with interstitial course-grained, fibrous material. Some silicate grains have low-iron, manganese-enriched (LIME) compositions. GEMS-like material is found at the bottom corners of the sample. Fo= forsterite; phyll = phyllosilicate; glm = GEMS-like material.

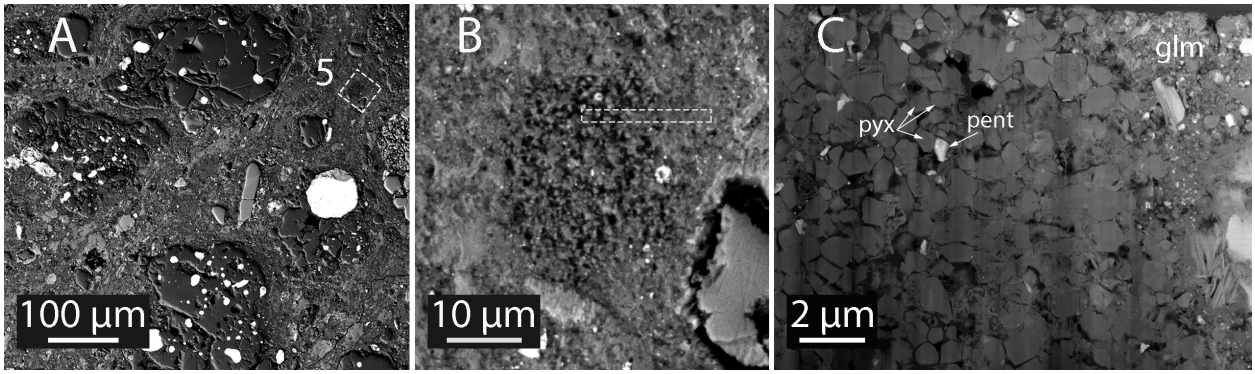

Figure 2.10: Corresponding BSE (A, B) and DF-STEM (C) images showing the contextual overview of area 5 as labelled in Figure 2.6. (A) BSE image of metal-rich region of Paris. (B) BSE image of the lift-out location from area 5. The lift-out spanned two regions of different composition and porosity. (C) DF-STEM of lift-out of ICM material. GEMS-like material only found at in top-right portion of the sample, directly adjacent to hydrated phases and crystalline silicates similar to those found in Figure 2.9. Some silicate grains have LIME compositions. Pyx = pyroxene; pent = pentlandite.

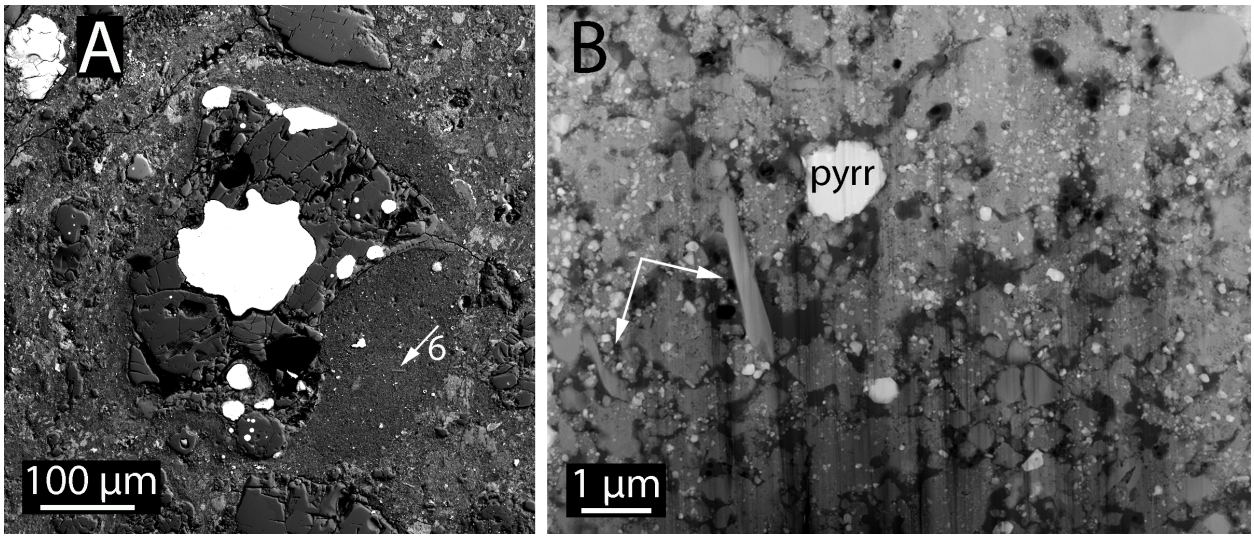

Figure 2.11: Corresponding BSE (A) DF-STEM (B) images showing the contextual overview of area 6 as labelled in Figure 2.6. (A) BSE image of a chondrule from area 6 with a prominent FGR and containing large metal inclusions with little evidence of alteration. The FGR does not display the layered structure seen in Figure 2.7 and Figure 2.12. Arrow points to the initial C deposit. (B) DF-STEM image of the lift-out showing abundant GEMS-like material. Forsterite whiskers as shown in Figure 3.10 and discussed in Section 3.3.4 are indicated by arrows. Pyrr = pyrrhotite.

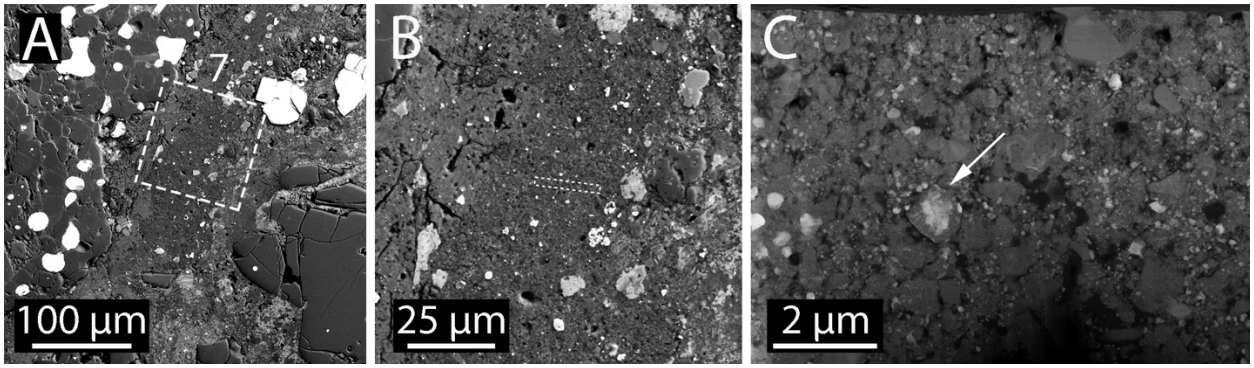

Figure 2.12: Corresponding BSE (A, B) and DF-STEM (C) images showing the contextual overview of area 7 as labelled in Figure 2.6. (A) BSE image of a metal-rich chondrule with surrounding layered FGR. (B) BSE image of the lift-out location from area 7 taken from the outer layer of the FGR. (C) DF-STEM image the lift-out showing abundant GEMS-like material. The magnetite-bearing grain with attached carbide as shown in Fig. 3.13 is indicated by the arrow.

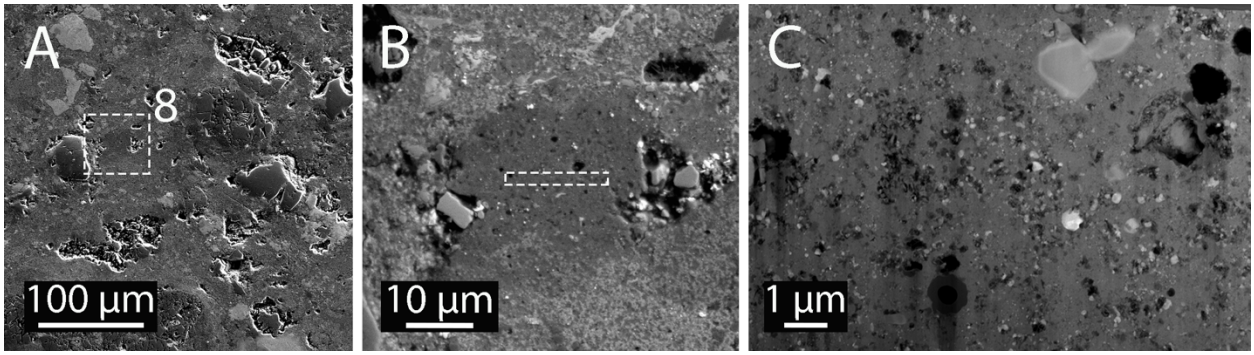

Figure 2.13: Corresponding SE (A), BSE (B), and DF-STEM (C) images showing the contextual overview of area 8 as labelled in Figure 2.6. (A) SE image of a metal-poor zone of Paris. (B) BSE image of the lift-out location from area 8. (C) DF-STEM image of the lift-out of ICM material.

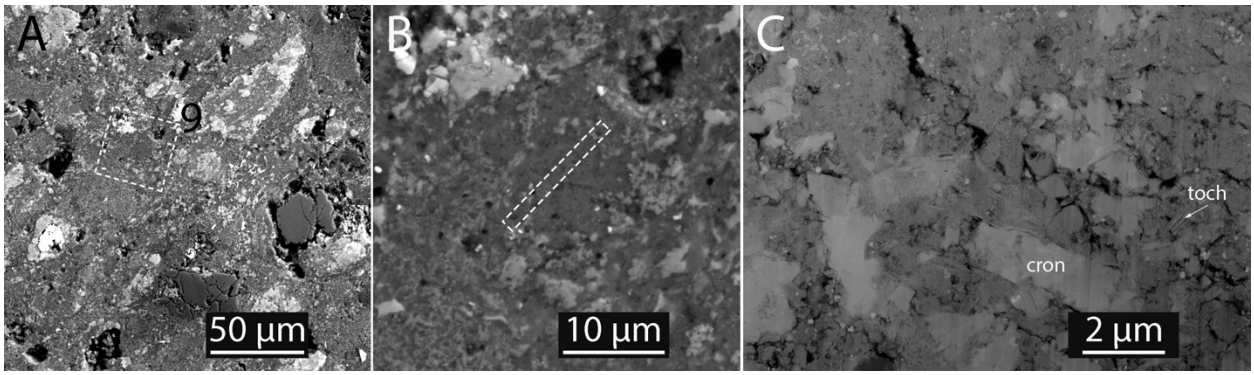

Figure 2.14: Corresponding BSE and DF-STEM images showing the location of the lift-out from area 9 as labelled in Figure 2.6. BSE and dark-field STEM images of a highly altered, metal-poor region of Paris. (A) BSE image of metal-poor zone in Paris with abundant alteration phases. (B) BSE image of the lift-out location from area 9. (C) DF-STEM image of the lift-out of ICM material. Very little GEMS-like material is found and contains large cronstedtite (cron) crystals.

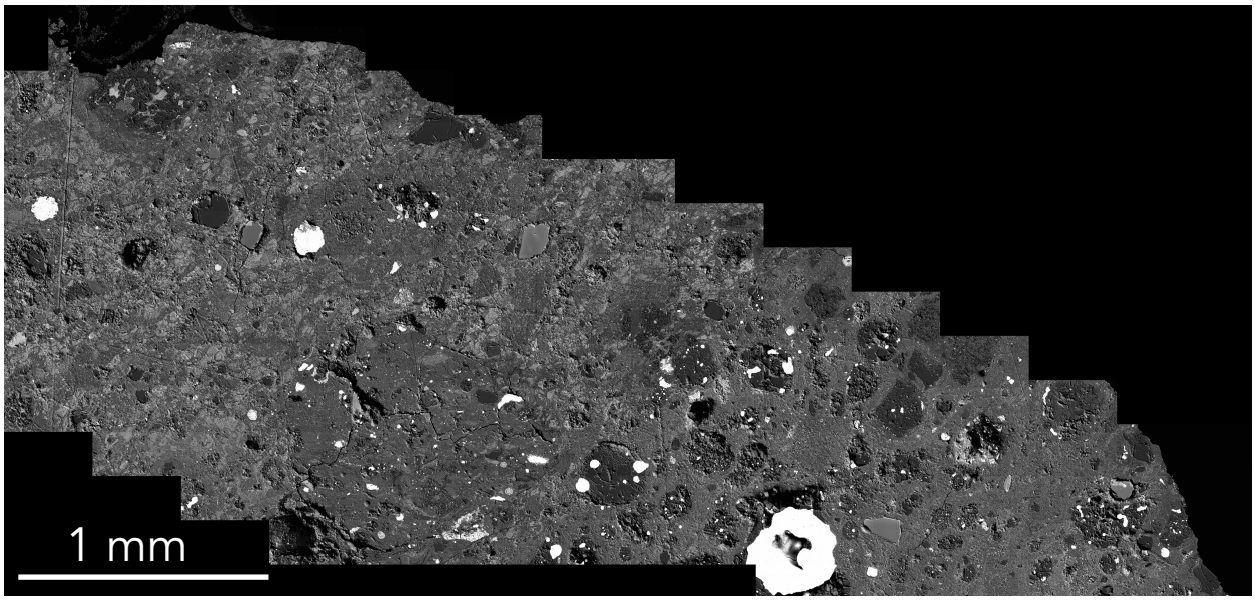

Figure 2.15: BSE image of Aguas Zarcas section. Section mapped by Katarina Keating, FMNH.

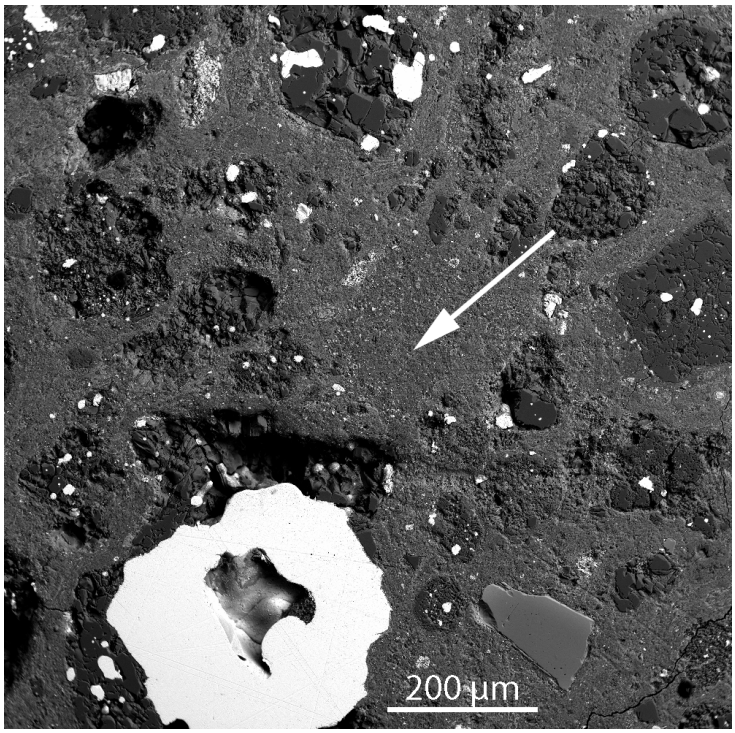

Figure 2.16: BSE image of metal-rich region of interest in Aguas Zarcas.

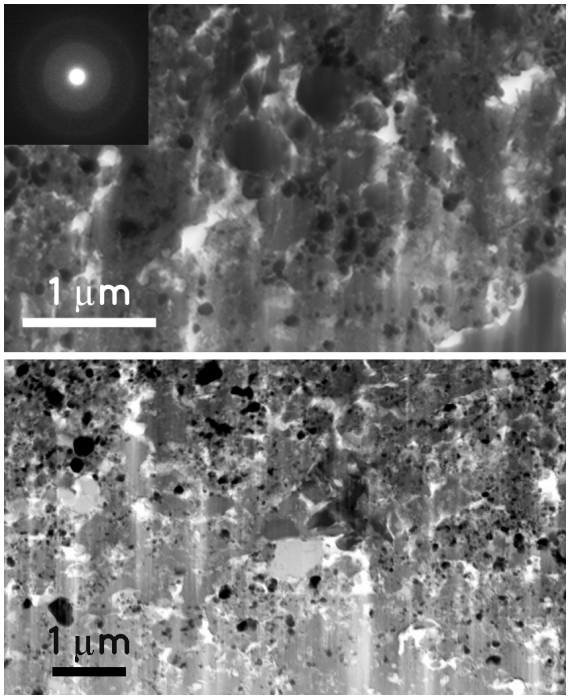

Figure 2.17: BF STEM-in-SEM mode images of Aguas Zarcas lamellae. Inset shows TEM-SAED pattern from the silicate groundmass showing that it is amorphous.

2.2.3 Acfer 094

Found in Algeria in 1990, Acfer 94 is a unique, ungrouped C2 carbonaceous chondrite (with affinities to both CM and CO chondrites) that is considered one of the least altered chondrites (Newton et al., 1995). Acfer 094 has undergone little parent-body hydrothermal processing or thermal metamorphism, as shown by its high presolar silicate abundance and preservation of 20–80 vol% amorphous silicate material. A testament to its pristinity and uniqueness, Acfer 094 has the highest presolar SiC abundance observed in any chondrite (Newton et al., 1995) and contains fossils of primordial asteroidal ice (Matsumoto et al., 2019).

Christine Floss of Washington University in St. Louis provided a mount of disaggregated and size-separated Acfer 094 matrix grains (Figure 2.18) with ten presolar silicates previously identified by NanoSIMS. Their elemental abundances measured by Auger Nanoprobe show compositions ranging from olivine to pyroxene as well as intermediate compositions. Nine of the

grains are Group 1 grains consistent with an origin in low to intermediate mass AGB stars, and one is a Group 4 grain that likely originated in a Type II SN (Refer to Nittler et al., 1997 for definitions of presolar oxide groups). See Chapter 4.2 and 4.3.

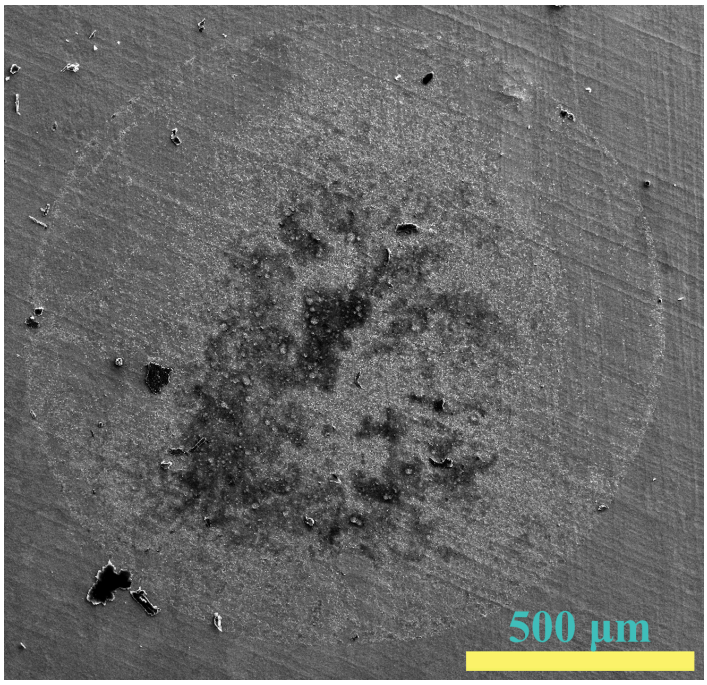

Figure 2.18: SEM image of a mount of Acfer 094 that was disaggregated by freeze-thaw. Grains were size separated by centrifugation. Grains ≤0.5µm were dispensed as a drop onto a Au foil.

Chapter 3

Search for Meteoritic GEMS: Comparison of Inclusions in Amorphous Silicates from Primitive Chondrites and from Anhydrous Chondritic Interplanetary Dust Particles

3.1 Introduction

CP-IDPs are unequilibrated aggregates of primarily sub-μm-sized crystalline and amorphous silicates bound by carbonaceous material (Figure 3.1). The crystalline silicates are predominantly forsterite and enstatite, while the amorphous silicate is predominantly GEMS—100–500 nm pseudo-euhedral grains of amorphous silicate with embedded inclusions of <50 nm metal and sulfides. GEMS have approximately chondritic bulk elemental compositions. The amorphous silicate in GEMS has predominantly pyroxene-like compositions with few GEMS exhibiting olivine-like compositions (Keller and Messenger, 2011).

The most abundant sulfides in chondritic materials are troilite (stoichiometric pyrrhotite endmember, FeS), pyrrhotite ($Fe_{1-x}S$, where $0 < x < 0.125$), and pentlandite $(Fe,Ni)_9S_8$. Pentlandite has a cubic structure (space group *Fm*3*m*), Ni contents generally >20 at%, and an Fe/Ni ratio close to 1. Ni-rich sulfides, including pentlandite, are not found in IDP GEMS or in anhydrous IDPs but are instead found in hydrated IDPs, which probably come from asteroids rather than comets (Zolensky and Thomas, 1995; Dai and Bradley, 2001). Pyrrhotites come in a complex variety of polytypes caused by different arrangements of ordered Fe vacancies leading to several "superstructures" based on the NiAs unit cell. Different pyrrhotite structures are denoted by NC notation, where N is the number of stacked NiAs cells along the crystallographic axis C. The four most Fe-enriched pyrrhotites are FeS (2C, troilite), $Fe_{11}S_{12}$ (6C), $Fe_{10}S_{11}$ (11C), and

Fe_9S_{10} (5C), while the most Fe-deficient pyrrhotite is Fe_7S_8 (4C). Pyrrhotite superstructures can have hexagonal or monoclinic symmetry. While hexagonal pyrrhotites can exist at both high and low temperatures at 1 atm, monoclinic pyrrhotite is only stable below 250 °C (Wang et al., 2006). Monoclinic pyrrhotite has been synthesized by annealing of hexagonal pyrrhotite <250 °C (Sugaki and Shima, 1965; Yund and Hall, 1969; O'Reilly et al., 2000) and by low-temperature aqueous activity (Sugaki and Shima, 1965).

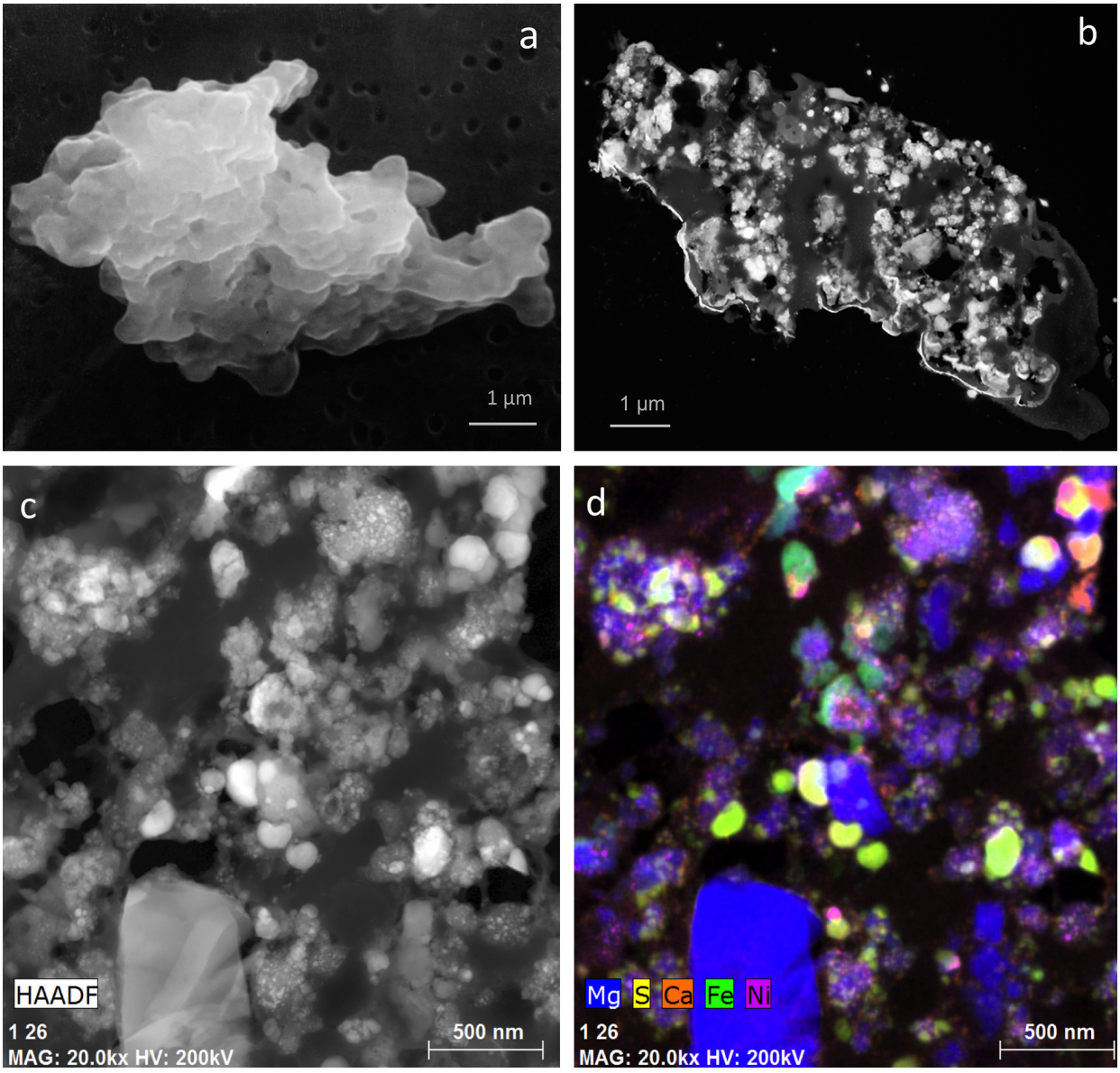

Figure 3.1: Secondary electron image (a), HAADF STEM images (b,c), and elemental map of a GEMS-rich anhydrous IDP. Images from Ishii (2019).

Previous diffraction studies on nanosulfides in anhydrous, GEMS-bearing IDPs found predominantly hexagonal pyrrhotites and an unusual cubic "spinel-like" sulfide with compositions similar to pyrrhotite (Dai and Bradley, 2001). This cubic sulfide was sometimes found intergrown with pyrrhotite and also transformed into hexagonal pyrrhotite under the electron beam during TEM analysis. This observation led Dai and Bradley (2001) to suggest that many hexagonal pyrrhotites in IDPs may be secondary thermal alteration products from atmospheric entry heating. A cubic low-Ni pentlandite (<3 at%) was also described in a hydrated IDP (Tomeoka and Buseck, 1984). It is possible that the cubic-spinel sulfide and the low-Ni pentlandite are the same phase. These cubic, low-Ni phases have not been observed elsewhere in nature, but a Ni-free pentlandite was synthesized by low-temperature (<200 °C) and low-pressure vapor-phase growth (Nakazawa et al., 1973). Only hexagonal pyrrhotite has been found within and on the surfaces of GEMS. Monoclinic pyrrhotite has been observed in cometary samples from the Stardust mission and is interpreted to be evidence of low-temperature aqueous activity on comet Wild 2. This interpretation is corroborated by the presence of orthorhombic cubanite ($CuFe_2S_3$) in Stardust samples, another low-temperature sulfide that has previously only been observed in CI chondrites (Berger et al., 2011). The previous study by Leroux et al. (2015) was not able to determine the crystallographic nature of the nanosulfides in Paris.

Sulfides with elemental compositions between and inclusive of pyrrhotite and pentlandite have been observed in hydrated IDPs and coarse-grained sulfides in CM chondrites (Zolensky et al., 2002; 2008). The intermediate compositions follow the trend of monosulfide solid solution. While hydrated IDPs show a smooth distribution between pyrrhotite and pentlandite elemental compositions, coarse-grained sulfides from other CM chondrites do not commonly have intermediate compositions. The origin of these intermediate sulfides is unclear, but they appear to be a distinct phase (see below, Section 5.1).

Kamacite (α-Fe,Ni) is the other abundant nanoscale phase found embedded in GEMS from IDPs. Kamacite is also observed in GEMS-like objects in UCAMMs but is less abundant than in IDP GEMS (Dobrică et al., 2012). Leroux et al. (2015) reported a number of seemingly S-free and Fe-rich inclusions in Paris, but, due to their small sizes (<30 nm), it was not possible to conclusively determine by EDS or SAED whether they were metal, oxide, or another phase.

3.2 Methods

As described in Section 2.1.1, section 2010-1 of the Paris meteorite was provided by the Muséum National d'Histoire Naturelle in Paris. Nine lamellae were lifted out and thinned using the TESCAN LYRA3 focused ion beam scanning electron microscope at the University of Chicago; final thinning to electron transparency was carried out using the FEI Helios NanoLab 660 FIB instrument at the University of Hawai'i at Mānoa just before TEM analyses. Preliminary BSE and EDS mapping was used to assess the alteration state of different lithologies in Paris: areas were assigned a petrologic type of ~2.9 where the ICM contained few alteration phases (such as magnetite, phyllosilicates, tochilinite, or cronstedtite) and where metal grains showed minimal signs of corrosion at their peripheries, while areas containing few metal grains and abundant alteration phases were assigned a petrologic type of ~2.7. Areas of interest were chosen from a range of petrographic settings with possibly different formation histories and varying degrees of aqueous alteration, including two lamellae from the more highly altered ICM (metal-poor) regions, four from more pristine (metal-rich) ICM regions, two from the outer portions of FGRs surrounding metal-rich chondrules, and one from the inner portion of a layered FGR surrounding a metal-rich chondrule (Figures 2.1–2.9 and 3.2). Even in metal-poor zones, care was taken to sample fine-grained materials and to avoid discernable alteration phases.

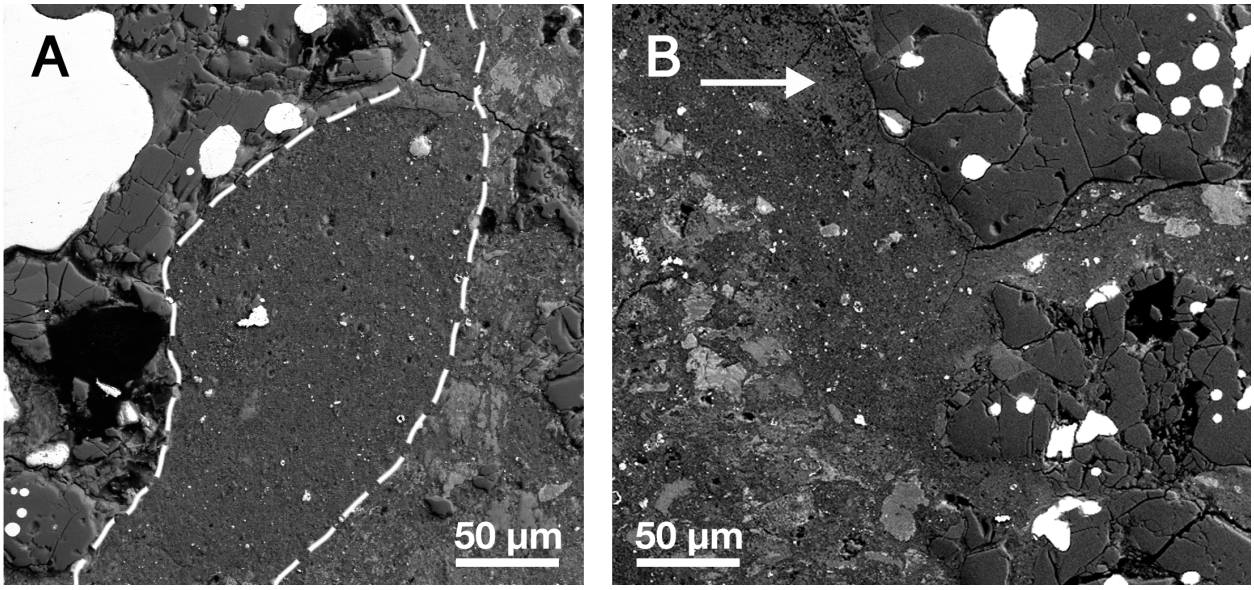

Figure 3.2: BSE images of Paris chondrules with surrounding FGRs. A) Dashed lines delineate the rough outline of a metal-rich chondrule (left) and where the FGR material meets the ICM (right). This FGR does not have multiple layers of material. B) Arrow points to an additional, interior layer of material within the FGR immediately surrounding a metal-rich chondrule. Metal appears white in these images.

As described in Section 2.1.2, a section of Aguas Zarcas, FMNH ME 6111.20, from a prerain specimen was polished with water-free isopropanol and diamond lapping film at the Field Museum of Natural History (FMNH) and stored in dry conditions in low vacuum. The section was first analyzed using a Zeiss Evo 60 scanning electron microscope (SEM) with an Oxford XMax 50 EDS system at the FMNH to find suitable regions that may preserve pristine material. The areas of interest were chosen from a fine-grained region of the ICM adjacent to metal-rich chondrules and avoiding alteration phases (Figure 2.11). Two electron-transparent lamellae were lifted out and thinned using a TESCAN LYRA3 FIB-SEM at the University of Chicago. Preliminary analysis was done using STEM-in-SEM mode at 30 kV and follow up work (SAED and EDS) was done at 300 and 200 kV using the JEOL JEM-3010 and JEOL JEM-ARM200CF, respectively, at the University of Illinois at Chicago (Figure 2.12).

Clast LT29 from the GEMS-rich CP-IDP U220GCA was selected for comparison with the GEMS-like material in Paris. LT29 is a nonporous, compact, red-brown organic carbon clast from a giant cluster particle that was embedded in epoxy and ultramicrotomed to 40–70 nm thickness. Due to its compact (less porous) nature, the epoxy (distinguishable by lack of N) did not significantly infiltrate its interior.

The Paris sections were examined using the FEI 60-300 keV High-base Titan3 G2 (scanning) transmission electron microscopy (S)TEM instrument equipped with an EDAX Genesis 4000 Si(Li) solid-state X-ray energy-dispersive spectrometer at the University of Hawai‘i at Mānoa. Aguas Zarcas sections were examined using the JEOL JEM-3010 at the University of Illinois at Chicago in order to confirm the presence of amorphous silicate and determine the chemistry of phases present. The sections were imaged using both conventional bright-field and HAADF modes at 300 kV (University of Hawai‘i at Mānoa) or 200 kV (University of Illinois at Chicago) accelerating voltage. Elemental compositions were measured by EDS, while crystallographic information was acquired by electron diffraction, either nanodiffraction for nanoscale phases or SAED for larger phases (note: nanodiffraction was only performed on Paris samples). In some cases, high-magnification lattice-fringe images were also acquired. Diffraction spacings were calibrated *in-situ* against polycrystalline Pt and were determined using the ImageJ software (Schindelin et al., 2015), and crystal structure identifications were confirmed using simulated patterns generated with CrystalMaker (CrystalMaker Software Ltd.; www.crystalmaker.com). EDS spectra were quantified using a thin-film X-ray correction procedure (Longo et al., 1999) to obtain normalized element abundances of O, Mg, Al, Si, S, Ca, Cr, Fe, and Ni. Experimental correction or “K” factors used for the quantifications were calibrated against standards of known composition, including the NIST SRM 2063 thin-film glass standard, San Carlos olivine, and Johnstown pyroxene. Depending primarily on counting statistics in individual spectra, the relative abundances of major

elements (>25 at%) are generally accurate to within ±2.5%, and minor elements (5–20 at%) to within ±25%. High spatial resolution EDS maps were acquired using the FEI TitanX 60-300 microscope at the Molecular Foundry at Lawrence Berkeley National Laboratory. The TitanX has 4 Bruker silicon drift detectors providing 140 eV energy resolution at Mn Kα and approximately 0.7 sr solid angle for X-ray collection. Data were collected using Esprit 1.9 software (Bruker Corporation) with a full X-ray fluorescence spectrum at each pixel and simultaneous collection of a HAADF image.

3.3 Results

3.3.1 Morphological observations

The GEMS-like material previously observed in Paris by Leroux et al. (2015) was found in all of our sections, including small areas from the more altered (~CM 2.7), metal-poor zones (Figures 2.8 and 2.9). GEMS-like material has also been identified for the first time in Aguas Zarcas: SAED confirms the presence of abundant amorphous silicate throughout the FIB section of Aguas Zarcas (see Figure 2.12, inset) and EDS confirms the presence of Fe- and S-bearing inclusions embedded in the amorphous silicate.

GEMS- like material was also found in microtomed sections of Paris and Acfer 094 studied by Ohtaki et al. (2021). The GEMS-like material is therefore native to Paris and Aguas Zarcas and not a FIB-induced artifact. The GEMS-like material is compositionally close to chondritic in chemical composition and consists of sub-μm amorphous silicate units with abundant Fe-bearing nanoparticles. The amorphous material is often intimately intermixed with hydrated phases such as tochilinite and cronstedtite, particularly in sections lifted from the metal-poor ICM but also in metal-rich ICM (e.g., Figure 3.3). These hydrated phases are noticeably less abundant in sections

lifted from FGRs. None of the amorphous domains enclosed crystalline cores such as those observed in some IDP GEMS (Bradley and Dai, 2004; Keller and Messenger, 2011).

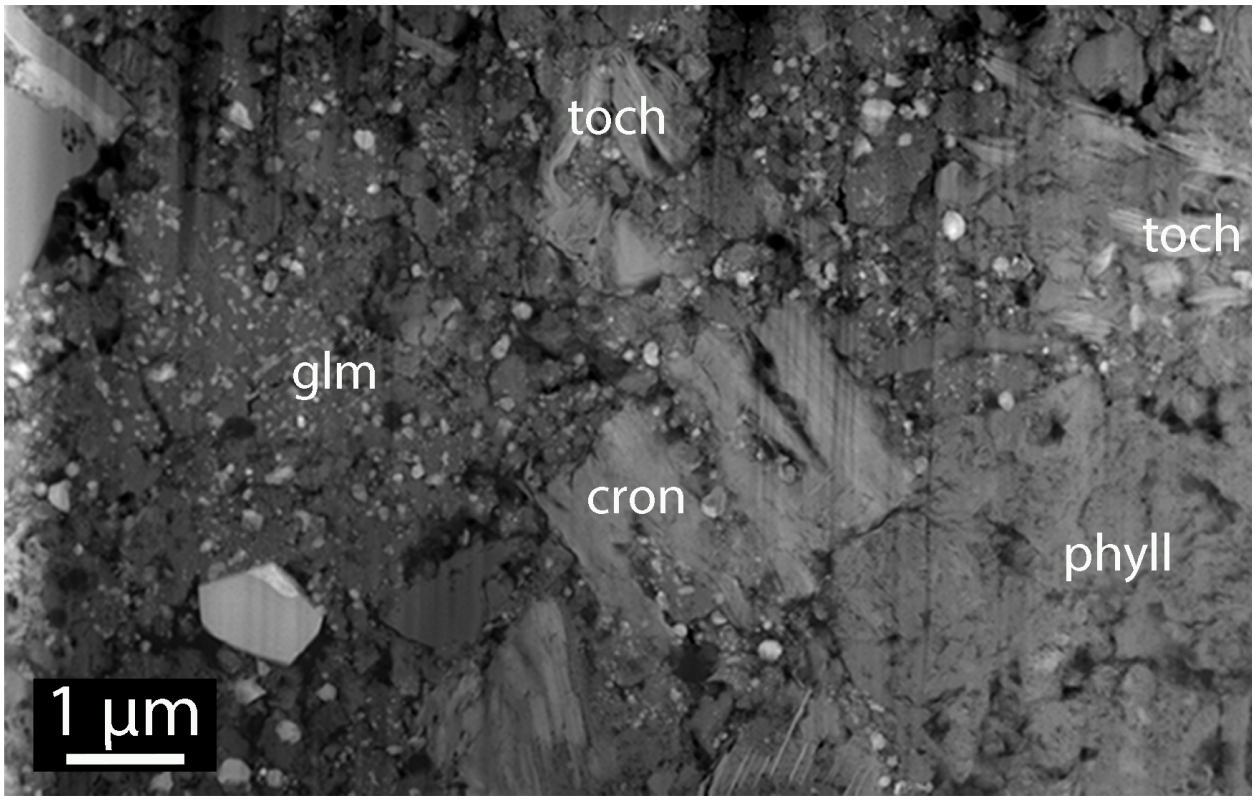

Figure 3.3: DF-STEM image of the lift-out from ICM region. GEMS-like material (glm) is directly adjacent to hydrated phases, such as tochilinite (toch), cronstedite (cron), and phyllosilicates (phyll).

The least-altered sections from the metal-rich (~CM2.9) regions in Paris contain generally smaller and more abundant nanophase particles throughout the lamellae and within amorphous silicate regions. The more aqueously altered samples from the metal-poor (~CM2.7) regions in Paris have far fewer nanoparticles overall, even where amorphous silicate is present. The outer or single-layered FGR material surrounding metal-rich chondrules appears to preserve a higher abundance of nanophase particles. The diameters of the embedded nanoparticles range from 9 to 166 nm, with averages of 32 nm in FGRs, 40 nm in metal-rich ICM, and 57 nm in metal-poor ICM. Within GEMS from IDP U220GCA, inclusions range in diameter from 4 to 64 nm with an

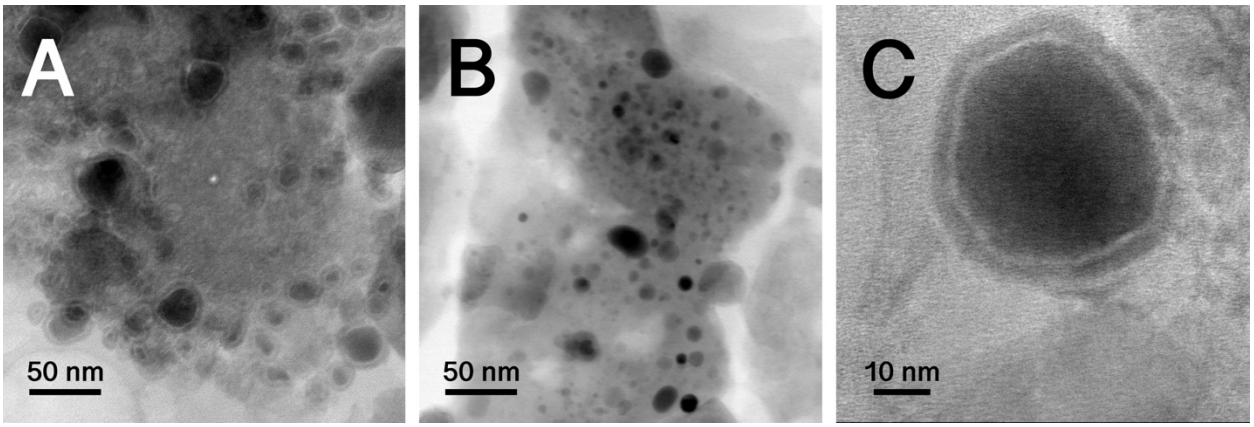

Figure 3.4: Bright-field images comparing GEMS-like material in Paris (A) and GEMS from IDP U220GCA LT29 (B). A rimmed nanoparticle from Paris is shown in C. Material shown in A and C derive from the FGR shown in Figure 2.11. Note that all nanoparticles in Paris are rimmed and those in the IDP are not.

average of 15 nm. The smallest grain-size fraction (<10 nm) seen in IDP GEMS are either absent or significantly underrepresented in all sections of Paris and Aguas Zarcas.

Nanoparticles are rounded or partially rounded objects with only rare grains showing euhedral-subhedral shapes. Many nanoparticles in both Paris and Aguas Zarcas also have conspicuous rims that are either absent or minimal in IDPs (Figure 3.4). Rims are enriched in O and depleted in Fe compared to the interior particle. Rims do not appear to be thicker in the more aqueously altered samples. Rims are not continuous with the nanoparticles, but instead are separated by an ~1 nm thick gap of low-Z material. Nanotubes of tochilinite with cylindrical morphologies were also observed (Figure 3.5).

3.3.2 Identification of metal

While kamacite is found in all GEMS from IDPs (Bradley, 1994; Dai and Bradley, 2001; Keller and Messenger, 2011), we have not identified any grains with diffraction patterns consistent with kamacite that appear to be embedded in the amorphous silicate matrix of Paris. Some grains with EDS spectra suggestive of FeNi metal have diffraction patterns inconsistent with metal and, instead, are identified as carbides or oxides, demonstrating the problem with relying on EDS

spectra alone in identifying nanoscale phases. Further work needs to be conducted to determine if nanophase metal grains reside in Aguas Zarcas amorphous silicate. Rare kamacite grains were identified in Paris that were not visibly embedded within the amorphous silicate domains (Figures 3.6 and 3.7). These metal grains ranged in size from 10 to 30 nm in diameter, larger than those found in IDP GEMS, which can range in size down to a few nm (Bradley, 2014). Some of these metal grains are embedded in enstatite crystals or associated with sulfide grains (Figure 3.7). All metal grains have O-rich rims (Figure 3.6E). Too few metal grains were observed to determine if there is a difference in metal abundance between the ICM and FGRs.

3.3.3 Sulfide compositions and mineralogy

Sulfides are the most abundant phases observed at the nanoscale in Paris and Aguas Zarcas GEMS-like materials. Sulfide elemental compositions as measured by EDS in Paris are shown on an Fe-Ni-S ternary diagram (Figure 3.8) and listed in Table 3.1. Using nanodiffraction, we confirmed crystallographically that the nanophase sulfides in Paris include pentlandite as well as both hexagonal and monoclinic pyrrhotite polytypes (Figure 3.9 and Table 3.1). All EDS measurements are likely skewed toward more Fe-rich compositions due to overlap of the surrounding Fe-bearing (silicate) groundmass. Because of this, Ni-free, stoichiometric FeS compositions consistent with troilite may instead be pyrrhotite. Superlattice reflections that could differentiate between troilite (2C, hexagonal) and other hexagonal pyrrhotite superstructures were not observed in any of the patterns. The S and Ni concentrations within the amorphous silicate groundmass are <~0.5 at%, and thus nanoparticle compositions are only minimally skewed with respect to S or Ni due to beam overlap.

Ni-poor, highly Fe-enriched sulfides (Fe > 50 at%) that have compositions more Fe-rich than troilite are seen in all sections. These grains have elemental compositions consistent with

tochilinite. However, one highly Fe-enriched grain from the metal-poor ICM indexed as monoclinic pyrrhotite. Monoclinic pyrrhotite is the most Fe-depleted pyrrhotite phase, which demonstrates that the Fe measured by EDS in nanophase sulfides is at least partially and often significantly derived from the surrounding material. This also underscores the importance in using crystallographic methods for unambiguous nanoscale phase identifications.

Both pyrrhotite and pentlandite were observed in every section. Ni-poor sulfides are more abundant than Ni-rich sulfides in all sections except those from the metal-poor ICM. The abundance of Ni-free or Ni-poor sulfides is higher in the least altered Paris sections than in the more highly altered sections of Paris. In particular, Ni-free and Ni-poor sulfides are more abundant in FGRs than in ICM. A Mann-Whitney U test (Mann and Whitney, 1947) confirms that the FGR and ICM nanosulfide populations are statistically different beyond 2σ. Pentlandite was found even in the least altered sections. Of the only five nanophase sulfides from metal-poor ICM measured by EDS, two had elemental compositions consistent with pentlandite, while the other three had compositions with large Fe enrichments. Several sulfides also show compositions intermediate between pyrrhotite and pentlandite. While some of these grains may be intergrowths of pyrrhotite and pentlandite, analysis by bright- and dark-field imaging as well as lattice-fringe imaging show that some of these grains with intermediate composition are single-phase grains. The crystal structures from the intermediate sulfides unfortunately could not be determined from nanodiffraction patterns, and it is therefore undetermined if their crystal structures are related to pyrrhotite or pentlandite, or another phase.

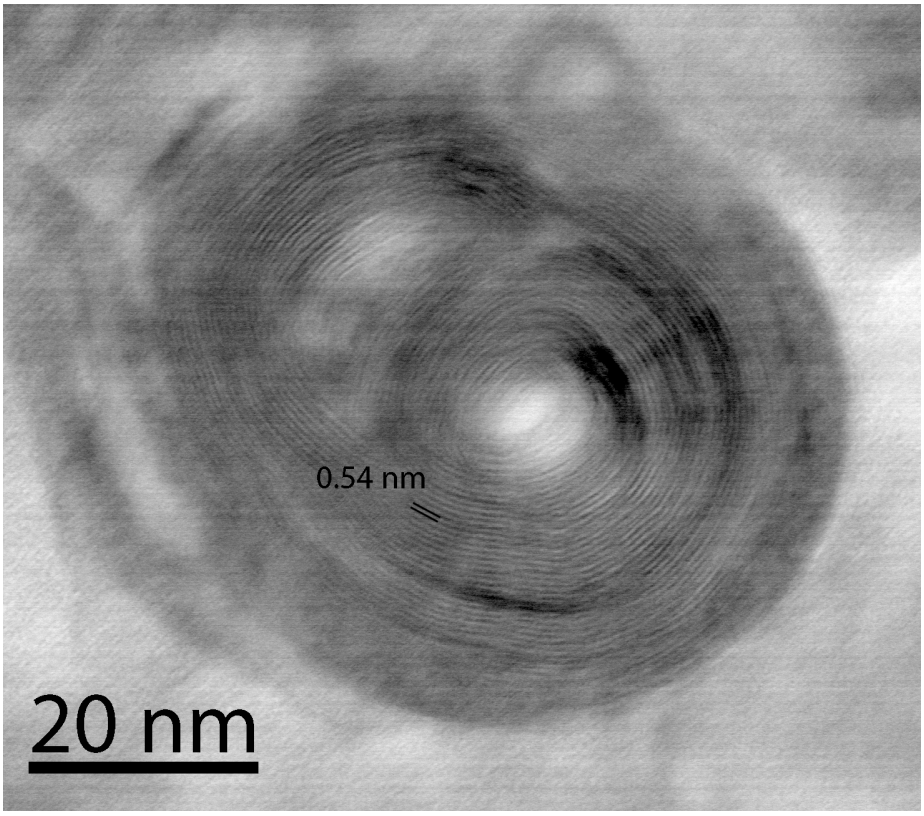

Figure 3.5: High-resolution TEM image of a cylindrical tochilinite nanotube with characteristic (002) lattice spacing of 0.54 nm from a metal-rich (~CM2.9) ICM region of Paris.

Table 3.1: Fe-Ni-S (at%) compositions of nanophase sulfides in Paris. Phase identifications based on stoichiometry except for crystal structures determined using nanodiffraction (in bold). n.d. = not detected. Petrologic types determined from BSE and EDS maps, with metal-rich/phyllosilicate-poor regions being designated ~2.9 and metal-poor/phyllosilicate-rich regions being designated as ~2.7.

Region	Fe (at%)	Ni (at%)	S (at%)	Phase
CM2.7 ICM	31.66 ± 0.99	21.11 ± 0.88	47.21 ± 0.82	Pentlandite
	45.92 ± 1.08	18.73 ± 0.69	35.34 ± 0.63	Pyrrhotite
	29.02 ± 0.85	23.73 ± 0.78	47.23 ± 0.72	Pentlandite
	65.41 ± 0.94	0.30 ± 0.11	34.27 ± 0.45	Pyrrhotite
	61.35 ± 0.88	0.52 ± 0.10	38.11 ± 0.47	**Pyrrhotite, monoclinic**
CM2.9 ICM	42.08 ± 0.64	4.72 ± 0.22	53.19 ± 0.47	Pyrrhotite
	49.14 ± 0.49	0.96 ± 0.07	49.89 ± 0.34	Pyrrhotite
	51.27 ± 0.55	0.23 ± 0.05	48.48 ± 0.36	Pyrrhotite
	51.16 ± 0.65	0.38 ± 0.08	48.45 ± 0.43	Pyrrhotite
	43.60 ± 0.51	4.90 ± 0.18	51.49 ± 0.39	Pyrrhotite
	57.56 ± 0.56	1.85 ± 0.11	40.58 ± 0.33	Pyrrhotite
	45.12 ± 0.58	0.46 ± 0.07	54.40 ± 0.43	Pyrrhotite
	52.72 ± 0.69	0.41 ± 0.08	46.85 ± 0.44	Pyrrhotite
	18.08 ± 0.24	32.58 ± 0.35	49.32 ± 0.28	Pentlandite
	42.89 ± 0.38	9.15 ± 0.17	47.95 ± 0.28	Pyrrhotite
	57.61 ± 1.21	7.35 ± 0.45	35.02 ± 0.66	Pyrrhotite
	53.19 ± 2.72	n.d.	46.80 ± 1.73	**Tochilinite**
	41.36 ± 3.29	4.64 ± 1.68	53.98 ± 2.51	**Pyrrhotite, hexagonal**
	21.67 ± 1.84	28.11 ± 2.22	50.21 ± 1.81	**Pentlandite**
	27.70 ± 1.45	23.49 ± 1.41	48.79 ± 1.28	**Pentlandite**
	27.58 ± 1.45	23.32 ± 1.42	49.09 ± 1.30	**Pentlandite**
	20.10 ± 0.75	29.01 ± 0.92	50.87 ± 0.79	Pentlandite
	25.75 ± 0.75	22.06 ± 0.65	52.17 ± 0.71	Pentlandite
	53.70 ± 0.80	0.26 ± 0.10	46.02 ± 0.51	Pyrrhotite
	46.58 ± 0.85	3.66 ± 0.30	49.74 ± 0.63	Pyrrhotite
	38.30 ± 0.70	12.73 ± 0.46	48.95 ± 0.55	Pyrrhotite
	59.98 ± 0.92	1.15 ± 0.13	38.86 ± 0.50	Pyrrhotite
	47.94 ± 0.71	1.27 ± 0.13	50.78 ± 0.49	Pyrrhotite
	49.44 ± 1.29	0.50 ± 0.26	50.04 ± 0.87	Pyrrhotite
	47.67 ± 0.38	3.61 ± 0.12	48.71 ± 0.26	Pyrrhotite
	32.28 ± 0.44	23.17 ± 0.39	44.54 ± 0.34	Pentlandite
	23.88 ± 0.47	17.76 ± 0.41	58.35 ± 0.46	Pentlandite
	28.01 ± 0.40	15.23 ± 0.32	56.74 ± 0.37	Pyrrhotite
	38.01 ± 0.37	16.03 ± 0.28	45.95 ± 0.30	Pyrrhotite
CM2.9 FGR Outer Layer	30.85 ± 0.48	24.06 ± 0.44	45.07 ± 0.38	Pentlandite
	39.26 ± 1.44	16.12 ± 1.05	44.60 ± 1.03	Pyrrhotite
	42.58 ± 0.90	4.08 ± 0.33	53.32 ± 0.67	Pyrrhotite
	23.59 ± 0.59	27.18 ± 0.68	49.22 ± 0.55	Pentlandite
	56.86 ± 1.14	0.91 ± 0.20	42.21 ± 0.69	Pyrrhotite
	52.10 ± 0.95	n.d.	47.89 ± 0.67	Pyrrhotite
	49.31 ± 1.18	0.87 ± 0.47	49.80 ± 0.90	Pyrrhotite
	42.90 ± 0.52	n.d.	57.09 ± 0.38	Pyrrhotite
	24.64 ± 0.35	26.24 ± 0.37	49.10 ± 0.32	Pentlandite
	54.54 ± 0.52	2.20 ± 0.13	43.25 ± 0.32	Pyrrhotite
	45.19 ± 0.50	1.94 ± 0.12	52.86 ± 0.37	Pyrrhotite
	45.84 ± 0.44	n.d.	54.15 ± 0.32	Pyrrhotite
	45.89 ± 0.40	0.18 ± 0.03	53.92 ± 0.30	Pyrrhotite
	45.63 ± 0.46	0.22 ± 0.04	54.13 ± 0.35	Pyrrhotite
	50.46 ± 0.70	1.42 ± 0.16	48.10 ± 0.46	Pyrrhotite
	54.78 ± 0.54	3.07 ± 0.13	42.14 ± 0.33	Pyrrhotite
	24.62 ± 0.36	23.39 ± 0.37	51.98 ± 0.31	Pentlandite
	48.87 ± 0.46	2.78 ± 0.11	48.34 ± 0.30	**Pyrrhotite, hexagonal**
	46.04 ± 0.90	n.d.	53.95 ± 0.65	Pyrrhotite
	55.42 ± 1.08	1.07 ± 0.22	43.50 ± 0.66	Pyrrhotite
	47.09 ± 0.77	n.d.	52.90 ± 0.56	Pyrrhotite
	45.42 ± 1.04	0.27 ± 0.17	54.29 ± 0.77	Pyrrhotite
	49.59 ± 0.95	n.d.	50.40 ± 0.68	Pyrrhotite
	44.41 ± 0.63	n.d.	55.58 ± 0.48	Pyrrhotite
	48.45 ± 0.67	0.40 ± 0.08	51.14 ± 0.47	Pyrrhotite
	44.04 ± 0.48	3.57 ± 0.15	52.37 ± 0.35	Pyrrhotite
	35.72 ± 0.55	13.20 ± 0.35	51.07 ± 0.44	Pyrrhotite
	46.38 ± 0.57	n.d.	53.61 ± 0.41	Pyrrhotite
	50.07 ± 0.63	n.d.	49.92 ± 0.43	Pyrrhotite
	48.86 ± 0.64	n.d.	51.13 ± 0.44	Pyrrhotite
	44.91 ± 0.88	4.02 ± 0.32	51.06 ± 0.65	Pyrrhotite
	44.69 ± 1.18	1.90 ± 0.28	53.39 ± 0.86	Pyrrhotite
	44.98 ± 0.71	n.d.	55.01 ± 0.55	Pyrrhotite
	58.50 ± 0.63	1.68 ± 0.07	39.81 ± 0.36	Pyrrhotite
	47.53 ± 0.53	0.04 ± 0.04	52.42 ± 0.39	Pyrrhotite
	35.67 ± 1.85	20.18 ± 1.51	44.14 ± 1.37	**Pentlandite**
	28.99 ± 0.92	25.16 ± 0.95	45.83 ± 0.81	**Pentlandite**
	40.45 ± 1.84	1.00 ± 0.54	58.54 ± 1.47	**Pyrrhotite, monoclinic**
	30.68 ± 0.79	20.46 ± 0.71	48.85 ± 0.70	Pentlandite
	47.88 ± 0.89	9.90 ± 0.42	42.21 ± 0.59	Pyrrhotite
	42.33 ± 0.88	3.25 ± 0.27	54.41 ± 0.69	Pyrrhotite
	42.10 ± 0.81	11.84 ± 0.49	46.04 ± 0.61	Pyrrhotite
	27.10 ± 0.90	16.46 ± 0.74	56.43 ± 0.86	Pentlandite
	60.84 ± 0.46	0.82 ± 0.06	38.32 ± 0.25	Pyrrhotite
	46.23 ± 0.75	2.88 ± 0.21	50.88 ± 0.52	Pyrrhotite
CM2.9 FGR Inner Layer	47.36 ± 1.89	1.01 ± 0.52	51.61 ± 1.32	**Pyrrhotite, hexagonal**
	29.13 ± 1.42	22.94 ± 1.38	47.91 ± 1.22	**Pentlandite**

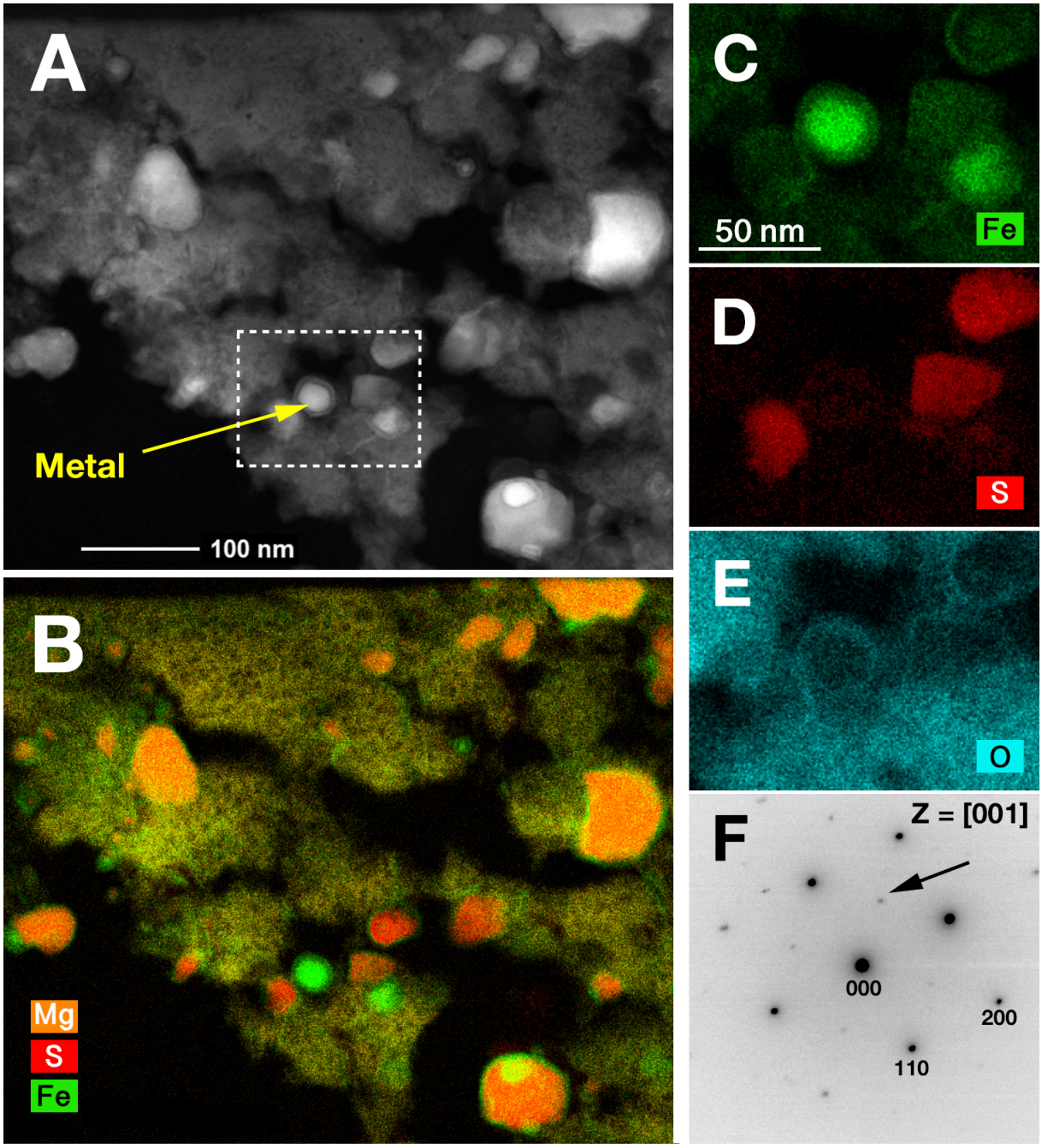

Figure 3.6: STEM imaging and EDS maps of another amorphous silicate region of an FGR containing a nanophase metal grain associated with sulfide. (A) Darkfield STEM image. Dashed rectangle refers to the field-of-view in panels C–E; (B) Combined Mg (orange), S (red), Fe (green) elemental map; (C) Fe elemental map; (D) S elemental map; (E) O (cyan) elemental map; (F) Nanodiffraction pattern from metal grain. Indexing is consistent with [001] kamacite with weaker reflections from the O-rich rim that are consistent with [001] magnetite (arrowed).

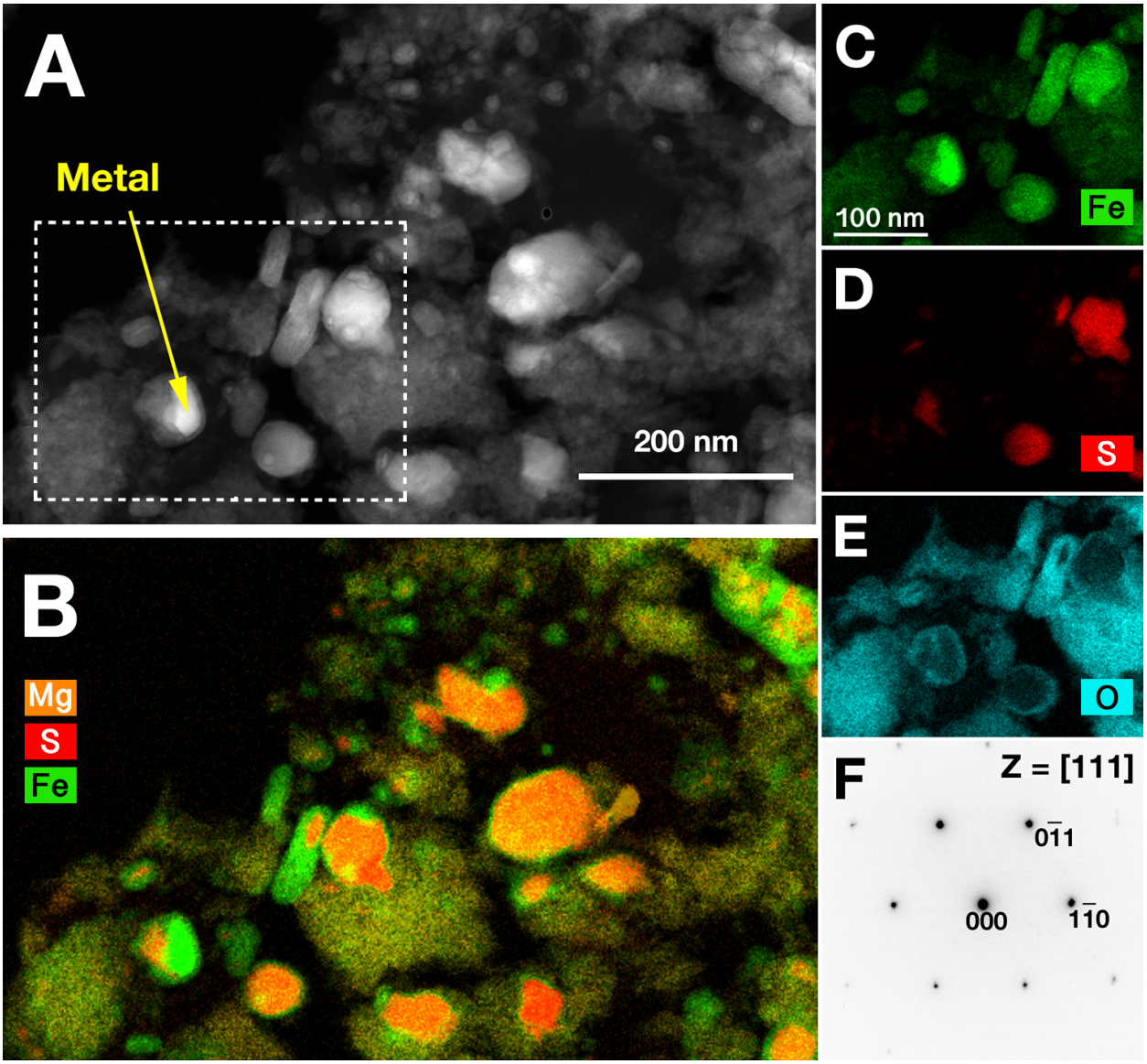

Figure 3.7: STEM imaging and EDS maps of another amorphous silicate region of an FGR containing a nanophase metal grain associated with sulfide. (A) Darkfield STEM image. Dashed rectangle refers to the field-of-view in panels C–E; (B) Combined Mg (orange), S (red), Fe (green) elemental map; (C) Fe elemental map; (D) S elemental map; (E) O (cyan) elemental map; (F) Nanodiffraction pattern from metal grain. Indexing is consistent with kamacite.

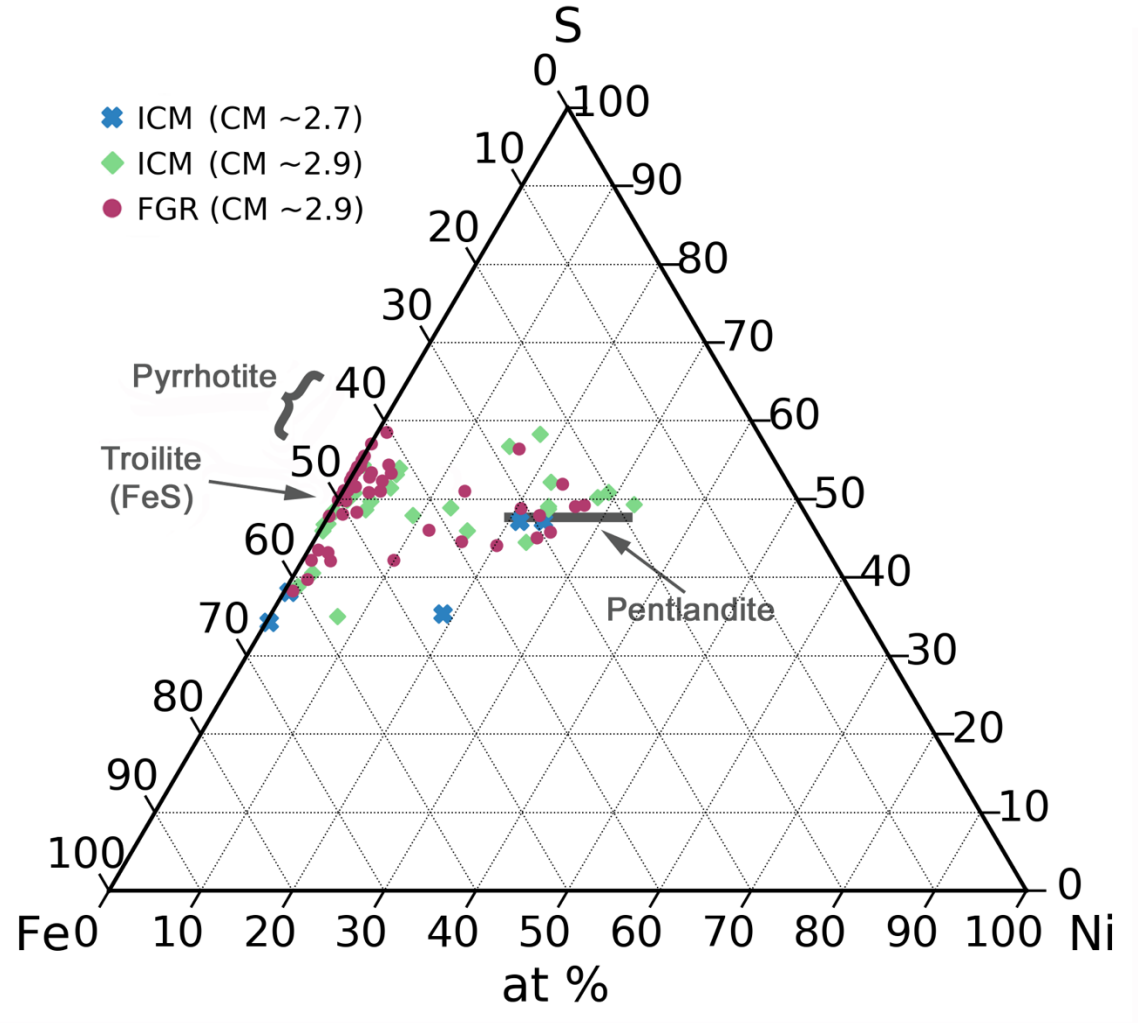

Figure 3.8: Compositions of nanophase sulfides in Paris obtained by EDS. Blue crosses: ICM sulfides from the more highly altered areas of Paris (~2.7 petrologic type). Nanoparticles are far less abundant in the heavily altered ICM. Green diamonds: ICM sulfides from the more pristine areas of Paris (~2.9 petrologic type). Red circles: Sulfides from FGR. Please refer to Zolensky et al. (2002; 2008) for comparisons to IDP sulfides and coarse-grained sulfides in CM chondrites, respectively.

3.3.4 Other accessory phases

The least aqueously altered ICM section contained a crystalline silicate morphologically and chemically similar to an enstatite whisker as commonly found in CP-IDPs (Figure 3.10C). One lamella from the outer layer of a chondrule FGR contained two forsterite whiskers (Figure 3.10A and B). Leroux et al. (2015) also observed enstatite and forsterite whiskers in Paris. Neither forsterite whiskers of our study nor those from Leroux et al. (2015) show evidence of stacking faults

or screw dislocations, which are typically observed in enstatite whiskers and are indicative of vapor-phase growth. As also reported by Leroux et al. (2015), the enstatite whisker shows evidence of partial alteration with the surrounding matrix, while the forsterite whiskers do not, suggesting that forsterite is more resistant to alteration. This is consistent with previous aqueous alteration experiments (Ohnishi and Tomeoka, 2007). However, the forsterite whiskers were found in the same highly pristine FGR section, while the enstatite whisker was found in an ICM section (albeit the least altered of the ICM sections in this study). This might also explain the discrepancy in their

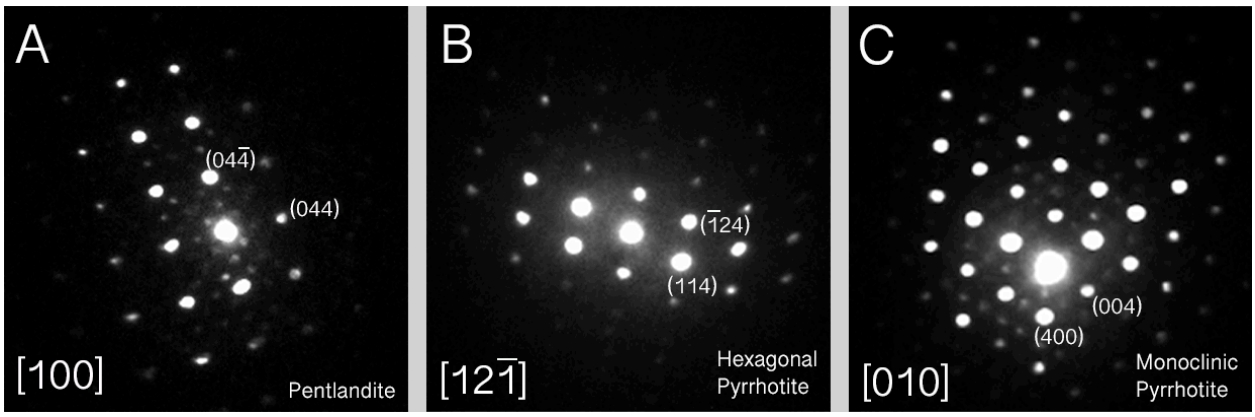

Figure 3.9: Nanodiffraction patterns from a pentlandite (A), hexagonal pyrrhotite (B), and monoclinic pyrrhotite (C) observed in Paris. The pentlandite shown here was observed in the ICM of a metal-rich region of Paris. The hexagonal pyrrhotite shown here was observed in the inner layer of a double-layered FGR. The monoclinic pyrrhotite shown here was observed in a single-layered FGR.

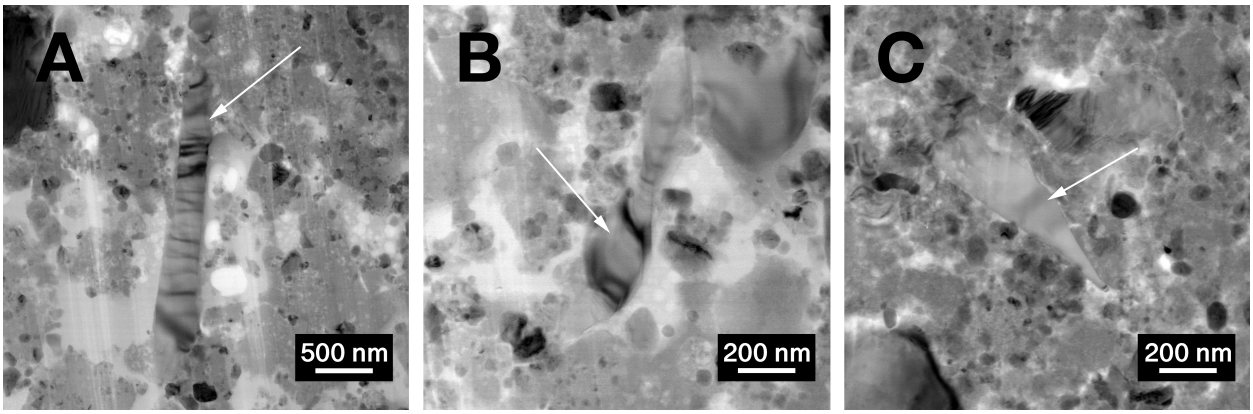

Figure 3.10: Bright-field TEM images of silicate whiskers, indicated by arrows. (A) Forsterite whisker with rod morphology. (B) Forsterite whisker with unusual bowling-pin shape. (C) Enstatite whisker with ribbon morphology. Bragg extinction contours are seen as horizontal, dark stripes across whiskers. Forsterite whiskers shown in A and B are from the FGR shown in Figure 2.11. The enstatite whisker shown in C was found in the metal-rich ICM region shown in Figure 2.8.

alteration states in our study as the FGRs show less evidence of aqueous alteration. The lamella from an inner FGR contained an enstatite platelet.

The forsterite whisker in Figure 3.10A shows a conventional ribbon-shaped morphology. The whisker shown in Figure 3.10B has an unusual bowling-pin shape. Both forsterite whiskers contained variable MnO and FeO contents throughout the grains. The whisker shown in Figure 3.10A has MnO concentrations ranging from 0.12 to 0.85 wt%, FeO concentrations ranging from 0.09 to 3.86 wt%, and FeO/MnO ratios ranging from 0.23 to 9.96 (MnO and FeO concentrations are not spatially correlated). Some areas throughout the whisker had low-iron, manganese-enriched (LIME) compositions, where LIME silicates have FeO/MnO ratios <1 and often contain MnO concentrations above 0.5 wt% in contrast to typical ferromagnesian silicates found in undifferentiated meteorites. Two lamellae from the metal-rich ICM contained areas with numerous LIME olivines and pyroxenes (Figure 3.11). LIME silicates have not been previously reported in Paris.

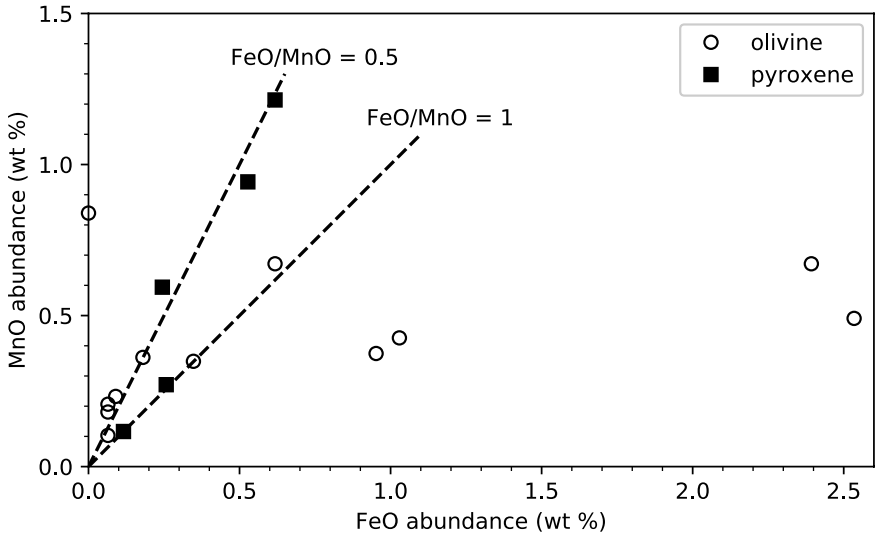

Figure 3.11: FeO and MnO abundances of mafic silicates in Paris. LIME silicates are defined as those with FeO/MnO < 1. All silicates shown here derive from the metal-rich ICM regions shown in Figure 2.9 and Figure 2.10.

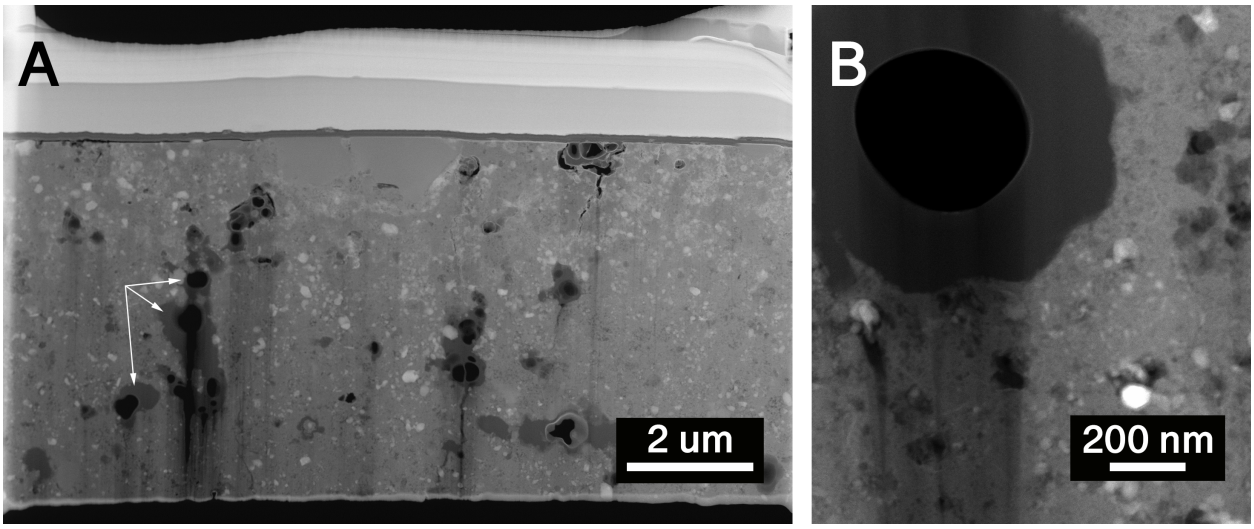

Figure 3.12: Dark-field TEM image of (A) lamella taken from an inner FGR (Figure 2.7 B, C) showing many prominent hollow carbon nanoglobules (some are indicated by arrows) and (B) a hollow carbon nanoglobule from altered (~CM2.7), metal-poor ICM (Figure 2.13).

We have also observed organic nanoglobules, carbon-rich grains that are <1 μm in size, in all but one of the sections (the most altered section of Paris, Figure 2.9), and we note that globules are more abundant in the material extracted from the inner layer of an FGR (Figure 3.12). Most globules are hollow with a central void or are compound globules with multiple voids, although small solid globules were also observed (it's possible that the presence of solid globules without voids is a FIB sectioning effect). Lastly, an assemblage comprising of a <200 nm sized haxonite grain attached to an ~1 μm poorly crystalline, Mg-poor (<6 wt%) grain with a magnetite interior was identified by EDS and SAED in a section taken from an FGR (Figure 3.13).

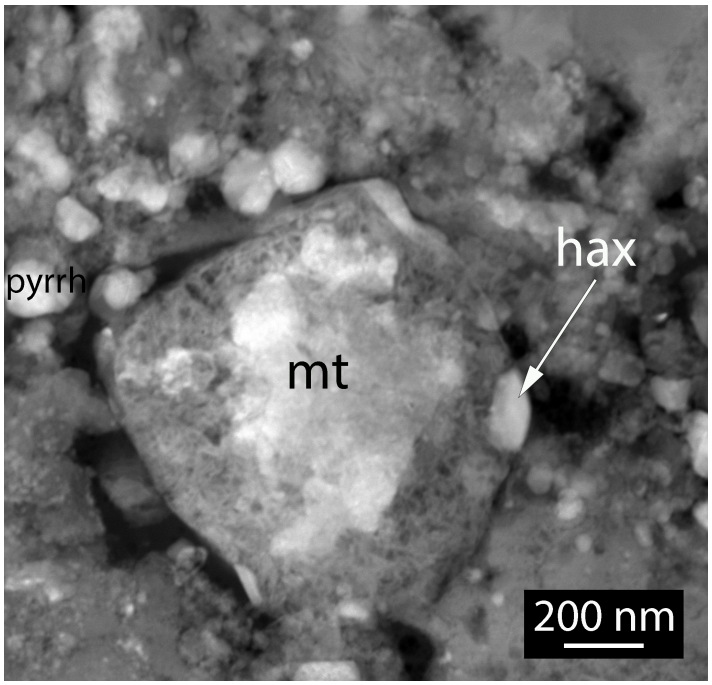

Figure 3.13: Dark-field TEM image of poorly crystalline grain with magnetite interior and attached Fe carbide (haxonite). FeS grain has composition consistent with pyrrhotite (pyrrh) as measured by EDS. Image taken from the FGR shown in Figure 2.12. mt = Magnetite; hax = haxonite

3.3.5 Amorphous silicate

While this study focuses on the nanoparticles embedded in GEMS and GEMS-like material, we refer the reader to the study by Ohtaki et al. (2021) which focuses on the amorphous silicate in which the nanoparticles are embedded. We summarize their study and findings here as the amorphous silicate component provides essential context for interpreting the origin of GEMS-like material. Using hyperspectral EDS mapping and electron energy loss spectroscopy (EELS) mapping, they found that the amorphous silicate in GEMS-like material differs significantly from GEMS in IDPs: (1) GEMS-like material is found as 100–1000 nm-sized irregularly shaped domains of amorphous silicate, while GEMS in IDPs consists of partially rounded objects 50–500 nm in diameter; (2) the amorphous silicate in GEMS-like material forms a continuous structure, while GEMS grains in IDPs are either distinct objects or aggregates; (3) the amorphous silicate in GEMS-like material has a significantly higher Fe content, ~25 at% on average, while IDP GEMS is nearly Fe-free; and (4) the oxidation state of Fe in Paris is dominated by Fe^{3+} from the amorphous silicate, while the oxidation state of Fe in IDP GEMS is dominated by Fe^{0} from metal inclusions (there is too little Fe in the amorphous silicate of IDP GEMS for EELS measurements).

3.4 Discussion

3.4.1 IDP GEMS vs. Paris GEMS-like material

As shown in Sections 4.1–4.3, there are notable differences between the nanoparticles in Paris and Aguas Zarcas GEMS-like material and those in IDP GEMS. Nanoparticles in GEMS-like material have larger sizes, pervasive O-rich rims, Ni-rich sulfides, and there is no metal within the amorphous silicate. Many of these observations can be explained by aqueous alteration of GEMS precursors. For example, the O-rich rims are plausibly made by oxidation (hydration) during aqueous activity. The smallest grains may have also been preferentially lost due to aqueous

alteration; however, aqueous alteration experiments of GEMS from IDPs showed that nm-sized sulfides and kamacite were less susceptible to alteration than amorphous silicates (Nakamura-Messenger et al., 2011). Metal inclusions of any size are either missing or significantly underrepresented within the amorphous silicate of Paris (more work needs to be done to determine if this is also true in Aguas Zarcas). It is unclear how the missing metal inclusions could have been lost due to aqueous alteration before crystallization of the surrounding amorphous silicate, and this may point to an intrinsic difference between the GEMS-like material in Paris and IDP GEMS. It is possible that the alteration conditions used in the experiments by Nakamura-Messenger et al. (2011) were not applicable to the conditions that were present on the Paris parent body, and so, further aqueous alteration experiments on GEMS are needed to explore the range of geochemical conditions that might produce the materials observed here.

Keller and Messenger (2011) argue that nanophase Fe-Ni grains found in GEMS served as condensation nuclei for the condensation of amorphous silicate in the solar nebula. The presolar GEMS model by Bradley (1994) instead argues that irradiation in the ISM produced the nanophase Fe-Ni grains. Experiments support the hypothesis that irradiation in the ISM can lead to the amorphization of crystalline silicates as well as the production of embedded Fe nanoparticles (e.g., Carrez et al., 2002). Experiments also support a third model posed by Davoisne et al. (2006), whereby embedded Fe nanoparticles are formed during thermal annealing of precursor, amorphous presolar silicates.[6] The absence of metal nanoparticles in the Paris amorphous silicate is puzzling if metal nanoparticles acted as condensation nuclei for amorphous silicates in the early

[6] In experiments by Davoisne et al. (2006), electron beam evaporation of San Carlos olivine is used to create a thin, amorphous silicate film which is then heated and annealed under vacuum at low and high oxygen fugacities (metal nanoparticles only formed under low fO_2). The oxygen fugacity of the solar nebula is lower than that used in experiments. See also Matsuno et al. (2014).

solar nebula as proposed and would also require a different formation pathway for sulfide formation. If the metal nanoparticles are instead the result of irradiation- or annealing-induced reduction of Fe, the lack of metal nanoparticles in Paris may signify that the amorphous silicate has not experienced the same irradiation or thermal history as the amorphous silicate in IDP GEMS. If metal was indeed originally present within the amorphous silicate but was lost due to aqueous alteration, it is also puzzling why the metal grains external to the amorphous silicate have survived. A possibility is that the nanophase metal grains within the original amorphous silicate may have had smaller sizes than other nanophase metal grains distributed throughout primitive matrices and were therefore more easily lost due to alteration. This would favor the hypothesis that the metal nanoparticles within GEMS formed by irradiation processing leading to smaller metal grains than those formed by other processes found throughout the matrix. It has also been suggested that the alteration of metal grains can be inhibited by the formation of an impermeable layer of $Fe(OH)_2$ when exposed to an alkaline (Chizmadia and Brearley, 2008), thus, differences in the fluid conditions experienced by the two populations of metal grains may explain the survival of metal grains outside of the amorphous silicate.

The origins of iron sulfide minerals in the Solar System are not well constrained and involve several possible primary (nebular) and secondary (parent body) processes. Equilibrium calculations show that troilite condenses in the solar nebula via gas-solid reactions between H_2S gas and Fe metal and that pyrrhotite formation is suppressed (Lauretta et al., 1996). Nanoscale analysis of experimental samples suggest that pyrrhotite formation is favored over troilite under certain nonequilibrium conditions (Gainsforth et al., 2017), which reflects the observation of primarily pyrrhotite rather than troilite in anhydrous IDPs (Zolensky and Thomas, 1995). Pentlandite is known to be an aqueous alteration product (e.g., Zolensky and Thomas, 1995), but experimental studies show that pentlandite can also form by sulfidation of metal in the solar nebula

(Lauretta et al., 1997, 1998). However, as pentlandite is not found in IDP GEMS or in anhydrous IDPs (Zolensky and Thomas, 1995; Dai and Bradley, 2001), it would be unexpected that pentlandite is indeed a primary nebular phase in these objects.

Studies have found that pentlandite is significantly more resistant to aqueous alteration than pyrrhotite and sometimes also forms from the hydration of pyrrhotite (Singerling, 2018). Therefore, aqueous alteration will tend to lead to a decrease in the abundance of pyrrhotite and an increase in the abundance of pentlandite. This trend is observed in Paris in that sections with a higher proportion of hydrated phases (e.g., cronstedtite and tochilinite) generally have a lower abundance of Ni-poor sulfides and a higher abundance of Ni-rich sulfides. We interpret that, while some coarse-grained pentlandite in primitive materials may be primary, the nanoscale ($\lesssim$100 nm) size fraction of pentlandite in GEMS-like material is a product of secondary alteration. The presence of pentlandite in GEMS-like material therefore does not itself rule out a genetic relationship with IDP GEMS.

Other nanosulfide phases identified in Paris that may reflect aqueous alteration are monoclinic pyrrhotite, tochilinite, and the sulfides of intermediate composition. Monoclinic pyrrhotite has been synthesized by annealing of hexagonal pyrrhotite <250 °C (Sugaki and Shima, 1965; Yund and Hall, 1969; O'Reilly et al., 2000) and by low-temperature aqueous activity (Sugaki and Shima, 1965). Experiments have found that chondritic tochilinite likely formed from the alteration of Fe-Ni metal beads in a S-bearing alkaline environment at low temperature (120–160 °C; Vacher et al., 2019). The finding of nanophase tochilinite in Paris therefore suggests that metal may indeed have been initially present within the amorphous silicate but was altered due to aqueous activity, although it is surprising that only one nanophase tochilinite particle was observed. Sulfides of intermediate composition between pyrrhotite and pentlandite have also been observed in hydrated IDPs and coarse-grained sulfides in CM chondrites (e.g., Zolensky et al., 2002, 2006).

While hydrated IDPs show a smooth distribution between pyrrhotite and pentlandite compositions, the nanophase sulfides in Paris and Aguas Zarcas as well as coarse-grained sulfides from other CMs have fewer sulfides of intermediate composition (Figure 3.8; see also Zolensky et al., 2002, 2006). The difference in the distribution of intermediate compositions likely reflects that Paris and other CM chondrites sample material from only one parent body, while hydrated IDPs likely sample material from many parent-bodies. It is also likely that at least some of these intermediate compositions, like pentlandite, are the result of aqueous alteration of pyrrhotite.

IDPs are pulse-heated during atmospheric entry, which may have thermally modified the inclusions originally present in IDP GEMS. As stated in Section 3.1, Dai and Bradley (2001) reported a cubic low-Ni sulfide phase in anhydrous IDPs that was sometimes intergrown with pyrrhotite and transformed into hexagonal pyrrhotite under the electron beam of the TEM. This observation led Dai and Bradley (2001) to suggest that many hexagonal pyrrhotites in IDPs may be secondary thermal alteration products from atmospheric entry heating and also demonstrates that IDP sulfides may not preserve their initial crystal structures. Therefore, both asteroidal aqueous alteration as well as thermal alteration during atmospheric entry could be responsible for at least some of the differences seen between GEMS-like grains in Paris and IDP GEMS. We have not observed any cubic, low-Ni sulfide phases in Paris, but it is unknown how this sulfide phase would respond in an aqueous environment.

The amorphous silicate component in Paris has higher Fe contents than the amorphous silicate in GEMS-bearing IDPs: ~15–40 at% in Paris compared to ~0–10 at% in IDP GEMS (Ohtaki et al., 2021). Higher Fe content may occur due to aqueous activity if Fe is mobilized from previously present metal nanoparticles. However, if this were the case, we would expect a higher Fe content in ICM compared to FGRs in Paris, but they were found to be the same within uncertainty. Furthermore, the Fe contents of amorphous silicate in primitive CCs that have

experienced less aqueous activity than Paris, such as Acfer 094 or the CR3.0 chondrites QUE 99177 and MET 00426, have even higher Fe contents than Paris, with ~20–55 at% in Acfer 094 and ~>50 at% in QUE 99177 and MET 00426 (Acfer 094: Ohtaki et al., 2021; CR3.0s: Abreu and Brearley, 2010). Similarly, it has been suggested that high Fe contents in presolar silicates may be due to aqueous processing, yet Fe contents are higher in presolar silicates from the CR3 chondrites QUE 99177 and MET 00426 than in the CR2 chondrite GRV 021710 (Floss and Stadermann, 2009; Zhao et al., 2013). It is therefore unlikely that aqueous alteration contributes significantly to the Fe content discrepancies between GEMS-like material and IDP GEMS.

3.4.2 FGRs vs. ICM

The least-altered sections from our Paris samples were taken from the FGRs surrounding metal-rich chondrules. These sections displayed very fine-grained textures, abundant GEMS-like material, and had little to no hydrated phases. As discussed above, the sulfide nanoparticles in the FGR sections were also more Ni-poor than those from the ICM, as expected for lower degrees of aqueous alteration. The observation that the FGRs are more pristine than the ICM in Paris was also found using high-resolution SEM and phase mapping, quantitative EPMA, and density measurements (Zanetta et al., 2021). This observation also agrees with presolar grain abundances (Leitner et al., 2016, 2020; Haenecour et al., 2018): Unlike presolar SiC grains, presolar silicates are quite sensitive to aqueous alteration. Haenecour et al. (2018) found presolar SiC abundances to be the same, within error, in both FGR and ICM regardless of petrologic type, suggesting that FGRs and ICM accreted from the same nebular reservoir; presolar silicate abundances are instead much lower in the ICM of petrologic type 2 chondrites than type 3 chondrites (Leitner et al., 2016), reflecting the differences in aqueous alteration experienced on the parent bodies. Haenecour et al. (2018) also noted that presolar silicate abundances are generally the same in FGRs regardless of

petrologic type. Moreover, while presolar silicate abundances are higher in the ICM in petrologic type 3 chondrites, they are generally higher in the FGRs of petrologic type 2 chondrites. Haenecour et al. (2018) interpreted that the lower presolar silicate abundances in FGRs in type 3 chondrites compared to ICM must reflect pre-accretionary aqueous alteration (e.g., Ciesla et al., 2003), while the lower abundances in ICM of type 2 chondrites are due to post-accretionary parent-body alteration, which inefficiently affected the FGRs due to their compacted nature. This trend is also consistent with presolar grain abundances in the FGRs of CM chondrites of lower petrologic type than that of Paris (Leitner et al., 2020). As Paris is a petrologic type 2 chondrite, it would therefore be expected that the FGRs in Paris are more pristine than the ICM, which is consistent with what we observe. Aqueous alteration of the ICM material also likely occurred mostly on the Paris parent body, although pre-accretionary aqueous alteration was likely a factor in both ICM and FGRs.

3.4.3 Preservation of primitive components

3.4.3.1 Anhydrous crystalline silicates

Several objects observed in Paris provide strong evidence for the survival of primary nebular condensates, including the silicate whiskers/platelets and LIME silicates. As with GEMS, enstatite whiskers and platelets are also characteristic features of CP-IDPs (Bradley et al., 1983). They are believed to be primary, high-temperature vapor-phase condensates. Their crystallographic orientations are unique in IDPs compared to terrestrial samples: enstatite whiskers in CP-IDPs are elongated along the [100] crystallographic axis, while terrestrial enstatites are elongated along the [001] axis. Enstatite whiskers in IDPs also often have stacking faults in the (100) plane and axial screw dislocations indicative of vapor-phase growth. The enstatite whiskers described by Leroux et al. (2015) are elongated along the [100] axis and have stacking faults in the (100) plane. Enstatite platelets in IDPs are thin along either the [010] or [001] direction, unlike

terrestrial enstatites with tabular morphologies, and are composed of intergrowths of ortho- and clinoenstatite.

Forsterite whiskers are highly unusual and have been observed only extremely rarely in IDPs (Bradley and Brownlee, 1983; Messenger and Keller, 2004). Though their origins are less certain, forsterite whiskers have also been formed during high-temperature condensation experiments (Tsuchiyama, 1998). The LIME compositions seen in the forsterite whiskers as well as in the individual LIME olivine and pyroxene crystals also suggest direct condensation from a solar nebular gas (Klöck et al., 1989; Ebel et al., 2012). LIME silicates have not been previously reported in Paris, but have been identified in a number of extraterrestrial samples, including IDPs (Klöck et al., 1989; Nakamura-Messenger et al., 2010), cometary samples from the Stardust mission (Zolensky et al., 2006), amoeboid olivine aggregates (AOAs; Grossman and Steele, 1976; Aléon et al., 2002; Weisberg et al., 2004; Sugiura et al., 2009), CR chondrule olivine (Ichikawa and Ikeda, 1995), coarse-grained chondrule rim material in the CV3 chondrite Allende (Rubin, 1984), ICM from LL3 Semarkona and CM2 Murchison (Klöck et al., 1989), and FGR material from C2-ungrouped EET83226 (Klöck et al., 1989). The O isotopic composition of LIME silicates from IDPs ($\Delta^{17}O \approx -2‰$; Aléon et al., 2009) differs from those in AOAs and Wild 2 samples ($\Delta^{17}O \approx -20‰$; Fagan et al., 2004; Nakashima et al., 2012), implying that there may be multiple formation processes or environments for LIME silicates. The O-isotopic compositions of LIME silicates in primitive matrices have yet to be measured.

Despite the preservation of primary nebular condensates, there appears to be a surprisingly low abundance of preserved, presolar material in Paris. GEMS-bearing IDPs, specifically anhydrous IDPs and targeted dust stream collections from comets, preserve the highest abundances of presolar (circumstellar) silicates (Busemann et al., 2009; Floss and Haenecour, 2016). If the GEMS-like material in Paris is indeed surviving (though aqueously altered) *bona fide* GEMS

equivalent to IDP GEMS, then it would be expected that a high abundance of presolar silicates would also be found in Paris; however, preliminary NanoSIMS investigations find extremely low presolar silicate abundances in Paris (Mostefaoui, 2011; Verdier-Paoletti et al., 2019). This suggests that the amorphous silicate matrix in Paris is unrelated to cometary IDPs or would require a heterogenous distribution of presolar silicates in the solar nebula.

Crystalline silicates make up more than ~25% of presolar silicate grains, with the remainder including both amorphous silicates and composite grains (Floss and Haenecour, 2016). Amorphous silicates are more sensitive to alteration than crystalline silicates (Nakamura-Messenger et al., 2011). If cometary, GEMS-bearing material was incorporated into the Paris parent body, it would be unexpected that presolar silicates would be somehow preferentially destroyed, while the amorphous silicate from GEMS remains. Such a large discrepancy between the proportions of incorporated GEMS and presolar silicates would require a temporal and/or spatial separation of these two components from IDPs. If IDP GEMS grains are presolar (interstellar), it is particularly difficult to explain how they could be the progenitors of the amorphous silicate in Paris as the interstellar and circumstellar grains would have to be decoupled. If IDP GEMS formed in the solar nebula, the discrepancy could arise if there was a difference in the relative amounts of nebular and interstellar components delivered to the asteroid and comet formation regions.

3.4.3.2 Organics

Organic nanoglobules have been reported in IDPs, comet Wild 2 samples, and several primitive carbonaceous chondrites including Paris (see Alexander et al., 2017, and references therein). Organic nanoglobules have variable morphologies, sizes, functional group chemistries, and isotopic compositions, which may have been shaped by a variety of pre- and post-accretionary

processes, but a subset of nanoglobules have extreme enrichments in D/H and $^{15}N/^{14}N$ likely formed in extremely cold (~10 K) and radiation-rich environments such as the protosolar molecular cloud or the outer regions of the solar nebula (Charnley and Rodgers, 2008; Alexander et al., 2017). Irradiation of molecular cloud ices has also been proposed as a mechanism for producing globular organics, in particular those with hollow interiors (Nakamura-Messenger et al., 2006; Ishii et al., 2018). Without knowing the isotopic composition or functional chemistry of the nanoglobules in Paris, it cannot be concluded that the nanoglobules imply an association between Paris and outer Solar System or primordial molecular cloud material. However, infrared spectra of aromatic-rich fragments of Paris match ISM spectra and suggest that Paris has preserved some interstellar organic matter (Merouane et al., 2012). Isotopic evidence from H isotopes in Paris matrices and O isotopes in Paris carbonates supports the incorporation of outer Solar System ice (Vacher et al., 2016, 2017; Piani et al., 2018). These observations, as well as the combined presence of organic nanoglobules, enstatite whiskers, LIME silicates, and GEMS-like material, are consistent with a possible relationship between Paris and CP-IDPs, which would suggest that IDP-like GEMS grains are the progenitors of the Paris GEMS-like material and any differences between them are due to secondary processing. While amorphous silicates (e.g., Acfer 094: Greshake, 1997; MET 00426 and QUE 99177: Abreu and Brearley, 2010; ALH 77307: Brearley, 1993) as well as organic nanoglobules (De Gregorio et al., 2013) have been found in the matrices of other primitive chondrites, none have been reported to contain this unique assemblage of primitive materials.

Coarse-grained carbide-magnetite assemblages (CMAs) have been described in unequilibrated, type-3 ordinary chondrites (e.g., Krot et al., 1997). CMAs in ordinary chondrites consist of the carbides haxonite and cohenite as well as kamacite, troilite, taenite, and pentlandite. Nanocrystalline carbides with magnetite rims have also been described in both ordinary chondrites (Keller, 1998) and carbonaceous chondrites (Abreu and Brearley, 2010). Neither the CMAs nor

the nanocrystalline carbides with rims have the same morphology as the assemblage seen here. The mechanism and timing of the formation of CMAs or nanocrystalline carbides with magnetite rims is not well constrained; although it is generally agreed that the carburization process that formed the Fe-carbides likely preceded the oxidation process that formed the magnetite. Both nebular and asteroidal formation for the Fe-carbides has been proposed (Krot et al., 1997; Keller, 1998).

3.5 Conclusions

We have explored the chemistry and mineralogy of the nanophase particles present throughout the fine-grained amorphous silicate in Paris and Aguas Zarcas. Using nanodiffraction, we have not identified any metal inclusions embedded in the amorphous silicate matrix, but we have identified rare metal grains that reside outside of the amorphous silicate domains. In addition to the absence of metal grains, the GEMS-like material differs in morphology, composition, and mineralogy to GEMS from IDPs believed to derive from comets. At this time, it is unclear if these differences are due to alteration or if they require independent origins. The presence of other phases commonly identified in IDPs, such as enstatite whiskers and platelets, LIME silicates, and carbon nanoglobules as well as isotopic measurements by other authors may support a genetic relationship between the GEMS-like material of Paris and those in IDPs, but these phases are more likely indicative of radial mixing in the solar nebula as the relatively large nanoparticle sizes, lack of metal nanoparticles, and high Fe contents in the amorphous silicate are not easily explained by aqueous alteration.

Chapter 4

Isotopic Analyses Facilitated by FIB Isolation Techniques

4.1 Development of FIB isolation techniques for CHILI measurements

The smallest structures resolvable by both NanoSIMS and CHILI are larger than the average sizes of presolar silicates and GEMS and lead to isotopic dilution of the measurements with surrounding material. FIB milling has been used previously to isolate presolar silicates from surrounding material for NanoSIMS analysis and involves depositing a protective cap of Pt and then ion milling an annulus around the grain of interest. I used this method to analyze the Fe and Ni isotopic compositions of two presolar silicates in CHILI but found that material outside of the milled region was still also sampled during analysis, leading to isotopic dilution of the measurements. For this reason, I developed a method to fully isolate sub-μm grains to avoid isotopic dilution, in which the FIB isolated grain is lifted out completely and placed onto a flat surface. During a preliminary test, I was able to measure the Fe and Ni isotopic composition of a grain lifted out from the matrix of Acfer 094 using this method.

4.2 Iron and Ni isotopic composition of isolated presolar silicates with CHILI

Presolar (circumstellar) silicates, GEMS, and primitive matrix grains may represent related and consecutive stages in the lifetime of cosmic silicates. In order to understand the relationships between these different primitive materials, isotopic studies are needed with increased spatial resolution and sensitivity, such as with the unparalleled analytical capabilities afforded by CHILI. Of particular interest are Fe and Ni isotopic composition of presolar silicates. Iron is highly abundant in presolar silicates, reaching as high as 40 at% in some samples (e.g., Ong and Floss,

2015). The high abundance of Fe makes it analytically favorable for analysis but is also a puzzle of its own: spectral observations of silicates around various stellar sources and in the ISM as well as thermodynamic calculations of silicate condensation predict Mg-rich/Fe-poor compositions. While secondary alteration may seem like an obvious explanation for this discrepancy, many presolar silicates with high Fe abundances show little evidence for secondary alteration.

Iron and Ni isotopic measurements can also help refine nucleosynthesis or galactic chemical evolution (GCE) models. The parent stars influence the neutron-rich nuclides but have little effect on the neutron-poor nuclides, which can then serve as proxies for GCE ($^{54}Fe/^{56}Fe$; $^{60}Ni/^{58}Ni$). This has been studied in presolar SiC grains (Trappitsch et al., 2018). In neutron-rich Fe isotopes, the largest compositional changes take place during the asymptotic giant branch (AGB) phase, where the $^{57}Fe/^{56}Fe$ ratios can become elevated by as much as 700‰ by the late dredge-up episodes. Silicates are predicted to form in earlier episodes before large $^{57}Fe/^{56}Fe$ excesses develop. Precise measurements of presolar silicates should probe this earlier stage of AGB evolution. While stellar models predict small to large excesses in $^{57}Fe/^{56}Fe$, many presolar silicates and presolar SiC grains show large depletions in this ratio (Nguyen and Messenger, 2014; Ong and Floss, 2015). Iron-58 has never been measured in presolar silicates due to the isobaric interference from ^{58}Ni, but presolar SiC can have significant $^{58}Fe/^{56}Fe$ enrichments of up to 500‰ (Trappitsch et al., 2018).

As described previously in Section 2.2.3, CHILI is a resonance ionization mass spectrometer designed to achieve an unprecedented lateral resolution of 10 nm and a useful yield of 30–40% (Stephan et al., 2016). Because of its high spatial resolution, improved sensitivity, and ability to eliminate isobaric interferences, CHILI is far better equipped than current SIMS instruments to resolve the true isotopic composition of nm-sized grains. The anticipated ~10 nm lateral resolution will be achieved using a Ga ion gun that is currently still in development. The

isotopic composition of presolar SiC grains have instead been successfully analyzed by applying a Nd:YLF desorption laser beam, frequency tripled to 351 nm, focused to ~1 μm (Stephan et al., 2016). However, presolar SiC grains are much larger than presolar silicates, GEMS, and meteorite matrix silicates and can also be extracted from their host meteorite using chemical treatments. The desorption laser's large beam size compared to the size of presolar silicates would lead to significant overlap of surrounding material. To avoid this issue, I have developed a method to isolate sub-μm grains for study with the desorption laser.

Ten presolar silicates were previously identified using NanoSIMS by O isotopic imaging of grain size separates from Acfer 094 dispersed onto Au foil. The elemental compositions of the presolar silicates were also characterized by Auger Nanoprobe. Using a TESCAN LYRA3 FIB-SEM equipped with an OmniGIS II gas injector, we isolated two of the presolar silicates using FIB milling. FIB milling has been used previously to isolate presolar silicates for NanoSIMS analysis (Nguyen and Messenger, 2014; Kodolányi et al., 2014). First, a cap of Pt is electron deposited over the grain to protect it from further milling and redeposition. Second, an annulus with an outer diameter of ~4 μm around the grain is milled away using the Ga^+ ion beam, leaving a central spoke (Figure 4.1). The Fe and Ni isotopic compositions were then measured in the two isolated presolar silicates using CHILI.

Our analyses of Acfer 094 matrix material as well as silicate standards (meteoritic olivine and pyroxene) show that these materials can be efficiently desorbed with the desorption laser. The laser power needed to desorb Fe and Ni from Pt and Au was found to be higher than the power needed to desorb from silicates. Thus, to avoid possible contamination from the Pt and Au, we

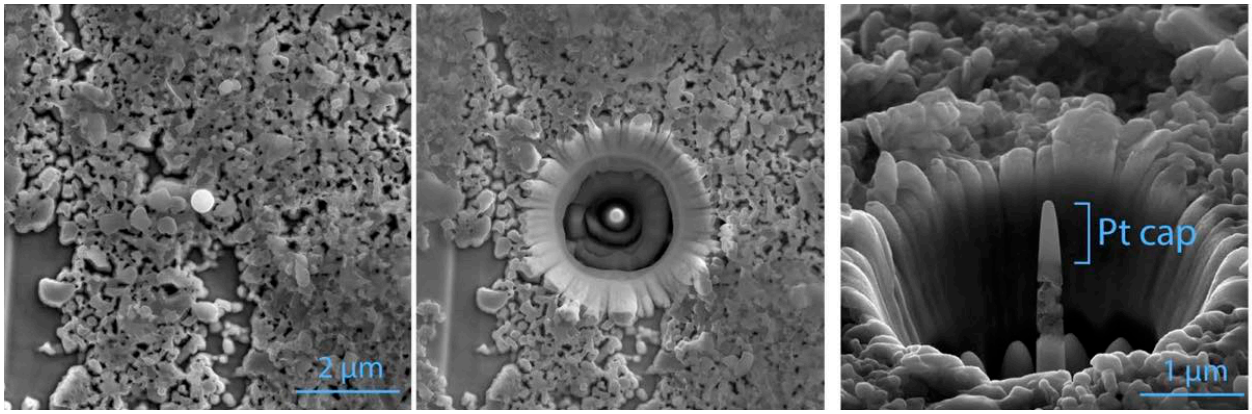

Figure 4.1: SEM images of grain isolation. (Left) untilted and (middle) tilted views of Pt deposit over grain. (Right) tilted view of FIB-isolated matrix grain.

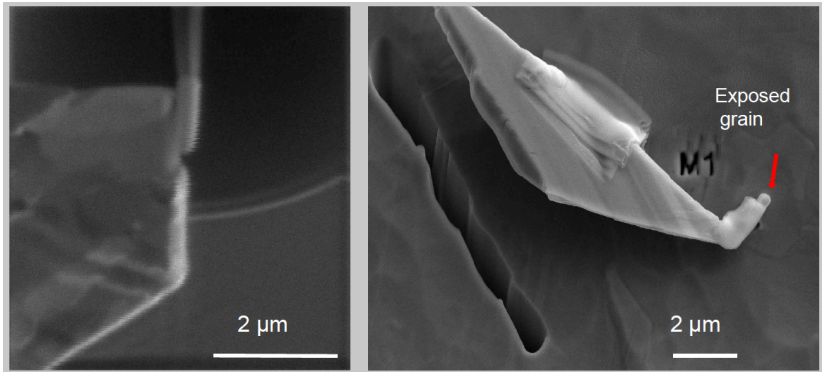

Figure 4.2: (Left) FIB image of tungsten needle prior to attachment to Pt cap. (Right) SEM image of lifted out and detached grain.

maintained the laser power below that needed for Pt or Au desorption. Nevertheless, subsequent electron imaging showed that material outside of the milled region was also desorbed. During analysis, it also appeared the spoke holding the grain was immediately lost while still Fe and Ni were detected, showing again that material from outside the region was being sampled.

For the remaining presolar silicates, we developed a method for fully lifting out and sequestering the grains from the surrounding material (Figure 4.2). After FIB milling around the grains, a tungsten needle is attached to the Pt cap with another layer of Pt via ion deposition using an Oxford OmniProbe 400 micromanipulator. An area of the Au foil is "cleaned" by ion milling.

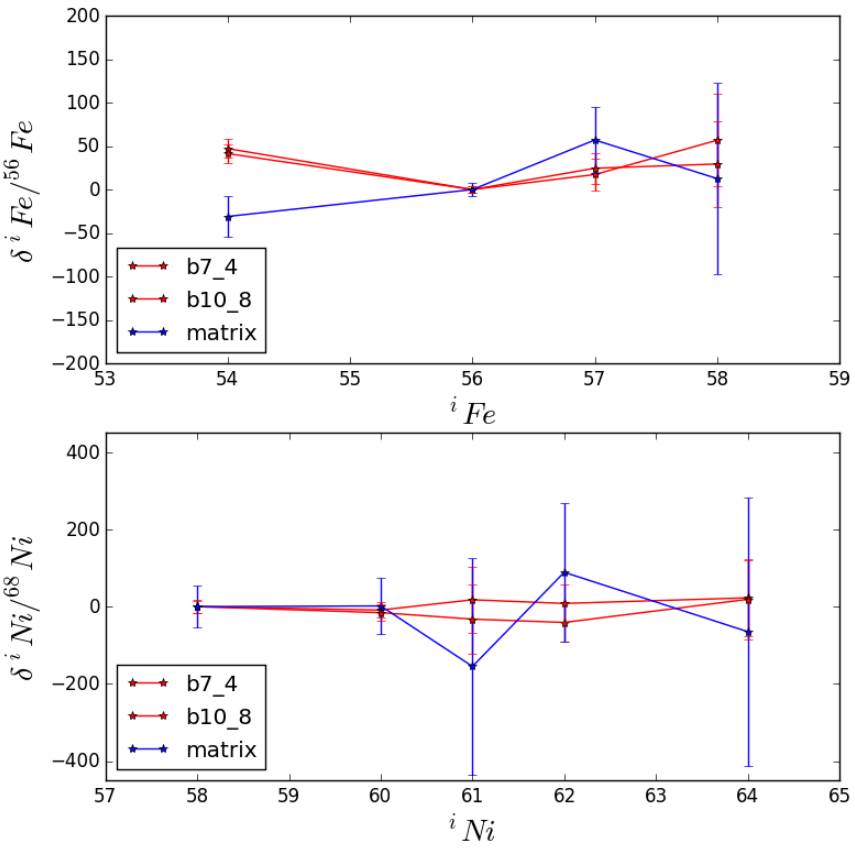

Figure 4.3: Fe and Ni isotopic composition in presolar silicates (red) and lifted out matrix grain (blue), normalized to meteoritic pyroxene measured in Ornans. 2σ error bars.

The needle with exposed grain is then affixed to the surface with another Pt deposit to avoid loss of the sample. One matrix grain has been successfully lifted out and analyzed with CHILI. The Fe and Ni isotopic compositions of this grain as well as the two (failed) presolar silicates are shown in Figure 4.3. While the presolar grains appear distinct in ^{54}Fe, more measurements are needed to assess if this is a true result or due to some systematic errors. The other isotopes are solar within uncertainties. Due to aforementioned reasons, it is likely that the presolar grains actually reflect separate matrix measurements.

4.3 Trace element isotopic measurements of matrix Acfer 094 grains using CHILI

I conducted the first isotopic study of heavy trace elements in primitive matrix, specifically in individual primitive matrix grains from Acfer 094. As described in the previous section, a desorption laser was used to remove sample material prior to the installation of the Ga^+ ion gun. With a spot size of ~1 μm, analyses of the primarily submicron matrix would have been considered bulk measurements. However, no measurable Sr, Mo, or Ba were found in the matrix in preliminary measurements. EDS mapping of the sample was later used to locate phases more likely to host these elements, specifically Ca-, Al-, K-, and Cr-rich phases (e.g., Figure 4.4). These phases were subsequently confirmed to be carriers of Sr, Mo, and Ba while the surrounding phases contributed no signal. Thus, despite the large beam size of the desorption laser, these can be considered single grain analyses. Future work is needed to constrain the concentration of trace heavy elements in the matrix as well as characterize the different host phases.

A total of fourteen matrix grains were analyzed with CHILI (Figure 4.5). These are the first measurements of heavy trace element isotopes in primitive silicate matrix. No resolved anomalous silicates were found at our level of precision. Large uncertainties were found due to the small grain sizes paired with the low abundance of trace elements in silicates; however, the uncertainties of many grains are small enough that an isotopically anomalous grain would be resolvable at the magnitudes typical of presolar SiC grains. For example, the largest uncertainty in δ^{92}Mo at 3σ is ~295 ‰ for these grains. With presolar SiC grains having anomalies in δ^{92}Mo of <−700 ‰, this would be clearly resolvable. Anomalies may be resolvable even in isotopes that are very low in abundance. For example, the lowest uncertainty at 3σ in δ^{84}Sr is ~371 ‰, showing that isotopic anomalies would be clearly resolvable at the magnitude of typical anomalous SiC grains for this same isotope (Figure 4.6). Therefore, despite the small grain sizes and low abundance

of trace elements in silicates, future isotopic measurements of trace elements in *bona fide* presolar silicates may be resolvable and will help constrain the formation history and environment of these grains.

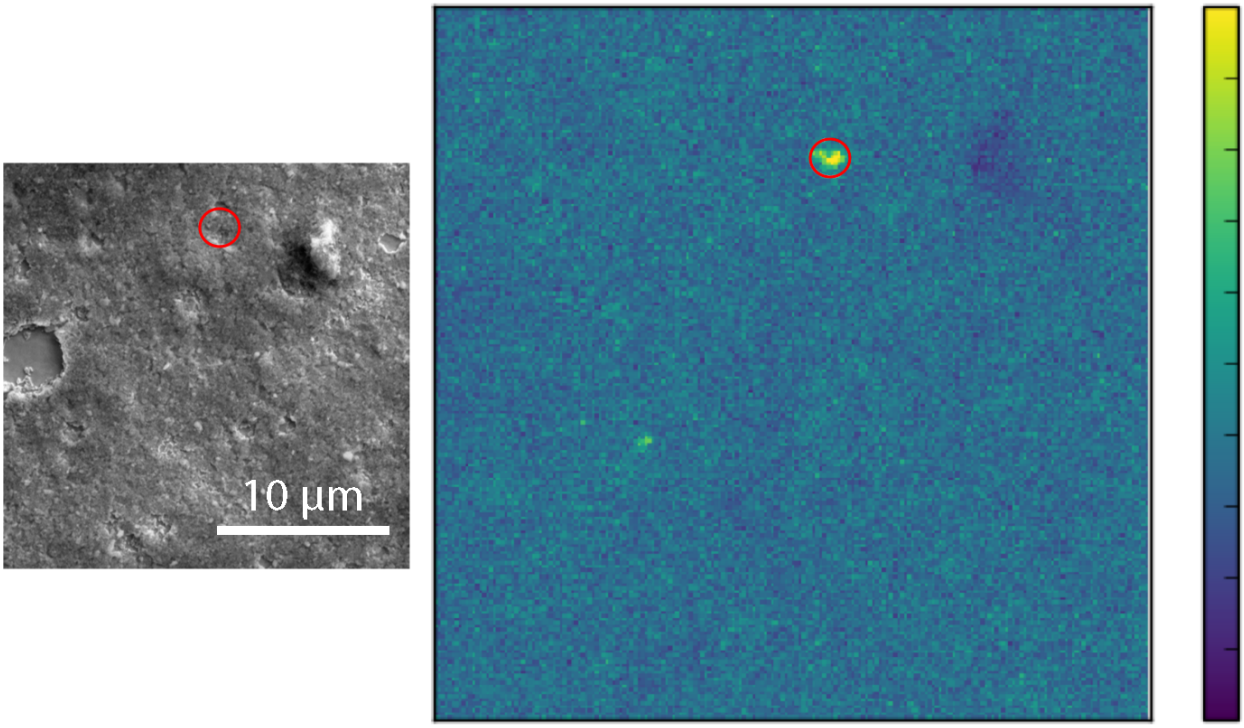

Figure 4.4: EDS image and corresponding EDS heat map showing grain with elevated K contents.

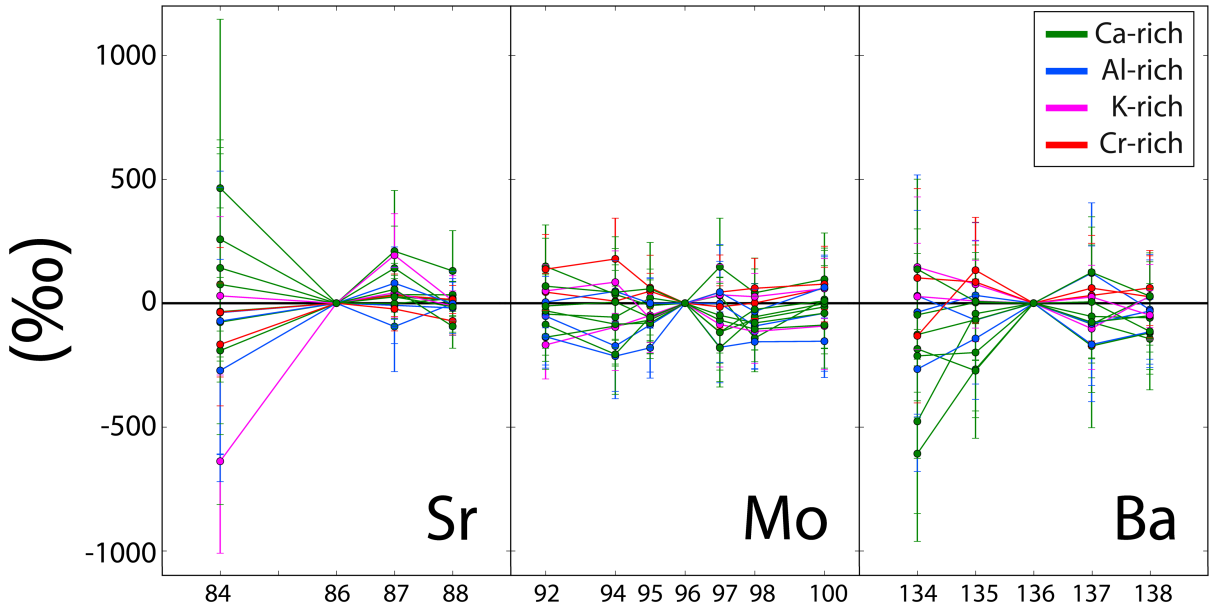

Figure 4.5: Isotope patterns for Sr, Mo, and Ba measured in 14 Acfer 094 matrix grains using CHILI. Uncertainties are 2σ. ^{130}Ba and ^{132}Ba not shown as too low in abundance.

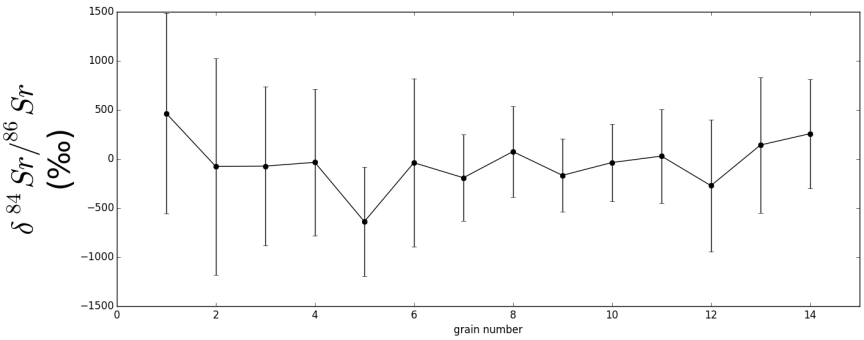

Figure 4.6: Isotope measurements in ^{84}Sr measured for all fourteen grains. Uncertainties are 3σ.

4.4 FIB-lamellae preparations for NanoSIMS isotopic studies

In collaboration with Nicole Nie, I prepared FIB lift-out sections of Hawaiian hematite spherules for a NanoSIMS study of their Fe isotopic compositions and Mn/Fe ratios to be used as an analogue for understanding Martian hematite spherule formation. This study found that the isotopic and elemental compositions of the Hawaiian hematite spherules is consistent with direct

precipitation from an acid-sulfate fluid and 80% Fe oxidation (Nie et al., 2020). This study also shows the viability of this method for studying future sample returns from Mars.

In collaboration with Nigel Brauser, these methods were also used for the preparation of similar lift-out sections of diamond anvil cell specimens. These specimens will be used to experimentally determine the self-diffusivity of Fe at high pressures in order to constrain the viscosity of the Earth's solid, inner core.

Chapter 5

Summary and Outlook

The pre-accretionary histories of many meteorites have been lost or modified due to secondary processing on the parent body, such as thermal metamorphism and aqueous alteration. The matrices of primitive CCs, i.e., those CCs that have experienced minimal to no secondary processing, are comprised of unequilibrated assemblages of fine-grained materials that retain preserved primordial components. Primitive CC matrices are therefore vital to understanding the inventory of available solids and their histories in the early solar nebula.

A major component of primitive CC matrices is amorphous silicate (e.g., Leroux et al., 2015). Amorphous silicate is highly susceptible to alteration and its presence is therefore indicative of minimal secondary processing. Amorphous silicate is also the predominant component of the ISM as well as CP-IDPs that are believed to originate in comets and are considered to be the most pristine extraterrestrial samples to date. The amorphous silicate in CP-IDPs contains inclusions of metal and sulfides and are referred to as GEMS. Despite their high abundance in CP-IDPs, GEMS has yet to be unambiguously identified in meteorites, and their relationship to the amorphous silicates observed in primitive CCs are unconstrained.

GEMS-like objects have been described in rare primitive CCs, including Paris (CM2.7–2.9), and Acfer 094 (C-ungrouped), a C-rich clast from LaPaz Icefield 02342 (CR2) (Chizmadia and Brearley, 2008; Leroux et al., 2015; Nittler et al., 2019; Matsumoto et al., 2019), and now Aguas Zarcas; however, as discussed in Chapter 3, there are notable differences between the GEMS-like objects and *bona fide* IDP GEMS. GEMS-like material has:

(1) larger inclusion sizes;

(2) pervasive O-rich rims surrounding inclusions;

(3) pyrrhotite and pentlandite nanosulfides, whereas GEMS in IDPs are exclusively pyrrhotite;

(4) an absence of metal inclusions within the amorphous silicate; and

(5) a higher Fe content and Fe oxidation state.

It remains unclear if these differences are inherent or due to modification of GEMS in the parent body. Until only recently, all CMs were classified as petrologic type 2 chondrites, indicating at least some level of aqueous alteration, even if minimal as in the case of Paris 2.9 lithologies. A recent study by Kimura et al. (2020) has identified the first CM type 3 chondrite, Asuka 12169, and Nittler et al. (2021) have also found that this meteorite contains the highest presolar O-rich abundance of any meteorite (identical to that of the CO3.0 chondrite Dominion Range 08006). If there is GEMS-like material preserved in Asuka 12169, it should have preserved the chemistry and mineralogy of this material prior to aqueous alteration. Generally, studying amorphous silicates and GEMS-like material in other primitive CCs of varying levels of alteration, and CCs from different CC groups are needed to clarify the origins and interrelationships between these materials.

Characterizations of fine-grained materials such as presolar silicates, GEMS, and fine-grained chondrite matrices have been hindered due to analytical limitations. Advanced techniques in sample preparation in combination with new instrumentation for sample analysis can provide new or improved data on small-scale samples. For example, to date, no presolar silicates or GEMS have been analyzed for heavy trace elements such as Mo, Zr, Ba, or Sr. Previous RIMS work has been done on heavy trace elements in SiC grains, but O-rich grains such as silicates would probe earlier (in the case of AGBs) or different (in the case of SNII) domains of stellar evolution than carbides. The *s*-process, *r*-process, *p*-process, and neutron burst signatures of such elements should be diagnostic of stellar origins and would provide important constraints on their associated

nucleosynthetic processes. Molybdenum, for example, would be a favorable element to study as it has two p-only isotopes (^{92}Mo and ^{94}Mo), one *s*-only isotope (^{96}Mo), one *r*-only isotope (^{100}Mo), and three isotopes with contributions from both the *r*- and *s*-process (^{95}Mo, ^{97}Mo, and ^{98}Mo).

GEMS may also store a memory of extinct short-lived radionuclides (SLRs) through their decay products, such as ^{60}Fe, ^{26}Al, and ^{44}Ti. Nickel-60 excesses due to the decay of ^{60}Fe have yet to be detected in presolar grains as a very high Fe/Ni ratio is required. The enhanced Fe contents in presolar silicates and GEMS coupled with the greater analytical sophistication of CHILI may make this detection more feasible (Davis and Gallino, 2006). Similarly, ^{26}Mg excesses due to extinct ^{26}Al or ^{44}Ca excesses due to extinct ^{44}Ti, as is seen in type X SiC grains (Besmehn and Hoppe, 2003), may also be detectable. Titanium-44, a SLR that decays to ^{44}Ca with a half-life of 60 days, is only synthesized in supernovae. If GEMS formed in a supernova environment, excesses in ^{44}Ca would provide strong evidence for this.

Fine-grained extraterrestrial materials may be small in size, but they nevertheless contain sizeable amounts of information. Complimentary chemical, mineralogical, and isotopic studies of presolar silicates, GEMS, and chondrite matrices with greater analytical sophistication will provide new and meaningful insights into our Solar System and the galaxy that contains it. As we push the limits of instrumentation, we push the limits of scientific discovery and approach a complete understanding of the universe.

BIBLIOGRAPHY

Abreu N. M. and Brearley A. J. (2010) Early solar system processes recorded in the matrices of two highly pristine CR3 carbonaceous chondrites, MET 00426 and QUE 99177. *Geochim. Cosmochim. Acta* **74**, 1146–1171.

Aléon J., Engrand C., Leshin L. A. and McKeegan K. D. (2009) Oxygen isotopic composition of chondritic interplanetary dust particles: a genetic link between carbonaceous chondrites and comets. *Geochim. Cosmochim. Acta* **73**, 4558–4575.

Aléon J., Krot A. N. and McKeegan K. D. (2002) Calcium-aluminum-rich inclusions and amoeboid olivine aggregates from the CR carbonaceous chondrites. *Meteorit. Planet. Sci.* **37**, 1729–1755.

Alexander C. M. O'D, Cody G. D., De Gregorio B. T., Nittler L. R. and Stroud R. M. (2017) The nature, origin and modification of insoluble organic matter in chondrites, the major source of Earth's C and N. *Chem. Erde-Geochem.* **77**, 227–256.

Altobelli N., Postberg F., Fiege K., Trieloff M., Kimura H., Sterken V. J., Hsu H.-W., Hillier J., Khawaja N., Moragas-Klostermeyer G., Blum J., Burton M., Srama R., Kempf S. and Gruen E. (2016) Flux and composition of interstellar dust at Saturn from Cassini's Cosmic Dust Analyzer. *Science* **352**, 312–318.

Besmehn A. and Hoppe P. (2003) A NanoSIMS study of Si- and Ca-Ti-isotopic compositions of presolar silicon carbide grains from supernovae. *Geochim. Cosmochim. Acta* **67**, 4693–4703.

Bourot-Denise M., Zanda B., Marrocchi Y., Greenwood R. C., Pont S., Hewins R. H., Franchi I. A. and Cornen G. (2010) Paris: the slightly altered, slightly metamorphosed CM that bridges the gap between CMs and COs. *Lunar Planet. Sci.* **41**, #1683.

Bradley J. P. (1994) Chemically anomalous, preaccretionally irradiated grains in interplanetary dust from comets. *Science* **265**, 925–929.

Bradley J. P. (2014) Early solar nebula grains - interplanetary dust particles. In *Meteorites and Cosmochemical Processes* (Ed. A. M. Davis), Vol. 1 *Treatise on Geochemistry, 2nd Ed.* (Exec. Eds. H. D. Holland and K. K. Turekian), Elsevier, Oxford, pp. 287–308.

Bradley J. P. and Brownlee D. E. (1983) Mineralogy and crystal chemistry of CP micrometeorites. *Lunar Planet. Sci.* **14**, 67-68.

Bradley J. P., Brownlee D. E. and Veblen D. R. (1983) Pyroxene whiskers and platelets in interplanetary dust: evidence of vapour phase growth. *Nature* **301**, 473–477.

Bradley J. P. and Dai Z. R. (2004) Mechanism of formation of glass with embedded metal and sulfides. *Astrophys. J.* **617**, 650–655.

Brearley A. J. (1993) Matrix and fine-grained rims in the unequilibrated CO3 chondrite, ALHA77307: Origins and evidence for diverse, primitive nebular dust components. *Geochim. Cosmochim. Acta* **57**, 1521–1550.

Busemann H., Nguyen A. N., Cody G. D., Hoppe P., Kilcoyne A. L. D., Stroud R. M., Zega T. J. and Nittler L. R. (2009) Ultra-primitive interplanetary dust particles from the comet 26P/Grigg–Skjellerup dust stream collection. *Earth Planet. Sci. Lett.* **288**, 44–57.

Carrez P., Demyk K., Cordier P., Gengembre L., Grimblot J., D'hendecourt L., Jones A. P. and Leroux H. (2002) Low-energy helium ion irradiation-induced amorphization and chemical changes in olivine: Insights for silicate dust evolution in the interstellar medium. *Meteorit. Planet. Sci.* **37**, 1599–1614.

Charnley S. B. and Rodgers S. D. (2008) Interstellar reservoirs of cometary matter. *Space Sci. Rev.* **138**, 59–73.

Chizmadia L. J. and Brearley A. J. (2008) Mineralogy, aqueous alteration, and primitive textural characteristics of fine-grained rims in the Y-791198 CM2 carbonaceous chondrite: tem observations and comparison to ALHA81002. *Geochim. Cosmochim. Acta* **72**, 602–625.

Ciesla F. J., Lauretta D. S., Cohen B. A. and Hood L. L. (2003) A nebular origin for chondritic fine-grained phyllosilicates. *Science* **299**, 549–552.

Cowley J. M. (1999) Electron nanodiffraction. *Microsc. Res. Techniq.* **46**, 75–97.

Dai Z. R. and Bradley J. P. (2001) Iron-nickel sulfides in anhydrous interplanetary dust particles. *Geochim. Cosmochim. Acta* **65**, 3601–3612.

Davis A. M. and Gallino R. (2006) Short-lived radionuclides in presolar SiC grains: constraints on timescales in AGB stars. *Memorie della Societa Astronomica Italiana* **77**, 885.

Davoisne C., Djouadi Z., Leroux H., d'Hendecourt L., Jones A. and Deboffle D. (2006) The origin of GEMS in IDPs as deduced from microstructural evolution of amorphous silicates with annealing. *Astron. Astrophys.* **448**, L1–L4.

De Gregorio B. T., Stroud R. M., Nittler L. R., Alexander C. M. O'D, Bassim N. D., Cody G. D., Kilcoyne A. L. D., Sandford S. A., Milam S. N., Nuevo M. and Zega T. J. (2013) Isotopic and chemical variation of organic nanoglobules in primitive meteorites. *Meteorit. Planet. Sci.* **48**, 904–928.

Dobrică E., Engrand C., Leroux H., Rouzaud J.-N. and Duprat J. (2012) Transmission electron microscopy of CONCORDIA ultracarbonaceous antarctic micrometeorites (UCAMMs): mineralogical properties. *Geochim. Cosmochim. Acta* **76**, 68–82.

Draine B. T. (2009) Interstellar dust models and evolutionary implications. In *Cosmic Dust - Near and Far* (eds. T. Henning, E. Grün, and J. Steinacker). Astronomical Society of the Pacific Conference Series. pp. 453–473.

Draine B. T., Dale D. A., Bendo G., Gordon K. D., Smith J. D. T., Armus L., Engelbracht C. W., Helou G., R. C. Kennicutt J., Li A., Roussel H., Walter F., Calzetti D., Moustakas J., Murphy E. J., Rieke G. H., Bot C., Hollenbach D. J., Sheth K. and Teplitz H. I. (2007) Dust Masses, PAH Abundances, and Starlight Intensities in the SINGS Galaxy Sample. *Astrophys. J.* **663**, 866.

Ebel D. S., Weisberg M. K. and Beckett J. R. (2012) Thermochemical stability of low-iron, manganese-enriched olivine in astrophysical environments. *Meteorit. Planet. Sci.* **47**, 585–593.

Fagan T. J., Krot A. N., Keil K. and Yurimoto H. (2004) Oxygen isotopic evolution of amoeboid olivine aggregates in the reduced CV3 chondrites Efremovka, Vigarano, and Leoville. *Geochim. Cosmochim. Acta* **68**, 2591–2611.

Ferrière K. M. (2001) The interstellar environment of our galaxy. *Rev. Mod. Phys.* **73**, 1031–1066.

Floss C. and Haenecour P. (2016) Presolar silicate grains: abundances, isotopic and elemental compositions, and the effects of secondary processing. *Geochem. J.* **50**, 3–25.

Floss C. and Stadermann F. (2009) Auger Nanoprobe analysis of presolar ferromagnesian silicate grains from primitive CR chondrites QUE 99177 and MET 00426. *Geochim. Cosmochim. Acta* **73**, 2415–2440.

Gabrielse G., Fei X., Orozco L., Tjoelker R., Haas J., Kalinowsky H., Trainor T. and Kells W. (1990) Thousandfold improvement in the measured antiproton mass. *Phys. Rev. Lett.* **65**, 1317–1320.

Gainsforth Z., Lauretta D. S., Tamura N., Westphal A. J., Jilly-Rehak C. E. and Butterworth A. L. (2017) Insights into solar nebula formation of pyrrhotite from nanoscale disequilibrium phases produced by H_2S sulfidation of Fe metal. *Am. Mineral.* **102**, 1881–1893.

Greshake A. (1997) The primitive matrix components of the unique carbonaceous chondrite Acfer 094: A TEM study. *Geochim. Cosmochim. Acta* **61**, 437–452.

Grossman L. and Steele I. M. (1976) Amoeboid olivine aggregates in the Allende meteorite. *Geochim. Cosmochim. Acta* **40**, 149–155.

Haenecour P., Floss C., Zega T. J., Croat T. K., Wang A., Jolliff B. L. and Carpenter P. (2018) Presolar silicates in the matrix and fine-grained rims around chondrules in primitive CO3.0 chondrites: evidence for pre-accretionary aqueous alteration of the rims in the solar nebula. *Geochim. Cosmochim. Acta* **221**, 379–405.

Hewins R. H., Bourot-Denise M., Zanda B., Leroux H., Barrat J.-A., Humayun M., Göpel C., Greenwood R. C., Franchi I. A., Pont S., Lorand J.-P., Cournède C., Gattacceca J., Rochette P., Kuga M., Marrocchi Y. and Marty B. (2014) The Paris meteorite, the least altered CM chondrite so far. *Geochim. Cosmochim. Acta* **124**, 190–222.

Hoppe P., Leitner J. and Kodolányi J. (2017) The stardust abundance in the local interstellar cloud at the birth of the Solar System. *Nat. Astron.* **1**, 617–620.

Ichikawa O. and Ikeda Y. (1995) Petrology of the Yamato-8449 CR chondrite. *Ant. Met. Res.* **8**, 63.

Ishii H. A., Bradley J. P., Bechtel H. A., Brownlee D. E., Bustillo K. C., Ciston J., Cuzzi J. N., Floss C. and Joswiak D. J. (2018) Multiple generations of grain aggregation in different environments preceded solar system body formation. *Proc. Natl. Acad. Sci.* **115**, 6608–6613.

Keller L. P. (1998) A transmission electron microscope study of iron-nickel carbides in the matrix of the Semarkona unequilibrated ordinary chondrite. *Meteorit. Planet. Sci.* **33**, 913–919.

Keller L. P. and Messenger S. (2011) On the origins of GEMS grains. *Geochim. Cosmochim. Acta* **75**, 5336–5365.

Kemper F., Vriend W. J. and Tielens A. G. G. M. (2004) The absence of crystalline silicates in the diffuse interstellar medium. *The Astrophys. J.* **609**, 826–837.

Kerraouch I., Bischoff A., Zolensky M. E., Pack A., Patzek M., Hanna R. D., Fries M. D., Harries D., Kebukawa Y., Le L., Ito M. and Rahman Z. (2021) The polymict carbonaceous breccia Aguas Zarcas: A potential analog to samples being returned by the OSIRIS-REx and Hayabusa2 missions. *Meteorit. Planet. Sci.*, in press, doi: 10.1111:maps.13620 (34 pp).

Kimura M., Imae N., Komatsu M., Barrat J. A., Greenwood R. C., Yamaguchi A. and Noguchi T. (2020) The most primitive CM chondrites, Asuka 12085, 12169, and 12236, of subtypes 3.0–2.8: Their characteristic features and classification. *Polar Science* **26**, #100565 (15 pp).

Klöck W., Thomas K. L., McKay D. S. and Palme H. (1989) Unusual olivine and pyroxene composition in interplanetary dust and unequilibrated ordinary chondrites. *Nature* **339**, 126–128.

Kodolányi J., Hoppe P., Gröner E., Pauly C. and Mücklich F. (2014) The Mg isotope composition of presolar silicate grains from red giant stars. *Geochim. Cosmochim. Acta* **140**, 577–605.

Krasnokutski S. A., Rouillé G., Jäger C., Huisken F., Zhukovska S. and Henning T. (2014) Formation of silicon oxide grains at low temperature. *Astrophys. J.* **782**, 15.

Krot A. N., Zolensky M. E., Wasson J. T., Scott E. R. D., Keil K. and Ohsumi K. (1997) Carbide-magnetite assemblages in type-3 ordinary chondrites. *Geochim. Cosmochim. Acta* **61**, 219–237.

Lauretta D. S., Kremser D. T. and Fegley B. Jr. (1996) The rate of iron sulfide formation in the solar nebula. *Icarus* **122**, 288–315.

Lauretta D. S., Lodders K. and Fegley B. Jr. (1997) Experimental simulations of sulfide formation in the solar nebula. *Science* **277**, 358–360.

Lauretta D. S., Lodders K. and Fegley B. Jr. (1998) Kamacite sulfurization in the solar nebula. *Meteorit. Planet. Sci.* **33**, 821–833.

Leitner J., Metzler K., Vollmer C., Floss C., Haenecour P., Kodolányi J., Harries D. and Hoppe P. (2020) The presolar grain inventory of fine-grained chondrule rims in the Mighei-type (CM) chondrites. *Meteorit. Planet. Sci.* **55**, 1176–1206.

Leitner J., Vollmer C., Floss C., Zipfel J. and Hoppe P. (2016) Ancient stardust in fine-grained chondrule dust rims from carbonaceous chondrites. *Earth Planet. Sci. Lett.* **434**, 117–128.

Leroux H., Cuvillier P., Zanda B. and Hewins R. H. (2015) GEMS-like material in the matrix of the Paris meteorite and the early stages of alteration of CM chondrites. *Geochim. Cosmochim. Acta* **170**, 247–265.

Longo D. M., Howe J. M. and Johnson W. C. (1999) Experimental method for determining Cliff–Lorimer factors in transmission electron microscopy (TEM) utilizing stepped wedge-shaped specimens prepared by focused ion beam (FIB) thinning. *Ultramicroscopy* **80**, 85–97.

Mann H. B. and Whitney D. R. (1947) On a test of whether one of two random variables is stochastically larger than the other. *Ann. Math. Stat.* **18**, 50–60.

Matsumoto M., Tsuchiyama A., Nakato A., Matsuno J., Miyake A., Kataoka A., Ito M., Tomioka N., Kodama Y., Uesugi K., Takeuchi A., Nakano T. and Vaccaro E. (2019) Discovery of fossil asteroidal ice in primitive meteorite Acfer 094. *Sci. Adv.* **5**, #eaax5078 (10 pp).

Matsuno J., Tsuchiyama A., Miyake A., Noguchi R. and Ichikawa S. (2014) Reduction experiment of FeO-bearing amorphous silicate: Application to origin of metallic iron in GEMS. *ApJ* **792**, 136.

Merouane S., Djouadi Z., d'Hendecourt L. L. S., Zanda B. and Borg J. (2012) Hydrocarbon materials of likely interstellar origin from the Paris meteorite. *Astrophys. J.* **756**, 154.

Messenger S. and Keller L. P. (2004) A supernova silicate from a cluster IDP. *Meteorit. Planet. Sci.* **39**, A68.

Meteoritical Bulletin Database. Available at: https://www.lpi.usra.edu/meteor/.

Metzler K. (2004) Formation of accretionary dust mantles in the solar nebula: evidence from preirradiated olivines in CM chondrites. *Meteorit. Planet. Sci.* **39**, 1307–1319.

Metzler K., Bischoff A. and Stöffler D. (1992) Accretionary dust mantles in CM chondrites: evidence for solar nebula processes. *Geochim. Cosmochim. Acta* **56**, 2873–2897.

Mostefaoui S. (2011) The search for presolar oxides in Paris. *Meteorit. Planet. Sci.* **46**, A169.

Nakamura-Messenger K., Clemett S. J., Messenger S. and Keller L. P. (2011) Experimental aqueous alteration of cometary dust. *Meteorit. Planet. Sci.* **46**, 843–856.

Nakamura-Messenger K., Keller L. P., Clemett S. J., Messenger S., Jones J. H., Palma R. L., Pepin R. O., Klöck W., Zolensky M. E. and Tatsuoka H. (2010) Brownleeite: a new manganese silicide mineral in an interplanetary dust particle. *Am. Mineral.* **95**, 221–228.

Nakamura-Messenger K., Messenger S., Keller L. P., Clemett S. J. and Zolensky M. E. (2006) Organic globules in the Tagish Lake meteorite: remnants of the protosolar disk. *Science* **314**, 1439–1442.

Nakashima D., Ushikubo T., Joswiak D. J., Brownlee D. E., Matrajt G., Weisberg M. K., Zolensky M. E. and Kita N. T. (2012) Oxygen isotopes in crystalline silicates of comet Wild 2: a comparison of oxygen isotope systematics between Wild 2 particles and chondritic materials. *Earth Planet. Sci. Lett.* **357–358**, 355–365.

Newton J., Bischoff A., Arden J. W., Franchi I. A., Geiger T., Greshake A. and Pillinger C. T. (1995) Acfer 094, a uniquely primitive carbonaceous chondrite from the Sahara. *Meteoritics* **30**, 47–56.

Nguyen A. N. and Messenger S. (2014) Resolving the stellar sources of isotopically rare presolar silicate grains through Mg and Fe isotopic analyses. *Astrophys. J.* **784**, #149 (15 pp).

Nie N. X., Dauphas N., Villalon K. L., Liu N., Heard A. W., Morris R. V. and Mertzman S. A. (2020) Iron isotopic and chemical tracing of basalt alteration and hematite spherule formation in Hawaii: A prospective study for Mars. *Earth Planet. Sci. Lett.* **544**, #116385 (14 pp).

Nittler L. R., Alexander C. M. O'D, Davidson J., Riebe M. E. I., Stroud R. M. and Wang J. (2018) High abundances of presolar grains and 15N-rich organic matter in CO3.0 chondrite Dominion Range 08006. *Geochim. Cosmochim. Acta* **226**, 107–131.

Nittler L. R., Alexander C. M. O'D, Patzer A. and Verdier-Paoletti M. J. (2021) Presolar stardust in highly pristine CM chondrites Asuka 12169 and Asuka 12236. *Meteorit. Planet. Sci.*, in press, doi: 10.1111:maps.13618 (17 pp).

Nittler L. R., Alexander C. M. O'D, Gao X., Walker R. M. and Zinner E. (1997) Stellar Sapphires: The Properties and Origins of Presolar Al_2O_3 in Meteorites. *The Astrophysical Journal* **483**, 475–495.

Nittler L. R., Stroud R. M., Trigo-Rodríguez J. M., Gregorio B. T. D., Alexander C. M. O'D, Davidson J., Moyano-Cambero C. E. and Tanbakouei S. (2019) A cometary building block in a primitive asteroidal meteorite. *Nat. Astron.* **3**, 659–666.

Noguchi T., Ohashi N., Tsujimoto S., Mitsunari T., Bradley J. P., Nakamura T., Toh S., Stephan T., Iwata N. and Imae N. (2015) Cometary dust in Antarctic ice and snow: Past and present chondritic porous micrometeorites preserved on the Earth's surface. *Earth Planet. Sci. Lett.* **410**, 1–11.

Ohnishi I. and Tomeoka K. (2007) Hydrothermal alteration experiments of enstatite: Implications for aqueous alteration of carbonaceous chondrites. *Meteorit. Planet. Sci.* **42**, 49–61.

Ohtaki K., Ishii H. A., Bradley J. P., Villalon K. L., Davis A. M., Stephan T., Bustillo K. C. and Ciston J. (2021) Search for meteoritic GEMS I: Comparison of amorphous silicates in Paris and Acfer 094 chondrite matrices and in anhydrous chondritic interplanetary dust particles. *Geochim. Cosmochim. Acta (submitted)*.

Ong W. J. and Floss C. (2015) Iron isotopic measurements in presolar silicate and oxide grains from the Acfer 094 ungrouped carbonaceous chondrite. *Meteorit. Planet. Sci.* **50**, 1392–1407.

O'Reilly W., Hoffmann V., Chouker A. C., Soffel H. C. and Menyeh A. (2000) Magnetic properties of synthetic analogues of pyrrhotite ore in the grain size range 1-24 μm. *Geophys. J. Int.* **142**, 669–683.

Piani L., Yurimoto H. and Remusat L. (2018) A dual origin for water in carbonaceous asteroids revealed by CM chondrites. *Nat. Astron.* **2**, 317–323.

Rouillé G., Jäger C., Krasnokutski S. A., Krebsz M. and Henning T. (2014) Cold condensation of dust in the ISM. *Faraday Discuss.* **168**, 449–460.

Rubin A. E. (1984) Manganiferous orthopyroxene and olivine in the Allende meteorite. *Am. Mineral.* **69**, 880–888.

Schindelin J., Rueden C. T., Hiner M. C. and Eliceiri K. W. (2015) The ImageJ ecosystem: an open platform for biomedical image analysis. *Mol. Reprod. Dev.* **82**, 518–529.

Sears D. W. G., Benoit P. H. and Jie L. (1993) Two chondrule groups each with distinctive rims in Murchison recognized by cathodoluminescence. *Meteoritics* **28**, 669–675.

Singerling S. A. (2018) Primary and altered iron sulfides in CM and CR carbonaceous chondrites: insights into nebular and parent body processes. Ph.D. Dissertation, University of New Mexico.

Stephan T., Trappitsch R., Davis A. M., Pellin M. J., Rost D., Savina M. R., Yokochi R. and Liu N. (2016) CHILI − the Chicago Instrument for Laser Ionization − a new tool for isotope measurements in cosmochemistry. *Int. J. Mass Spectrom.* **407**, 1–15.

Sugaki A. and Shima H. (1965) Synthetic sulfide minerals (III). In *Memoirs of the Faculty of Engineering, Yamaguchi University* pp. 109–118.

Sugiura N., Petaev M. I., Kimura M., Miyazaki A. and Hiyagon H. (2009) Nebular history of amoeboid olivine aggregates. *Meteorit. Planet. Sci.* **44**, 559–572.

Takayama A. and Tomeoka K. (2012) Fine-grained rims surrounding chondrules in the Tagish Lake carbonaceous chondrite: verification of their formation through parent-body processes. *Geochim. Cosmochim. Acta* **98**, 1–18.

Tomeoka K. and Tanimura I. (2000) Phyllosilicate-rich chondrule rims in the vigarano CV3 chondrite: evidence for parent-body processes. *Geochim. Cosmochim. Acta* **64**, 1971–1988.

Trappitsch R., Stephan T., Savina M. R., Davis A. M., Pellin M. J., Rost D., Gyngard F., Gallino R., Bisterzo S., Cristallo S. and Dauphas N. (2018) Simultaneous iron and nickel isotopic analyses of presolar silicon carbide grains. *Geochim. Cosmochim. Acta* **221**, 87–108.

Trigo-Rodriguez J. M., Rubin A. E. and Wasson J. T. (2006) Non-nebular origin of dark mantles around chondrules and inclusions in CM chondrites. *Geochim. Cosmochim. Acta* **70**, 1271–1290.

Tsuchiyama A. (1998) Condensation experiments using a forsterite evaporation source in H2 at low pressures. *Mineral. J.* **20**, 59–80.

Vacher L. G., Marrocchi Y., Verdier-Paoletti M. J., Villeneuve J. and Gounelle M. (2016) Inward radial mixing of interstellar water ices in the solar protplanetary disk. *Astrophys. J. Lett.* **827**, L1 (6 pp).

Vacher L. G., Marrocchi Y., Verdier-Paoletti M. J., Villeneuve J. and Gounelle M. (2017) Erratum: "Inward radial mixing of interstellar water ices in the solar protoplanetary disk" (2016, ApJL, 827, L1). *Astrophys. J. Lett.* **836**, L16.

Vacher L. G., Truche L., Faure F., Tissandier L., Mosser-Ruck R. and Marrocchi Y. (2019) Deciphering the conditions of tochilinite and cronstedtite formation in CM chondrites from low temperature hydrothermal experiments. *Meteorit. Planet. Sci.* **54**, 1870–1889.

Verdier-Paoletti M. J., Nittler L. R. and Wang J. (2019) First detection of presolar grains in Paris, the most preserved CM chondrite. *Lunar Planet. Sci.* **50**, #2948.

Vollmer C., Pelka M., Leitner J. and Janssen A. (2020) Amorphous silicates as a record of solar nebular and parent body processes—A transmission electron microscope study of fine-grained rims and matrix in three Antarctic CR chondrites. *Meteorit. Planet. Sci.* **55**, 1491–1508.

Weisberg M. K., Connolly Jr H. C. and Ebel D. S. (2004) Petrology and origin of amoeboid olivine aggregates in CR chondrites. *Meteorit. Planet. Sci.* **39**, 1741–1753.

Westphal A. J., Stroud R. M., Bechtel H. A., Brenker F. E., Butterworth A. L., Flynn G. J., Frank D. R., Gainsforth Z., Hillier J. K., Postberg F., Simionovici A. S., Sterken V. J., Nittler L. R., Allen C., Anderson D., Ansari A., Bajt S., Bastien R. K., Bassim N., Bridges J., Brownlee D. E., Burchell M., Burghammer M., Changela H., Cloetens P., Davis A. M., Doll R., Floss C., Grün E., Heck P. R., Hoppe P., Hudson B., Huth J., Kearsley A., King A. J., Lai B., Leitner J., Lemelle L., Leonard A., Leroux H., Lettieri R., Marchant W., Ogliore R., Ong W. J., Price M. C., Sandford S. A., Tresseras J.-A. S., Schmitz S., Schoonjans T., Schreiber K., Silversmit G., Solé V. A., Srama R., Stadermann F., Stephan T., Stodolna J., Sutton S., Trieloff M., Tsou P., Tyliszczak T., Vekemans B., Vincze L., Korff J. V., Wordsworth N., Zevin D., Zolensky M. E. and Dusters 30714 Stardust@home

(2014) Evidence for interstellar origin of seven dust particles collected by the Stardust spacecraft. *Science* **345**, 786–791.

Yund R. A. and Hall H. T. (1969) Hexagonal and monoclinic pyrrhotites. *Econ. Geol.* **64**, 420–423.

Zanetta P.-M., Leroux H., Le Guillou C., Zanda B. and Hewins R. H. (2021) Nebular thermal processing of accretionary fine-grained rims in the Paris CM chondrite. *Geochim. Cosmochim. Acta* **295**, 135–154.

Zhao X., Floss C., Lin Y. and Bose M. (2013) Stardust investigation into the CR chondrite Grove Mountain 021710. *Astrophys. J.* **769**, 49.

Zhukovska S., Gail H.-P. and Trieloff M. (2008) Evolution of interstellar dust and stardust in the solar neighbourhood. *Astron. Astrophys.* **479**, 453–480.

Zinner E. (2014) Presolar grains. In *Meteorites and Cosmochemical Processes* (Ed. A. M. Davis), Vol. 1 *Treatise on Geochemistry, 2nd Ed.* (Exec. Eds. H. D. Holland and K. K. Turekian), Elsevier, Oxford, pp. 181–213.

Zolensky M. E., Nakamura K., Gounelle M., Mikouchi T., Kasama T., Tachikawa O. and Tonui E. (2002) Mineralogy of Tagish Lake: an ungrouped type 2 carbonaceous chondrite. *Meteorit. Planet. Sci.* **37**, 737–761.

Zolensky M. E. and Thomas K. L. (1995) Iron and iron-nickel sulfides in chondritic interplanetary dust particles. *Geochim. Cosmochim. Acta* **59**, 4707–4712.

Zolensky M. E., Zega T. J., Yano H., Wirick S., Westphal A. J., Weisberg M. K., Weber I., Warren J. L., Velbel M. A., Tsuchiyama A., Tsou P., Toppani A., Tomioka N., Tomeoka K., Teslich N., Taheri M., Susini J., Stroud R., Stephan T., Stadermann F. J., Snead C. J., Simon S. B., Simionovici A., See T. H., Robert F., Rietmeijer F. J. M., Rao W., Perronnet M. C., Papanastassiou D. A., Okudaira K., Ohsumi K., Ohnishi I., Nakamura-Messenger K., Nakamura T., Mostefaoui S., Mikouchi T., Meibom A., Matrajt G., Marcus M. A., Leroux H., Lemelle L., Le L., Lanzirotti A., Langenhorst F., Krot A. N., Keller L. P., Kearsley A. T., Joswiak D., Jacob D., Ishii H., Harvey R., Hagiya K., Grossman L., Grossman J. N., Graham G. A., Gounelle M., Gillet P., Genge M. J., Flynn G., Ferroir T., Fallon S., Ebel D. S., Dai Z. R., Cordier P., Clark B., Chi M., Butterworth A. L., Brownlee D. E., Bridges J. C., Brennan S., Brearley A., Bradley J. P., Bleuet P., Bland P. A. and Bastien R. (2006) Mineralogy and petrology of comet 81P/Wild 2 nucleus samples. *Science* **314**, 1735–1739.